



Universiteit
Leiden
The Netherlands

A search for transient reductions in the inflaton speed of sound in cosmological data, and other topics

Torrado Cacho, J.

Citation

Torrado Cacho, J. (2015, March 31). *A search for transient reductions in the inflaton speed of sound in cosmological data, and other topics*. *Casimir PhD Series*. Retrieved from <https://hdl.handle.net/1887/32593>

Version: Not Applicable (or Unknown)

License: [Licence agreement concerning inclusion of doctoral thesis in the Institutional Repository of the University of Leiden](#)

Downloaded from: <https://hdl.handle.net/1887/32593>

Note: To cite this publication please use the final published version (if applicable).

Cover Page



Universiteit Leiden



The handle <http://hdl.handle.net/1887/32593> holds various files of this Leiden University dissertation

Author: Torrado Cacho, Jesús

Title: A search for transient reductions in the speed of sound of the inflaton in cosmological data, and other topics

Issue Date: 2015-03-31

A search for transient reductions
in the speed of sound of the inflaton
in cosmological data, and other topics

Proefschrift

ter verkrijging van
de graad van Doctor aan de Universiteit Leiden,
op gezag van Rector Magnificus prof. mr. C.J.J.M. Stolker,
volgens besluit van het College voor Promoties
te verdedigen op dinsdag 31 maart 2015
klokke 13.45 uur

door

Jesús Torrado Cacho

geboren te Badajoz (Spanje)
in 1984

Promotiecommissie:

Promotor: Prof. dr. Ana Achúcarro

Overige leden: Dr. J. Lesgourges (CERN, Genève, Zwitserland)
Dr. E.I. Zavala (Swansea University, Swansea, VK)
Dr. E. Pajer (ITF Utrecht)
Prof. dr. E.R. Eliel
Prof. dr. K.E. Schalm
Dr. W. Valkenburg

Casimir PhD series Delft-Leiden 2015-4

ISBN 978-90-8593-212-3

An electronic version of this thesis can be found at <https://openaccess.leidenuniv.nl>

Part of this research is supported by the Graduate School “Particle Physics at the Energy Frontier of New Phenomena”, which is funded by the German Research Foundation (DFG).

The cover shows a triangular section of Planck’s 2013 CMB sky (★), reflected several times along its sides to form a 2-dimensional orbifold with the symmetry of a hexagonal lattice, gathering both of the topics of this thesis (but bearing no physical meaning).

The font used on the cover is Fjalla, Copyright 2011 by Sorkin Type Co, under SIL Open Font license v1.1.

(★) Copyright: ESA and the Planck Collaboration. Reproduced here for educational purposes. No endorsement from ESA is implied.

*To my parents, thanks to whom I am not just a physicist,
but a person in all its dimensions.*

*And to Berenice, who walked along the valley with me –
without your support this thesis would have never been possible.*

Contents

Foreword	7
I Constraints on cosmic inflation with transient reductions in the speed of sound of the inflaton	11
1 Introduction	13
1.1 Background Cosmology – Large scale geometry of the universe . . .	13
1.2 The <i>horizon problem</i> and the need for inflation	18
1.3 Primordial perturbations	24
1.4 The Cosmic Microwave Background	33
1.5 Constraining inflation with the CMB – parameter extraction . . .	39
Bibliography	52
2 Localized correlated features in the CMB power spectrum and primordial bispectrum from a transient reduction in the speed of sound	57
2.1 Introduction	58
2.2 Our test case – A gaussian in e -folds	60
2.3 Methodology of the search	62
2.4 Summary and analysis of the results	64
2.5 Comparison with the search for features in Planck’s bispectrum . .	73
2.6 Conclusions and discussion	75
Bibliography	77
3 Adding Large Scale Structure data into the search	85
3.1 Introduction	86
3.2 Review of the model	87
3.3 Methodology and data sets	87
3.4 Results and discussion	90
3.5 Conclusions and outlook	93
Bibliography	95

4	Peer-reviewed and published cosmological code	99
4.1	Introduction	99
4.2	Arbitrary Primordial Power Spectrum for CLASS	100
4.3	Interfacing of MULTINEST into MONTE PYTHON	101
	Bibliography	106
II	Geometry of Heterotic Orbifolds	107
5	Classification of symmetric toroidal orbifolds	109
5.1	Introduction	110
5.2	Construction of toroidal orbifolds	111
5.3	Equivalences of space groups	114
5.4	Classification of space groups	121
5.5	Results: classification of toroidal orbifolds	122
5.6	Summary and discussion	128
5.A	Details on lattices	130
5.B	Two-dimensional orbifolds	137
	Bibliography	141
	Summary	147
	Samenvatting	151
	List of publications	156
	Curriculum vitæ	159
	Acknowledgements	161

Foreword

This thesis consists of two different parts, separating research projects carried out in two different groups.

In the first and longest part of this thesis, we attempt to fit the signal for a reduction in the speed of sound of the inflaton. In chapter 1, we shortly introduce the topics discussed in this thesis, namely Λ CDM cosmology, transient reduction in the speed of sound during inflation, and Bayesian statistical inference. Afterwards, we attempt to fit a particular hypothesis for the speed of sound reduction using Cosmic Microwave Background data (chapter 2) and later adding Large Scale Structure data to the search (chapter 3). Finally, in chapter 4 we present two pieces of code that were elaborated for the research in this thesis, and later released to the community.

In the second part, consisting solely of chapter 5, we present a classification of all possible 6-dimensional symmetric toroidal orbifolds over which Heterotic String Theory leads to a supersymmetric model. To do that, we made use of standard crystallographic tools.

Abbreviations

CMB Cosmic Microwave Background radiation

(C)DM (Cold) Dark Matter

Λ CDM Dark Energy, Cold Dark Matter cosmological model

EFT Effective Field Theory

FLRW Friedmann-Lemaître-Robertson-Walker, either meaning simply the so-called metric, or the full homogeneous and isotropic cosmology

GR General Relativity

GSR Generalised Slow-Roll

GUT Grand Unification Theory

LSS Large Scale Structure

MCMC Markov chain Monte Carlo

pdf Probability Density Function (often in low caps)

QFT Quantum Field Theory

SRFT Slow-Roll Fourier Transform

SUSY Super-symmetry

WMAP(#) The Wilkinson Microwave Anisotropy Probe; a number # after it refers to the data release corresponding to the #-th year of the survey.

WP WMAP low- ℓ polarisation likelihood.



Part I

Constraints on cosmic inflation with transient reductions in the speed of sound of the inflaton

Chapter 1

Introduction

In this chapter, we review how to characterise inflation through cosmological observations. After a brief description of FLRW cosmology, we describe slow-roll inflation and the effect of possible transient reductions in the speed of sound of the inflaton. Later we describe the Cosmic Microwave Background and how it can be used to constrain features in the inflationary potential. Finally, we review the statistical tools commonly used to achieve the characterisation of inflation through general cosmological data sets.

For the sake of brevity, most of the detailed calculations are not shown. Everywhere in this thesis, we use natural units, $c = \hbar = 1$, but keep the Newton's gravitational constant (and thus Planck mass) explicit .

1.1 Background Cosmology – Large scale geometry of the universe

1.1.1 Description and evolution of homogeneous cosmologies

We observe the CMB radiation and the LSS to be on large scales mostly isotropic. Isotropy from here, combined with the Copernican principle – *our place in the Universe is not special* – implies homogeneity of the space.

In this thesis we will always assume the space-time to be described on cosmological scales as a perfect fluid, determined by only two quantities, its density ρ and pressure p , which is by definition homogeneous, isotropic, having no viscosity, shear tension or energy conduction – it can just uniformly compress or expand.

To describe this system in the context of General Relativity, one normally chooses a *comoving frame* in which the 3-surfaces of homogeneity are synchronous and the same 3-d coordinates are assigned to the same particle of the fluid at all times. In this frame, the metric describing the very large scales reads (we take

$c = 1$)

$$ds^2 = g_{\mu\nu} dx^\mu dx^\nu := -dt^2 + a^2(t) dl^2, \quad (1.1)$$

where $a(t)$ is a *scale factor* and dl^2 is the metric of the 3-space:

$$dl^2 := d\chi^2 + \Sigma^2(\chi) (d\theta^2 + \sin^2\theta d\phi^2), \quad \Sigma(\chi) = \begin{cases} \sinh \chi & \text{if } \kappa = -1 \\ \chi & \text{if } \kappa = 0 \\ \sin \chi & \text{if } \kappa = +1 \end{cases}, \quad (1.2)$$

where κ is a parameter defining the 3-curvature, proportional to the Ricci scalar of the 3-space.

We often define the *conformal time*, τ , by factoring out the scale factor:

$$ds^2 = a^2(\tau) (-d\tau^2 + dl^2), \quad d\tau = \frac{dt}{a}. \quad (1.3)$$

On the other side of the Einstein equation, the *matter* side, we have the stress-energy tensor of a perfect fluid in comoving coordinates, which is simply

$$T_{\mu\nu} = \text{diag}(\rho, p, p, p). \quad (1.4)$$

Finally, from the Einstein equation and the continuity equation $\nabla_\alpha T^{\alpha\mu} = 0$ we derive the commonly used pair of Friedmann equations

$$3H^2 + 3\frac{\kappa}{a^2} - \Lambda = 8\pi G \rho, \quad (1.5a)$$

$$\dot{\rho} + 3H(\rho + p) = 0, \quad (1.5b)$$

where we have introduced the Hubble parameter, $H := d/dt \log a = \dot{a}/a$, and where Λ is the Einstein's Cosmological constant, and G is Newton's gravitational constant.

The perfect fluid that fills the Universe has, from the very-large-scale gravitational point of view, two different components: matter (M), and radiation (R), with equations of state

$$p = \omega\rho \quad \text{with} \quad \omega = \begin{cases} \frac{1}{3} & \text{Radiation} \\ 0 & \text{Matter} \\ -1 & \text{Dark Energy} \end{cases}. \quad (1.6)$$

Note that we have included another component: Dark Energy, which is the effect of the cosmological constant (Λ) in the dynamics of the Universe when treated as a fluid, i.e. when taken to the RHS in eq. (1.5a); we can define $\rho_\Lambda := \Lambda/8\pi G$, and, since ρ_Λ is constant, the continuity equation imposes $\omega_\Lambda = -1$. From the continuity equation we can derive the evolution of the density of each species i with $a(t)$:

$$\rho_i = \rho_{i,0} \left(\frac{a}{a_0} \right)^{-3(1+\omega_i)}, \quad (1.7)$$

where the sub-index 0 refers to the values in a particular instant, usually *today*.

The solution for a flat FLRW Universe dominated by a fluid satisfying the *strong energy condition* $\omega > -1/3$ (i.e. matter or radiation) is

$$a(t) = a_0 t^{\frac{2}{3(1+\omega)}} . \quad (1.8)$$

For Dark Energy, with equation of state given by $\omega = -1$,

$$a(t) = a_0 e^{Ht} . \quad (1.9)$$

It is useful to derive an equation for the acceleration of the scale factor a by differentiating w.r.t. time eq. (1.5a) and inserting (1.5b):¹

$$\frac{\ddot{a}}{a} = -\frac{4\pi G}{3}(1 + 3\omega)\rho . \quad (1.10)$$

This equation makes clear that the expansion of the Universe accelerates when it is dominated by species with $\omega_i < -1/3$, i.e. it decelerates whenever Matter or Radiation dominate, and accelerates whenever Dark Energy dominates. The order in which the different species dominate the expansion can be guessed from eq. (1.7): radiation energy density decays the fastest with time, so at some point matter takes over; finally, since the energy density of Dark Energy is constant, it becomes eventually the dominating species. Therefore, unless something happens which is extraneous to the model as defined so far, the dynamics are dominated in order by

Radiation \rightarrow Matter \rightarrow Dark Energy .

According to the Supernovæ data [35, 34], the Universe reached a Dark-Energy-dominated stage at $t \simeq 9.8$ Gyr, approximately 4 Gyr ago.

Data coming from different surveys, including CMB, Gravitational Lensing and type Ia Supernovæ redshifts, point clearly towards a very close to flat Universe, $\kappa/(aH)^2 \simeq 0$, populated today by an insignificant amount of radiation, a significant amount matter and an even more significant proportion of Dark Energy [36]. This, together with Standard Model particle physics, is the model of the Universe we will assume for now.

1.1.2 Causal structure of the Universe – Horizons and Hubble radius

Let us now talk about the *causal structure* of the universe: which events could ever be influenced by which other events. We define the (*comoving*) *particle horizon* of an observer at a time t as the sphere enclosing all points of the fluid that have

¹Notice that this equation can also be obtained from the spatial component of the Einstein equation.

ever been in causal contact with the observer, i.e. from which a photon emitted at any time may have ever reached the observer. Unsurprisingly, its radius is equal to the (conformal) length that a photon has been able to travel since the origin of the Universe $t = \delta t$ (we admit that the FLRW is not valid from the very beginning of the Universe $t = 0$, if it exists):

$$r_p(t) := \int_{\delta t}^t \frac{d\tilde{t}}{a(\tilde{t})}. \quad (1.11)$$

If this integral is finite, there exists a particle horizon, meaning that there is a distance such that two points which are separated by more than it, have never been in causal contact by the time t . In a FLRW Universe dominated by radiation, as ours is initially, eq. (1.8) tells us that the integral converges and is dominated by its upper limit. A divergence in the integral (1.11) implies that every pair of points in the fluid have already been in causal contact with each other by the time t . It is obvious that the particle horizon can only grow with time: if a point in the fluid was ever in the horizon, it will always be.

The equivalent concept towards the future is the (*comoving*) *event horizon* of an observer at a time t : it is the sphere enclosing all points of the fluid at a time t that will *ever* be in causal contact with us before the end of the Universe t_{end} :

$$r_e(t) := \int_t^{t_{\text{end}}} \frac{d\tilde{t}}{a(\tilde{t})}. \quad (1.12)$$

Again, this integral may diverge, meaning that we will be able to observe any point of the Universe if we are patient enough. This is the case of a decelerating Universe without a final singularity. In the opposite case of a converging integral, e.g. for an ever-faster expanding Universe, as time goes by more and more distant objects whose light ever reached us will never again be observable.

Let us now define the *recessional velocity* v_{rec} and the *radial peculiar velocity* v_{pec} of a galaxy in a point χ of the fluid. The total velocity of an object today is equal to the derivative of its physical distance $d = a\chi$ with respect to time

$$v_{\text{total}} = \underbrace{\dot{a}\chi}_{v_{\text{rec}}} + \underbrace{a\dot{\chi}}_{v_{\text{pec}}}. \quad (1.13)$$

With this definition, a point of the fluid has only recessional velocity, and photons have, on top of a recessional velocity, a peculiar velocity of $v_{\text{pec}} = c \equiv 1$. Neither the total or the recessional velocity are properly defined 4-speeds, as the peculiar velocity is (notice how the velocities addition rule of Relativity is not applied here, as it would be for local 4-speeds). Notice how this definition implies the Hubble law automatically:

$$v_{\text{rec}} = \frac{\dot{a}}{a} a\chi = Hd. \quad (1.14)$$

We define the *comoving Hubble radius* r_{H} as the comoving distance to the points of the fluid that recede from us at the speed of light, $v_{\text{rec}} = c \equiv 1$:

$$r_{\text{H}}(t) = \frac{1}{aH}, \quad (1.15)$$

and the *comoving Hubble sphere* as the surface containing all such points. Recessional velocities higher than the speed of light are possible (see e.g. [15]). Photons emitted towards us from a superluminally receding galaxy actually recede from us, while at the same time any photon overtakes any observer at the speed of light, thus making no conflict with GR. The Hubble radius is *always* contained between the particle and event horizons.

Since photons emitted from outside the Hubble sphere recede from us, one would be tempted to think that the *Hubble radius* is the true event horizon: galaxies outside it (*super-Hubble*), will never be observable. That is definitely not true (see e.g. [16]): the size of the comoving Hubble sphere changes with time, growing in decelerated Universes and shrinking in accelerated ones. A growing Hubble sphere may overtake the receding photons emitted from a super-Hubble galaxy, thus making it observable (see fig. 1.1). Notice that the *physical* Hubble radius $ar_{\text{H}} = H^{-1}$ grows for Universes dominated by physical fluids, $\omega > 1/3$, and stays constant for Dark Energy dominated Universes, $\omega = -1$.

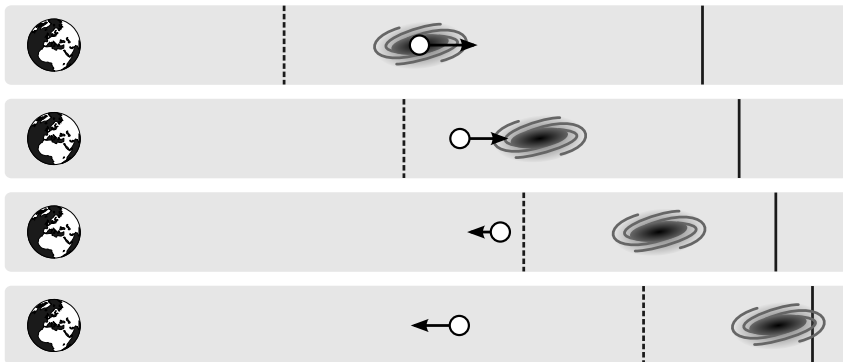


Figure 1.1: Sequence of the path of a photon (white spot) emitted by a super-Hubble galaxy in a decelerating Universe: the super-Hubble galaxy becomes observable when the initially receding photon is overtaken by the expanding Hubble sphere (dotted line). This only happens when the galaxy is sub-event-horizon (continuous line) at the instant of emission. The arrow represents the total velocity of the photon, as in eq. (1.13). The plot's x direction represents physical distances.

1.2 The *horizon problem* and the need for inflation

1.2.1 The *horizon problem*

The CMB radiation was emitted when the radiation temperature of the Universe was such that the electrons would fall into the nuclei to form atoms, leaving the photons free to travel through the Universe. We call this moment, which has a short but different-from-zero duration, *recombination*. The CMB is astonishingly uniform, reproducing very precisely a black body spectrum with a temperature $T_{\text{CMB}} = 2.725 \text{ K}$. On top of it, once known foreground effects have been accounted for, one finds inhomogeneities of order $10^{-5} T_{\text{CMB}}$, which are quite correlated on all scales accessible to the current experiments.

Now let us do a small calculation: under the assumptions stated in section 1.1, using eq. (1.11), we can calculate the size of the particle horizon at *recombination* t_{rec} , the moment when the CMB radiation was emitted; then, we can calculate the angle that separates today in the sky two points that were never in causal contact – it turns out to be $\simeq 2^\circ$. This has a very simple consequence: points separated in the sky by bigger angles should show fluctuations of their CMB temperature of order $1 \cdot T_{\text{CMB}}$, and those fluctuations should be uncorrelated, i.e. the CMB temperature spectrum should be 0 for $\ell \lesssim 90$ (we discuss the definition of the CMB power spectrum later in section 1.4).

As we just stated, this is certainly not what happens. Either our calculation of the particle horizon at recombination is wrong (i.e. the evolution of $a(t)$ from $t = 0$ to t_{rec} is not as we think it is), or the initial conditions of the Universe were *really* special.

1.2.2 The *flatness conundrum*

Let us recover the curvature in the Friedmann equation (1.5a) (and include the cosmological constant in the density term) and rewrite it as

$$1 - \underbrace{\frac{8\pi G}{3H^2} \rho}_{\Omega} = -\frac{\kappa}{(aH)^2}. \quad (1.16)$$

Notice how the newly defined, positive quantity Ω controls the curvature of the model:

$$\begin{cases} \Omega < 1 & \text{if } \kappa = -1 \\ \Omega = 1 & \text{if } \kappa = 0 \\ \Omega > 1 & \text{if } \kappa = +1 \end{cases}. \quad (1.17)$$

Let us now show that the value for a flat Universe, $\Omega = 1$, is unstable. For that, let us calculate its derivative w.r.t. a :

$$\frac{d}{da} (1 - \Omega) = \frac{1 + 3\omega}{a} \Omega (1 - \Omega). \quad (1.18)$$

Notice the sign of the derivative:

$$\text{sign} \left(\frac{d}{da} (1 - \Omega) \right) = \text{sign} (1 + 3\omega) \text{sign} (1 - \Omega) . \quad (1.19)$$

For matter and radiation ($\omega = 0, 1/3$) the value of $(1 - \Omega)$ goes away from 0 as a grows, curving the Universe more and more; instead, for a fluid with negative pressure $\omega < -1/3$, the Universe tends towards flatness.

Today [36], our bound for the curvature is $|1 - \Omega_0| \simeq 0.05$. Knowing (see sec. 1.1) that the Universe spent most of its history dominated by matter and radiation, we can extrapolate this value towards the early stages of the Universe, e.g. at the epoch corresponding to energy scales of order 10^{16} GeV, where we find $|1 - \Omega| \simeq 10^{-55}$, many orders of magnitude smaller. Thus, the Universe should have started its history at stunningly low values of the curvature. This apparent *fine-tuning* of the initial conditions could use a physical explanation.

1.2.3 Digression – Problems and conundrums

We just acknowledged two observations which are surprising when put into the context of the cosmological model as we have established it so far. Are those surprises *physical problems*, i.e. do they *need* to be addressed in order for the theory to be correct or to be complete? In order to answer those questions, let us consider the issue in a more abstract way.

Let's first divide the predictions that models make into two types: deterministic and probabilistic. In turn, probabilistic predictions may come in the form of a well-defined probability distribution function (pdf), or as a lack of predictivity for a certain parameter or outcome, in which case only the main features of a *prior* pdf are known (e.g. equal probability for unpreferred values).

One deterministic prediction would be e.g. how much will a spring elongate when pulled with a certain amount of force. One probabilistic prediction is e.g. the life of a radioactive nucleus, whose decay is a random process. When a deterministic prediction is contradicted by a properly done experiment where observational errors have been accounted for, we have a *physical problem* at hand: our model for the phenomenon is apparently not correct, and we must explain the new observation by modifying it.

When testing a probabilistic prediction the situation is more complicated, since it depends on the amount of samples of the distribution that we have got or may be able to get soon: without enough samples, we cannot characterise the distribution with enough certainty. Regarding sample collection, we distinguish two different situations²

²A word of caution: the ability to gather samples changes with time: we have continuously achieved previously unimaginable measurements. Thus, questions that were previously philosophical, or simply non-existing, turn suddenly into physical ones. This is often associated with *paradigm shifts* [28].

- a) We have collected, or will be able to collect soon, enough samples to test the features of a pdf. In this case, if there is a contradiction with the pdf predicted by the model, or if the model does not predict a particular pdf, we do have a *physical problem*: we have in the first case to modify our model, and in the second one we should extend it to include the new information.
- b) We have neither collected, nor will be able to collect soon, enough samples to be able to tell anything about the pdf with minimum reliability. In this case, the model, despite predicting a certain pdf, cannot be tested against the data. Then, no contradiction between the model and the data can be claimed, even if the data looks surprising, a situation which we often call *fine-tuning*. There is no *physical problem* at hand, but a philosophical one; in the context of physics, we can call this situations *conundrums*.

In conclusion, in order to call an apparently surprising result a *physical problem*, we need to be able to assess whether there is actually a contradiction between the prediction and the observation. If we cannot properly perform such assessment, we should call them something else, e.g. *conundrums*, since we cannot resolve the situation using scientific methods. Answering conundrums is satisfactory from the point of view of Physics, and can be argued to be part of the scientific endeavour; but those answers cannot be falsified, so the quest is only worthy when they are addressed by simple principles that at the same time solve real physical problems. Solutions to conundrums are the *icing on the cake*, and sometimes good indications of where our model may be extended, but they may also be *red herrings* that distract us from looking at the real physical problems.

Now back to our apparent problems

Horizon problem *The size of the particle horizon at recombination implies that points in the sky separated by more than 2° should have big temperature variations (of order the background temperature T_{CMB}), which should be uncorrelated.* The prediction is probabilistic – it is not impossible that there are no such variations, just unlikely – and the pdf is not completely characterised, but its central value, T_{CMB} , is well determined. In this case, we do have a big number of samples – every pair of regions in the sky separated by $> 2^\circ$, the size of those regions being determined by the resolution of the experiment. They provide a statistically very significant contradiction of the predicted result: the variations on these scales are very small and strongly correlated – here is a *physical problem*: our model is incomplete.

Flatness conundrum *In a Universe dominated most of its history by matter and radiation, as ours has been, the curvature grows with time, so finding a very flat Universe today is quite unexpected, since it would imply an incredibly low amount of curvature in the past.* Here, we have a deterministic prediction: given a value of the curvature in the past, we would know the current one. But we do not know the value in the past, only in the present

day, so we are concerned by a different, probabilistic prediction: if we assume that all values of the curvature were equally likely in the past (or at least approximately so), we expect to find very high curvatures today, flat Universes being highly unlikely. There is only one possible sample here, which is the observable Universe. The fact that our Universe is very improbable may not be appealing, but with only one sample at hand we may as well just have been lucky. There is no physical problem here, but an interesting *conundrum*. We may state that solving this conundrum is possible by modifying the model to increase the probability of a flat Universe today.

Any solution to the horizon problem (which also predicts the correct spectrum for the anisotropies) is equally good, unless further evidence against it is found. But those solutions that in addition address the flatness conundrum without introducing new assumptions deserve special attention.

1.2.4 Inflation as a possible solution

Let us see how both the horizon problem and the flatness conundrum can be addressed by assuming that the Universe during his very early moments underwent a stage of accelerated expansion [1], or *Inflation*.

Consider the horizon problem. Given a long enough period of accelerated expansion, it is intuitively immediate that every point in the Universe is causally connected to every other one, since the points that appear to be today very far away must have been very close in the past. To quantify this, let us solve the particle horizon, eq. (1.11), for a flat Universe dominated by a particular fluid, indicated by i , with equation of state parametrised by ω_i :

$$r_p = \frac{C}{\frac{1}{2}(1 + 3\omega_i)} a^{\frac{1}{2}(1+3\omega_i)} \Big|_{a_{\text{ini}}}^{a_{\text{rec}}}, \quad (1.20)$$

where C is a positive constant, irrelevant here, and a_{ini} and a_{rec} are respectively the scale factor at the beginning of the Universe and at recombination. As eq. (1.10) proves, for fluids with negative pressure such that $\rho + 3p < 0$, or equation of state $\omega_i < -1/3$, the expansion of the Universe is accelerated. In the particle horizon, those values of ω_i make the exponent of the a negative, turning the lower bound into the biggest contribution: for values of the initial scale factor close to zero, the size of the comoving particle horizon tends towards infinity. Our initial intuition gets thus confirmed: an initial phase of accelerated inflation can solve the horizon problem.

Since in our model the Universe starts dominated by radiation, in order to get this phase of accelerated inflation we need to assume that the Universe was initially dominated by a different fluid that later decayed into the Standard Model species that constitute the Universe today, at energies such that they behave as radiation. As we argued, this candidate must behave as a fluid with negative

pressure, $\rho + 3p < 0$ ($\omega < -1/3$). We look for a substance with that feature, the simplest one being a scalar field in a *slow-roll* regime, as we will describe.

Let us assume that at very early times the Universe's dynamics is dominated by a single, homogeneous scalar field $\phi(t, \mathbf{x}) = \phi(t)$, which we will call *inflaton*, that is minimally coupled to gravity, with an action

$$S = \int d^4x \sqrt{-g} \left[\frac{M_{\text{Pl}}^2}{2} R - \frac{1}{2} g^{\mu\nu} \partial_\mu \phi \partial_\nu \phi - V(\phi) \right], \quad (1.21)$$

where $M_{\text{Pl}} = \sqrt{\frac{\hbar c}{8\pi G}}$ is the Planck mass, R is the 4-dimensional Ricci scalar and $V(\phi)$ is a potential which is so far arbitrary. Using the Klein-Gordon equation for the scalar field, and the Friedmann equations for its stress-energy tensor, we arrive at the relations (of which only two are independent)

$$\ddot{\phi} + 3H\dot{\phi} = -\frac{dV}{d\phi}, \quad H^2 = \frac{1}{3M_{\text{Pl}}^2} \left(\frac{1}{2} \dot{\phi}^2 + V \right), \quad \dot{H} = \frac{1}{M_{\text{Pl}}^2} \left(-\frac{1}{2} \dot{\phi}^2 \right). \quad (1.22)$$

From this point onwards, for the sake of simplicity, we take $M_{\text{Pl}} = 1$. Notice how H^2 is proportional to the sum of the kinetic ($K \sim 1/2 \dot{\phi}^2$) and the potential energies of the scalar field, and how $-\dot{H}$ equals the kinetic energy. Calculating the stress-energy tensor from the action above, and comparing with that of a perfect fluid, eq. (1.4), we find the density and pressure of the scalar field:

$$\rho_\phi = \frac{1}{2} \dot{\phi}^2 + V, \quad p_\phi = \frac{1}{2} \dot{\phi}^2 - V. \quad (1.23)$$

Now consider the limit $K \ll V$. In that limit, we immediately get accelerated expansion: $\rho + 3p < 0$, in particular with an equation of state for the scalar field $\omega_\phi \simeq -1$. From the third equation in (1.22), we get an almost constant Hubble parameter, which implies that the scale factor behaves as

$$a \propto e^{Ht}, \quad H \simeq \text{const}. \quad (1.24)$$

This allows us to define a useful new time scale, e -folds N , as $dN = Hdt$: during one e -fold, the scale factor a grows by a factor of e .

One can now quantify how long Inflation must last in order to solve the horizon problem, i.e. to get all the scales in the CMB sky into the particle horizon. This turns out to be 50 – 60 e -folds. With respect to the flatness conundrum, we can see from eqs. (1.18) and (1.19) that flatness becomes an attractor for $\rho + 3p < 0$, so a flat Universe becomes more likely regardless of the original curvature before Inflation. Notice how, unlike the horizon *problem*, the flatness *conundrum* has no quantitative solution; but it is remarkable that it is addressed by the same solution as the horizon problem, which speaks in favour of accelerated expansion against other possible solutions that do not make the Universe flatten with time.

Let us now talk some more about the physical meaning of this framework of Inflation, and incidentally also about its *duration*. Inflation would last as long as the approximation $K \ll V$ holds. That condition describes the dynamics of a field which is *slowly rolling* down a potential. This means that in the first equation in (1.22) the acceleration is very small, and the evolution of the field is dominated by the other terms: the friction term $3H\dot{\phi}$ and the slope of the potential $dV/d\phi$. In fig. 1.2 we display two possible realisations of a slow-roll potential. We call this whole setting *single-field, slow-roll Inflation*. A slow-roll setting can also be realised in an effectively-single-field theory resulting from integrating out the heavy degrees of freedom (though multiple-field scenarios in which more than one field is light are also possible).

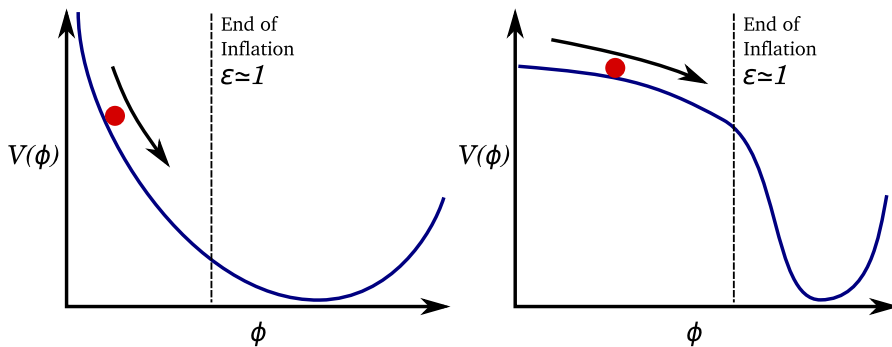


Figure 1.2: Depiction of two simple slow-roll potentials. In the left, the high slope of the potential $dV/d\phi$ gets compensated by an equally large value of the friction term $3H\dot{\phi}$. In the right, both the slope and the friction are smaller. In both cases, inflation ends whenever one term becomes much bigger than the other, creating a large acceleration.

In order to quantify the slow-roll condition $K \ll V$, we define the positive quantity ϵ , called *first slow-roll parameter*:

$$\epsilon := -\frac{\dot{H}}{H^2} = -\frac{d \log H}{dN} = \frac{1}{3} \frac{K}{K+V} < 1. \quad (1.25)$$

Its being smaller than 1 guarantees that $\ddot{a} > 0$, hence the Universe's expansion is accelerated. In order for Inflation to last enough time we must also guarantee that the slow-roll condition is satisfied for long enough, i.e. ϵ does not grow too fast, which is given by the *second slow-roll parameter*:

$$|\eta| := \left| \frac{\dot{\epsilon}}{H\epsilon} \right| = \left| \frac{d \log \epsilon}{dN} \right| < 1. \quad (1.26)$$

We could keep adding higher derivative terms to the description, but this is enough to describe the current data with sufficient precision.

1.3 Primordial perturbations

The former description of the Universe is so far missing a very important ingredient: it is completely homogeneous, lacking any kind of actual structure, such as clusters, galaxies, stars... We expect small inhomogeneities to be created at some point in the Universe history. In this section, we will see how they get created by Inflation, how to treat them mathematically, and which are their main features.

1.3.1 Primordial perturbations in quantized slow-roll inflation

In order to study perturbations on top of the FLRW metric, we have to write a perturbed version of the metric (1.1), $\tilde{g}_{\mu\nu} := g_{\mu\nu} + \delta g_{\mu\nu}$. Its particular shape depends upon some gauge freedom. In the context of Inflation, we normally work in the *comoving gauge*, in which the choice of coordinates is such that the scalar momentum density vanishes, i.e. the 3-surfaces of constant time are everywhere orthogonal to the fluid's flow. In this gauge, the spatial part of the perturbed metric reads

$$\delta g_{ij} = a^2(t)(-2)\zeta(t, \mathbf{x})\delta_{ij} + a^2(t)h_{ij}(t, \mathbf{x}), \quad (1.27)$$

where $\zeta(t, \mathbf{x})$ is a scalar and $h_{ij}(t, \mathbf{x})$ is a transverse, traceless tensor. In this gauge, the curvature of the 3-surfaces of constant time is $R = 4/a^2\nabla^2\zeta$. Hence, we call the scalar ζ *comoving curvature perturbation*.³ On the other hand, the tensor h_{ij} characterises the *gravitational waves*, which we will not study here.

The Einstein equations of the perturbed metric allow us to calculate the remaining metric perturbations $\delta g_{0\mu}$ also in terms of (ζ, h_{ij}) . Substituting them into the action for the scalar field, eq. (1.22), and expanding in powers of ζ , we arrive at the *quadratic* action for the comoving curvature perturbation (terms of higher order are ignored)

$$S_2 = \frac{1}{2} \int d^4x a^3 \left(\frac{\dot{\phi}}{H} \right)^2 \left[\dot{\zeta}^2 - \frac{1}{a^2} (\partial_i \zeta)^2 \right]. \quad (1.28)$$

The definition of the comoving gauge, with synchronous 3-surfaces orthogonal to the fluid's flow, implies that the density of the fluid must be constant over those surfaces, in this case $\phi(t, \mathbf{x}) = \bar{\phi}(t)$ over those surfaces, since it is the only fluid populating the Universe.

After all remaining gauge freedom is removed using the Einstein equations, we are left with a single scalar degree of freedom, ζ , and two degrees of freedom for each of the two independent tensor perturbations h_{ij} (spin 2, massless). All

³Notice that it is more common in the literature (see e.g. [40]) to refer to the comoving curvature perturbation with the symbol \mathcal{R} .

five of them are sourced by the only degree of freedom of the theory: the scalar field ϕ .

Now, one can solve the equations of motion for the comoving curvature perturbation arising from the action (1.28). This is often done in terms of the *Mukhanov variable*

$$v := z\zeta, \quad z^2 := 2a^2\epsilon. \quad (1.29)$$

We quantise the action in terms of this variable and derive the equations of motion in the Fourier transformed 3-space, named *Mukhanov-Sasaki equation* [33, 37]:

$$v_{\mathbf{k}}'' + \left(k^2 - \frac{z''}{z}\right)v_{\mathbf{k}} = 0, \quad (1.30)$$

where the primes mean derivatives with respect to conformal time. Conventionally, we impose as initial conditions at the beginning of Inflation, or *choose as a vacuum*, that the mode functions are Minkowski states,

$$\lim_{\tau \rightarrow -\infty} v_{\mathbf{k}}(\tau) = \frac{1}{\sqrt{2k}} e^{-ik\tau}, \quad (1.31)$$

a choice called *Bunch-Davies vacuum* [12]. Solving in the approximation $H \simeq \text{const}$, $\epsilon = \text{const}$ (quasi de-Sitter Universe), we arrive at the solution for the modes of the comoving curvature perturbation in terms of the Mukhanov variable:

$$v_{\mathbf{k}}(\tau) = \frac{1}{\sqrt{2k}} e^{-ik\tau} \left(1 - \frac{i}{k\tau}\right). \quad (1.32)$$

Note that this equation resembles that of an harmonic oscillator with a time dependent mass $m^2(\tau) := -z''/z \simeq 2/\tau^2$, where the last approximation is true in the quasi de-Sitter limit. It becomes immediately obvious that the modes of comoving curvature perturbations are oscillatory unless the exponent $k\tau$ vanishes. In the quasi de-Sitter approximation, $H = \text{const}$, $\epsilon = \text{const}$, we have for a conformal time interval $\tau \simeq (aH)^{-1}$. This means that whenever $k \ll aH$, the curvature perturbations are *constant*:

$$\lim_{k/(aH) \rightarrow 0} \dot{\zeta}(t, \mathbf{k}) = 0. \quad (1.33)$$

Remembering the definition of the comoving Hubble radius, eq. (1.15), $r_{\text{H}} = 1/aH$, we learn that this *freeze-out scale* corresponds precisely to the Hubble sphere.⁴

⁴It is common in the literature to refer to this scales as *sub-* or *super-Hubble horizon*, or even worse, simply *sub-* or *super-horizon*. As explained in section 1.1.2, the Hubble radius is not a cosmological horizon, as it is manifested in the context of Inflation by how scales exit and re-enter it; instead, cosmological horizons can only ever be escaped (in the case of the event horizon) or entered (in the case of the particle horizon) a single time, the reverse process not being possible.

Thus, we state that the comoving curvature perturbation is conserved on super-Hubble scales. Since in the de-Sitter Universe the Hubble sphere gets smaller with time, as Inflation progresses modes of decreasing wavelengths get frozen as they exit the Hubble sphere. Once Inflation is finished and we return to a radiation-dominated Universe, the Hubble sphere starts growing, eventually allowing for interactions between regions separated by previously frozen distances. Those interactions give birth to the CMB anisotropies that we can see today, as explained in section 1.4.

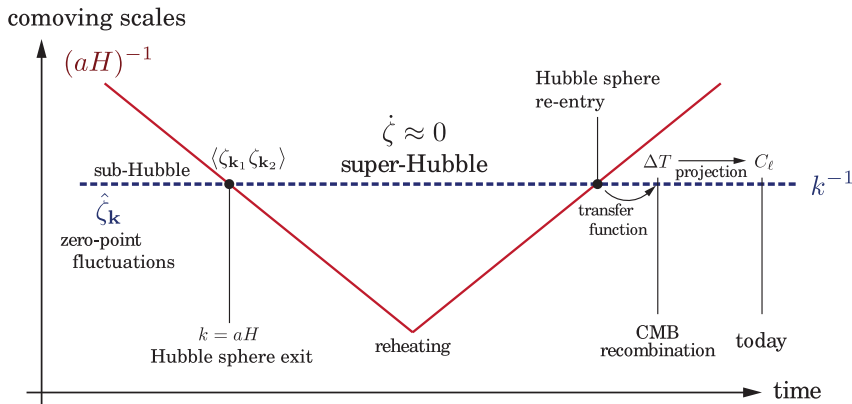


Figure 1.3: Depiction of how a mode of a particular comoving scale (dashed) leaves the Hubble sphere (solid) during Inflation, getting frozen, and how it eventually re-enters during the radiation-dominated regime. Figure from [10].

In the next section, we will review the treatment of the correlation functions of curvature perturbations, which ultimately determine the CMB observables. After it, we will discuss the main features of the perturbations created in this inflationary setting: namely, that they are nearly *scale-invariant*, and nearly *gaussian*.

1.3.2 Correlation functions – spectrum and bispectrum

Here we focus on studying the statistical properties of the perturbations, which we assume to be generated by a random process. In particular, we are interested in correlations between its values in different points of space. In Fourier space, the n -point correlation functions are transformed simply to products of the function itself. We define the 2- and 3-point correlation functions in the Fourier space, called respectively *power spectrum* and *bispectrum*, as

$$(2\pi)^3 \delta_D^{(3)}(\mathbf{k}_1 + \mathbf{k}_2) P_\zeta(\mathbf{k}_1) := \zeta(\mathbf{k}_1)\zeta(\mathbf{k}_2), \quad (1.34a)$$

$$(2\pi)^3 \delta_D^{(3)}(\mathbf{k}_1 + \mathbf{k}_2 + \mathbf{k}_3) B_\zeta(\mathbf{k}_1, \mathbf{k}_2) := \zeta(\mathbf{k}_1)\zeta(\mathbf{k}_2)\zeta(\mathbf{k}_3). \quad (1.34b)$$

Of course, we can go on and study higher order correlation functions, but those two are enough to describe the current data with enough precision.

We are interested in studying not the particular realisation of the perturbations in our Universe, but the properties of the probability distribution that generated them. These properties show up when averaging over the *ensemble* of all possible *realisations* of the random field ζ which may have been generated by the same physical mechanism. We will denote this ensemble average as $\langle \cdot \rangle$. Since we expect that mechanism to generate *statistically* isotropic perturbations, the spectrum and bispectrum must depend on norms only, not directions, so the ensemble-averaged correlation functions are

$$(2\pi)^3 \delta_{\text{D}}^{(3)}(\mathbf{k}_1 + \mathbf{k}_2) P_{\zeta}(k_1) = \langle |\zeta(\mathbf{k}_1)|^2 \rangle, \quad (1.35a)$$

$$(2\pi)^3 \delta_{\text{D}}^{(3)}(\mathbf{k}_1 + \mathbf{k}_2 + \mathbf{k}_3) B_{\zeta}(k_1, k_2, k_3) := \langle \zeta(\mathbf{k}_1)\zeta(\mathbf{k}_2)\zeta(\mathbf{k}_3) \rangle. \quad (1.35b)$$

Notice that in the spectrum formula we have made use of the fact that the curvature perturbation is a real function in the space of positions. On the other hand, notice that we have substituted the dependence of the bispectrum from the vectors $(\mathbf{k}_1, \mathbf{k}_2)$, to the norms (k_1, k_2, k_3) . We have done so because, though the first two vectors and the delta completely determine the third vector, once the ensemble average erases the direction information, the norms of the two first vectors do not specify that of the third. There is a range of values of k_3 allowed for each pair (k_1, k_2) , which are given by the *triangle condition* imposed by the delta:

$$\mathbf{k}_1 + \mathbf{k}_2 + \mathbf{k}_3 = 0. \quad (1.36)$$

The triangle condition enforces the k_i 's to live inside a regular-triangular pyramid in the (k_1, k_2, k_3) space (see fig. 1.4, and for a review see [31]). Using the *triangular inequality*, for every permutation $(i, j, k) \in \text{Perm}(1, 2, 3)$:

$$\mathbf{k}_i = -(\mathbf{k}_j + \mathbf{k}_k) \Rightarrow k_i = |\mathbf{k}_j + \mathbf{k}_k| \Rightarrow |k_j - k_k| \leq k_i \leq k_j + k_k, \quad (1.37)$$

where the equality in the last inequation defines the three sides of the pyramid for $i = 1, 2, 3$.

Since our experiments have a limited precision, we assume that there is a minimum scale accessible to us, i.e, a maximum wave number K such that $k_i \leq K, \forall i$, then

$$k_1 + k_2 + k_3 \leq |k_1 + k_2| + k_3 \leq 2k_3 \leq 2K \quad (1.38)$$

and the pyramid turns into a regular tetrahedron with base in the plane

$$k_1 + k_2 + k_3 = 2K \quad (1.39)$$

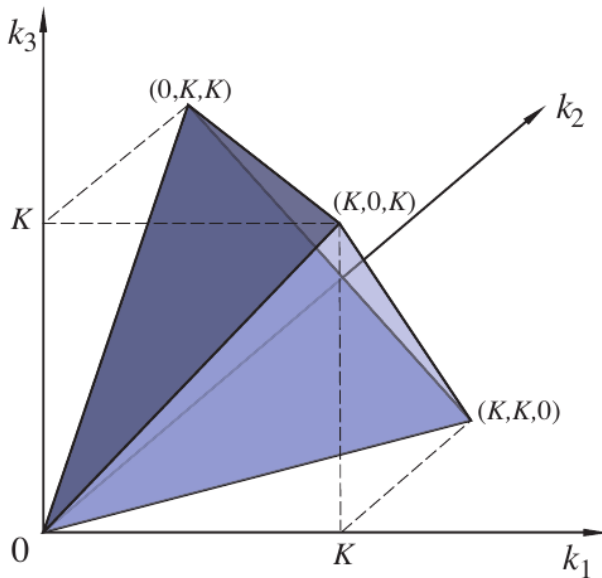


Figure 1.4: Regular Tetrahedron of allowed wave-numbers, limited by the conditions of eq. (1.37) and (1.39). Figure from [31, fig. 2]

Regarding the shape of the $(\mathbf{k}_1, \mathbf{k}_2, \mathbf{k}_3)$ triangles, three different limits are often studied:

<i>squeezed or local</i>	$k_3 \ll k_1 \simeq k_2$	<i>edges of the tetrahedron</i>
<i>equilateral</i>	$k_3 \simeq k_1 \simeq k_2$	<i>axis of the tetrahedron</i>
<i>flattened</i>	$k_3 \simeq k_1 + k_2$	<i>heights of the faces of the tetrahedron</i>

1.3.3 Predictions of slow-roll inflation

Power spectrum – scale-invariance

In the QFT framework described in section 1.3.1, one can calculate the predicted power spectrum for the comoving curvature perturbation [12]

$$P_\zeta(k) = \frac{1}{4k^3} \left. \frac{H^2}{\epsilon} \right|_{k=aH}, \quad (1.40)$$

where the spectrum for each comoving wavelength k can be evaluated when said length becomes larger than the (shrinking) Hubble sphere, thus getting *frozen*. We can define a *dimensionless* version of the power spectrum as

$$\mathcal{P}(k) := \frac{k^3}{2\pi^2} P_\zeta(k) = \frac{1}{8\pi^2} \left. \frac{H^2}{\epsilon} \right|_{k=aH}. \quad (1.41)$$

What are the particular features of this spectrum? From the slow-roll conditions we know that during Inflation H decreases slowly as ϵ grows slowly (i.e. the kinetic energy increases), so for the smaller wavelengths (higher k) we expect $\mathcal{P}(k)$ to *slowly* decrease, according to (1.41). The spectrum will thus be nearly *scale-invariant*, with a little less power for higher k . Notice that scale-invariance is a natural consequence of the lack of large-scale standard rulers in the early Universe.

When dealing with constraining the power spectrum with observations, we often prefer a more phenomenological parametrisation that reveals more directly its dependence on the scale. We start by assuming a general power law spectrum, $\mathcal{P}(k) \sim k^n$, and then Taylor-expand it in its logarithm around a pivot scale k_0 :

$$\log \frac{\mathcal{P}(k)}{\mathcal{P}(k_0)} \simeq 0 + (n_s - 1) \log \frac{k}{k_0} + \frac{\alpha_s}{2} \left(\log \frac{k}{k_0} \right)^2 + \dots, \quad (1.42)$$

where we have defined the *spectral index*⁵ n_s and the *running* α_s , and ignored higher order terms. For a nearly scale invariant spectrum, we should get very small values of $n_s - 1$ and an even smaller for α_s , which can often be neglected. Calling A_s the value of the spectrum at the pivot scale, we arrive at the very well known expression

$$\mathcal{P}(k) \simeq A_s \left(\frac{k}{k_0} \right)^{n_s - 1}. \quad (1.43)$$

The value of the spectral index can be calculated from eq. (1.40):

$$n_s - 1 = -2\epsilon - \eta, \quad (1.44)$$

where we omit contributions from higher powers of ϵ and η . We don't know the precise values for ϵ and η , but we know that they result in a value for n_s close to 1 but slightly smaller. This small deviation from unity constitutes a strong test for the Inflation framework described here: slow-roll, single-field inflation with canonical kinetic terms and Bunch-Davies vacuum. This small deviation was confirmed by WMAP and later by Planck. The latter finds a 95% c.l. interval [8]

$$n_s = 0.9616 \pm 0.0094. \quad (1.45)$$

Bispectrum – gaussianity

One of the defining features of a Gaussian distribution is that it is completely characterised by its mean and its variance, strictly its 1st order momentum and 2nd order central momentum. Higher order momenta, are completely determined by those two. In particular, all the odd momenta are zero.

⁵We would normally call *spectral index* the n in $\mathcal{P}(k) \sim k^n$, but in cosmology it is customary to give that name to the difference $n_s - 1$.

The fluctuations of the inflaton have a mean value of zero, and their higher order momenta are given by its n -point correlation functions (we just described the predicted 2-point correlation). If inflationary primordial fluctuations were gaussian, they would be completely determined by a constant power spectrum, and have an vanishing bispectrum.

The contributions to the bispectrum would arise mainly from the order-3 terms in the action of the comoving curvature perturbation. Those terms account for interactions between the fields present during inflation. Since the only field in the theory is minimally coupled to gravity, we expect to have only a very small contribution to the bispectrum. The full bispectrum for single-field, slow-roll inflation was first calculated in [32, 4] and it is

$$B_{\zeta}(k_1, k_2, k_3) = \frac{(2\pi)^4 \mathcal{P}(\sum_i k_i)^2}{(k_1 k_2 k_3)^2} \frac{1}{8k_1 k_2 k_3} \times \left[(3\epsilon - 2\eta) \sum_{i=1}^3 k_i^3 + \epsilon \sum_{i \neq j} k_i k_j^2 + \epsilon \frac{4}{\sum_{i=1}^3 k_i} \sum_{i \neq j} k_i^2 k_j^2 \right]. \quad (1.46)$$

Now, in the same way we did with the power spectrum, we often define a dimensionless version of the bispectrum by factoring out $(k_1 k_2 k_3)^{-2}$, and, in order to compare its value with that of the power spectrum, also a factor of $\mathcal{P}(\sum_i k_i)^2$, defining the *shape function* $\mathcal{S}(k_1, k_2, k_3)$:

$$\mathcal{S}(k_1, k_2, k_3) := \frac{(k_1 k_2 k_3)^2}{(2\pi)^4 \mathcal{P}(\sum k)^2} B_{\zeta}(k_1, k_2, k_3). \quad (1.47)$$

(Unfortunately, there is no unique convention in the literature for the prefactor)

Factoring out this scaling, we can now see how the bispectrum is suppressed by $\mathcal{O}(\epsilon, \eta)$ with respect to the power spectrum. We do not know the real value of the slow-roll parameters, but the bounds given by eqs. (1.44) and (1.45) make us expect a very small bispectrum, which, together with a nearly scale-invariant power spectrum are a strong indication for slow-roll single-field inflation. Both WMAP and Planck confirm the smallness of the bispectrum when fitting the shape in eq. (1.46).

Notice that in the last sentence we explicitly stated which shape of the bispectrum was fitted when quoting the amount of non-gaussianity. We must always do so, and the reason is that the many possible configurations of momenta in which the bispectrum can be evaluated (see fig. 1.4) leave room for very diverse functional forms with very different dependencies on the configurations. Given a data set containing a significant amount on non-gaussianity in a particular shape, if we try to fit a shape much different from that of the signal we would get a small amplitude for it. Being aware of this, we should be careful about making general statements of the amount of non-gaussianity in e.g. the CMB data, since this *amount*, in principle, depends on its shape. We are about to describe

a model that predicts a distinct shape for the primordial bispectrum, and so do other inflationary settings. A precise measurement of the cosmological observables which are most informative about the primordial bispectrum (specially the CMB bispectrum) can be determinant to distinguish among different inflationary scenarios.

1.3.4 Beyond the simplest model – Transient reductions in the speed of sound

Inflation occurs at high energy scales in which our knowledge of the field content, prior to cosmological constraints, is almost non-existent. The presence of multiple fields during Inflation would produce a very rich phenomenology that could also be constrained in principle by cosmological observations (different, also rich phenomenology can arise too from other alternatives to the simplest inflationary scenario, such as brief interruptions of the slow-roll regime or different choices of the vacuum).

As we argued in the last section, the predictions of slow-roll, single-field inflation are well within the constraints of CMB observations, their most direct probe. This fact motivates us to approach the presence of multiple fields during inflation under the hypothesis that they are significantly heavy. In this regime, we expect to be able to integrate out those heavy degrees of freedom and obtain an effectively-single-field theory in which the effect of the background enters through effective operators in the action, and the inflaton direction fulfils a slow-roll regime. Small excitations of the heavy degrees of freedom during inflation might produce, through the effective operators, potentially detectable deviations from the predictions of a purely single-field framework.

To achieve that, several different approaches are possible. In this section we will not discuss the details of the procedure, but instead we start from the effective action, after integrating out the heavy degrees of freedom, of the field $\pi(t, \mathbf{x})$, which represents displacements along the background trajectory in the effective potential. The quadratic and cubic action for this field are [13]

$$S_2 = \int d^4x a^3 \epsilon H^2 \left(\frac{\dot{\pi}^2}{c_s^2} - \frac{1}{a^2} (\nabla\pi)^2 \right), \quad (1.48a)$$

$$S_3 = \int d^4x a^3 \epsilon H^2 \times \left\{ -2Hs c_s^{-2} \pi \dot{\pi}^2 - (1 - c_s^{-2}) \pi \left[\dot{\pi}^2 - \frac{1}{a^2} (\nabla\pi)^2 \right] \right\}, \quad (1.48b)$$

where we are neglecting higher order slow-roll corrections. Notice the introduction of the speed of sound c_s , and the derived quantities u and s , defined as:

$$u := 1 - c_s^{-2}, \quad s := \frac{\dot{c}_s}{c_s H}. \quad (1.49)$$

The action above neglects terms of higher order in u and s . The speed of sound in the effective field theory can be related to the angular velocity $\dot{\theta}$ of the field π whenever it finds a *turn* in the inflationary trajectory:

$$c_s^{-2} = 1 + \frac{4\dot{\theta}^2}{\frac{k^2}{a^2} + M_{\text{eff}}^2}, \quad (1.50)$$

where M_{eff}^2 is the effective mass of the mode perpendicular to the trajectory in field space. Therefore, a turn between two straight segments of the trajectory produces a momentary reduction in the speed of sound. As the action above is perturbative in terms of u and s , the reduction in the speed of sound cannot be too big nor too quick; at the same time, we keep at all times a slow-roll regime, and expect the contribution of the slow-roll corrections to be much smaller than that of the speed of sound, which must be dominating the evolution during the turns. Altogether, the theoretical framework presented here is well defined in the regime of *mild and moderately sharp transient reductions*:

$$\mathcal{O}(\epsilon, \eta) \ll \max(u, s) \ll 1. \quad (1.51)$$

Now we will take a look at the possible observable consequences of this regime. To do that, we need to relate the inflaton direction π with the comoving curvature perturbation ζ :

$$\zeta = -H\pi. \quad (1.52)$$

In terms of the adiabatic curvature perturbation, the quadratic action of the inflationary mode is

$$S_2 = \underbrace{\int d^4x a^3 \epsilon \left[\dot{\zeta}^2 - \frac{(\nabla\zeta)^2}{a^2} \right]}_{S_{2,0}} + \underbrace{\int d^4x a^3 \epsilon (-u) \dot{\zeta}^2}_{\delta S_2}. \quad (1.53)$$

Notice that the first part of the action, $S_{2,0}$, corresponding to the case $c_s = 1$, is similar to the canonical slow-roll action eq. (1.28), and has the same phenomenology, producing the well known power spectrum of eq. (1.41). The new, interesting term δS_2 accounts for the reductions in the speed of sound, and produces a perturbation of the (nearly) scale-invariant power spectrum, which can be calculated using the *in-in formalism* [27, 41] for the case of a small, transient reduction in c_s , to first order in $u \equiv 1 - c_s^{-2}$ [3]:

$$\frac{\Delta\mathcal{P}}{\mathcal{P}}(k) = k \int_{-\infty}^0 d\tau u(\tau) \sin(2k\tau), \quad (1.54)$$

where $k \equiv |\mathbf{k}|$, \mathcal{P} is the featureless power spectrum with $c_s = 1$ defined by eq. (1.41), and τ is the conformal time. This very important expression shows

precisely how changes in the speed of sound, within the regime described here, seed features in the primordial power spectrum of curvature perturbations. Those features are given by a simple Fourier transform in conformal time, assuming $c_s = 1$ at the beginning ($\tau = -\infty$) and the end of inflation ($\tau = 0$).

We can also calculate the resulting bispectrum from the cubic action in terms of the adiabatic curvature perturbation, using the in-in formalism, at first order on u and s , and disregarding slow-roll contributions [3]:

$$\begin{aligned} \Delta B_\zeta(\mathbf{k}_1, \mathbf{k}_2, \mathbf{k}_3) = & \frac{(2\pi)^4 \mathcal{P}^2}{(k_1 k_2 k_3)^2} \left\{ -\frac{3}{2} \frac{k_1 k_2}{k_3} \left[\frac{1}{2k} \left(1 + \frac{k_3}{2k} \right) \frac{\Delta \mathcal{P}}{\mathcal{P}} - \frac{k_3}{4k^2} \frac{d}{d \ln k} \frac{\Delta \mathcal{P}}{\mathcal{P}} \right] + \dots \right. \\ & + \frac{1}{4} \frac{k_1^2 + k_2^2 + k_3^2}{k_1 k_2 k_3} \left[\frac{1}{2k} \left(4k^2 - (k_1 k_2 + \dots) - \frac{k_1 k_2 k_3}{2k} \right) \frac{\Delta \mathcal{P}}{\mathcal{P}} \right. \\ & \left. \left. - \frac{k_1 k_2 + \dots}{2k} \frac{d}{d \ln k} \frac{\Delta \mathcal{P}}{\mathcal{P}} + \frac{k_1 k_2 k_3}{4k^2} \left(\frac{d}{d \ln k} \right)^2 \frac{\Delta \mathcal{P}}{\mathcal{P}} \right] \right\}, \quad (1.55) \end{aligned}$$

where $k_i := |\mathbf{k}_i|$, $k := 1/2 \sum_{i=1}^2 k_i$, and \mathcal{P} , $\Delta \mathcal{P}/\mathcal{P}$ and its derivatives are evaluated at k . The ellipsis \dots means a sum over all possible permutations of $(1, 2, 3)$ on the indices of the term previous to it. Note that in the squeezed limit $k_i \ll k_j \simeq k_k$ we recover the single-field consistency condition of [32, 14].

It becomes immediately clear how a reduction in the speed of sound seeds correlated perturbations in both the power spectrum and bispectrum. In the first part of this thesis, we study how this correlation can be exploited to try to detect reductions in the speed of sound in CMB (and LSS) data.

As a final remark, note that, though we have related the reduction in the speed of sound to the angular velocity along a turn, the result above is independent of the physical origin of such reduction. Different high energy realisations of the reduction would produce different effective operators in the cubic action, making the realisations distinguishable at the level of the bispectrum [13, 2].

1.4 The Cosmic Microwave Background

1.4.1 Statistical properties – spectrum and bispectrum

We expect the temperature anisotropies in the CMB to be the most informative probe of the primordial perturbations generated by inflation. As we will see later, the statistical properties of the primordial n -point correlation functions are related to the corresponding correlations of temperature anisotropies in the CMB sky. We will leave the description of the physical effects leading from primordial to CMB anisotropies for the next section, and we start here by describing the treatment of correlation functions of the temperature anisotropies in the CMB sky.

Since the anisotropies are projected on the 2-sphere defined by all possible directions in the sky given by the unit vector $\hat{\mathbf{n}}$, we use as the basis of the transformation the spherical harmonics:

$$\frac{\Delta T}{T}(\hat{\mathbf{n}}) = \sum_{\ell m} a_{\ell m} Y_{\ell m}(\hat{\mathbf{n}}) \quad (1.56)$$

Notice how the harmonic-transformed perturbation, instead of a continuous function like the primordial perturbation $\zeta(\mathbf{k})$ was, is now a discrete series of coefficients $a_{\ell m}$, due to the finitude of the space over which the transformation is taken: a 2-sphere. The integer sub-index $\ell \geq 0$ characterises the angular periodicity of $Y_{\ell m}$, its *period* being $(2\pi/\ell)$ rad or $360^\circ/\ell$. For each ℓ , the values of the integer index $m \in [-\ell, \ell]$ represent the different relative directions in which the angular variation of $Y_{\ell m}$ can be realised.

As we did with primordial perturbations, we define the *CMB power spectrum* C_ℓ as the 2-point correlation function averaged over all possible realisations of the random fluctuations:

$$\langle a_{\ell_1 m_1} a_{\ell_2 m_2}^* \rangle = \delta_{\ell_1 \ell_2} \delta_{m_1 m_2} C_{\ell_1}. \quad (1.57)$$

In an analogous way to the primordial spectrum's lack of information of direction, $\mathcal{P}(\mathbf{k}) \equiv \mathcal{P}(k)$, the CMB power spectrum carries no information on direction either, $C_{\ell m} \equiv C_\ell$, imposed by the delta $\delta_{m_1 m_2}$.

Equivalently, one could have calculated directly the correlation between two temperature anisotropies, and averaged them over all possible realisations of the CMB sky, getting

$$\left\langle \frac{\Delta T}{T}(\hat{\mathbf{n}}_1) \frac{\Delta T}{T}(\hat{\mathbf{n}}_2) \right\rangle = \sum_{\ell} \frac{2\ell + 1}{4\pi} C_\ell P_\ell(\cos \theta), \quad (1.58)$$

where P_ℓ are the Legendre polynomials and θ is the angle between the direction $\hat{\mathbf{n}}_1$ and $\hat{\mathbf{n}}_2$.

We define the 3-point correlation function, or *reduced CMB bispectrum* as

$$\langle a_{\ell_1 m_1} a_{\ell_2 m_2} a_{\ell_3 m_3} \rangle := \mathcal{G}_{\ell_1 \ell_2 \ell_3}^{m_1 m_2 m_3} b_{\ell_1 \ell_2 \ell_3}, \quad (1.59)$$

where we make use of the so-called *Gaunt integral*:

$$\mathcal{G}_{\ell_1 \ell_2 \ell_3}^{m_1 m_2 m_3} = \sqrt{\frac{(2\ell_1 + 1)(2\ell_2 + 1)(2\ell_3 + 1)}{4\pi}} \begin{pmatrix} \ell_1 & \ell_2 & \ell_3 \\ 0 & 0 & 0 \end{pmatrix} \begin{pmatrix} \ell_1 & \ell_2 & \ell_3 \\ m_1 & m_2 & m_3 \end{pmatrix}, \quad (1.60)$$

where the matrices represent Wigner 3- j symbols (we will show the origin of the Gaunt integral in the next section). We can also write the inverse equation to (1.59):

$$b_{\ell_1 \ell_2 \ell_3} = \sum_{m_i} \mathcal{G}_{\ell_1 \ell_2 \ell_3}^{m_1 m_2 m_3} \langle a_{\ell_1 m_1} a_{\ell_2 m_2} a_{\ell_3 m_3} \rangle. \quad (1.61)$$

Notice now that the reduced CMB bispectrum has no directional information (m_i), as expected, since we assumed isotropy. The only directional information, which is geometrical, not physical, is inside the Gaunt integral, which takes the rôle of the deltas in (1.57). Those deltas would impose some constraints on $\langle a_{\ell_1 m_1} a_{\ell_2 m_2}^* \rangle$ which were not visibly present in C_ℓ . In the same way, the fact that the Gaunt integral contains those two 3- j symbols imposes some *selection rules* in $\langle a_{\ell_1 m_1} a_{\ell_2 m_2} a_{\ell_3 m_3} \rangle$ that cannot be seen directly on $b_{\ell_1 \ell_2 \ell_3}$. In particular, the ℓ_i 's must form a triangle of even perimeter, i.e.⁶

$$\frac{\ell_1 + \ell_2 + \ell_3}{2} \in \mathbb{Z}, \quad (1.62a)$$

$$|\ell_j - \ell_k| \leq \ell_i \leq \ell_j + \ell_k, \quad \forall (i, j, k) \in \text{Perm}(1, 2, 3). \quad (1.62b)$$

The second condition is analogous to the one imposed over the wave numbers in the primordial bispectrum, (1.36): both wave numbers and harmonic indices must form triangles in order to contribute to each bispectrum. In particular, in the harmonic space, the triangle must have even perimeter.

The triangle condition determines a tetrahedral cone for the ℓ_i 's, as it did for the k_i 's. In the case of the wave numbers, the cone was cut into a pyramid by the existence of a maximum observable wave number K . Here, correspondingly, we assume a maximum precision L , such that $\ell_1, \ell_2, \ell_3 \leq L$. But here the lack of a vectorial condition like $\sum_i \mathbf{k}_i = 0$ lets the cone be extended up to the edges of the cube limited by L , forming not a pyramid but a *bi-pyramid* (see [19, fig. 2], where it is called *tetrapyd*) with apices in $(0, 0, 0)$ and (L, L, L) , limited by the planes

$$\ell_i = \ell_j + \ell_k, \quad \ell_i = L, \quad \forall (i, j, k) \in \text{Perm}(1, 2, 3). \quad (1.63)$$

Notice that the observed quantity in the sky is the *angle-averaged CMB bispectrum*, defined as

$$B_{\ell_1 \ell_2 \ell_3} := \sum_{m_i} \begin{pmatrix} \ell_1 & \ell_2 & \ell_3 \\ m_1 & m_2 & m_3 \end{pmatrix} \langle a_{\ell_1 m_1} a_{\ell_2 m_2} a_{\ell_3 m_3} \rangle, \quad (1.64)$$

or, inversely

$$\langle a_{\ell_1 m_1} a_{\ell_2 m_2} a_{\ell_3 m_3} \rangle = \begin{pmatrix} \ell_1 & \ell_2 & \ell_3 \\ m_1 & m_2 & m_3 \end{pmatrix} B_{\ell_1 \ell_2 \ell_3}, \quad (1.65)$$

and which fulfils the following relation with the reduced bispectrum

$$B_{\ell_1 \ell_2 \ell_3} = \sqrt{\frac{(2\ell_1 + 1)(2\ell_2 + 1)(2\ell_3 + 1)}{4\pi}} \begin{pmatrix} \ell_1 & \ell_2 & \ell_3 \\ 0 & 0 & 0 \end{pmatrix} b_{\ell_1 \ell_2 \ell_3}. \quad (1.66)$$

⁶Notice that the second condition, provided that all ℓ_i 's are positive numbers, needs only be checked for a particular permutation of $(1, 2, 3)$, which implies that it is satisfied for all of them.

1.4.2 From inflationary primordial fluctuations to CMB anisotropies

In section 1.3.1 we described the curvature perturbations created by slow-roll, single-field inflation, and proved that their modes get frozen when their respective wave length exists the Hubble sphere.⁷ The very fact that they remain frozen while they are outside the Hubble sphere is what allows us to learn anything about Inflation, since we know close to nothing about the physics going on right after the end of inflation.

After the end of inflation, the Universe becomes filled with radiation (part of which decouples as matter at some point), and the comoving curvature perturbations created by Inflation source perturbations in the density of the radiation field. In slow-roll, single field inflation the only degree of freedom present is the scalar field, which sources curvature perturbations ζ in the synchronous 3-surfaces. As the only degree of freedom driving the dynamics of the Universe, at each point of the fluid, the curvature perturbation can be used as a clock $t_{\mathbf{x}} = t_{\mathbf{x}}(\zeta)$. Then, the small spatial variations can be understood as inflation being slightly ahead or behind at each point by a small quantity $\delta t(\mathbf{x})$. This small, continuous time shift causes the different regions to have expanded a slightly different amount – the surfaces of constant time are not homogeneous any more, or, equivalently, the surfaces of homogeneity are not flat anymore, which is another way to understand why *curvature perturbations* in the 3-space are generated.

Let us look at the density perturbation of the fluid i at some point after inflation, in a surface of constant time t . This 3-surface is nearly homogeneous, with an energy density $\bar{\rho}_i(t)$. The real, perturbed density of the fluid i , for a small time shift, can be written as

$$\rho_i(t, \mathbf{x}) = \bar{\rho}_i(t + \delta t(\mathbf{x})) \simeq \bar{\rho}_i(t) + \dot{\bar{\rho}}_i(t)\delta t(\mathbf{x}), \quad (1.67)$$

and a similar expression for the pressure. Defining $\delta\rho_i(t, \mathbf{x}) := \dot{\bar{\rho}}_i(t)\delta t(\mathbf{x})$ and substituting the time derivative of the density with the continuity equation (1.5b), one arrives at the equality

$$\frac{\delta\rho_i}{\rho_i + p_i} = -3H\delta t(x), \quad (1.68)$$

where one should notice that the right term is independent of the species. This independence of the particular fluid is a consequence of there being a *single* degree of freedom $\delta t(\mathbf{x})$ sourcing the perturbations, and defines *adiabatic perturbations*.

Before continuing, a caveat is in order: in general, the linear perturbations of the different fluids, photons, baryons or CDM, are possibly coupled with each other in different ways, depending on the mechanism that generated them. They

⁷Formally, we have only proven that perturbations are conserved during inflation, but still would have to prove that they keep frozen after inflation has ended. The proof for adiabatic perturbations can be found in [40], and in an alternative formulation in [39].

can be expanded by two orthogonal components: *entropy perturbation*, which imply local variations of the relative number density, but keeping the total energy density constant (and thus the curvature of the local space-time, hence also called *isocurvature perturbations*); and *adiabatic perturbations*, in which there is no energy exchange between the different fluids, and are defined by equation (1.68). Slow-roll single-field inflation produces adiabatic perturbations, while in multiple-field inflation we expect several degrees of freedom seeding perturbations, thus creating a combination of adiabatic and isocurvature perturbations. Only because we assumed slow-roll single-field inflation, we are able to choose such a synchronous gauge that traces the perturbations in all fluids simultaneously, showing explicitly the defining property of adiabatic perturbations, eq. (1.68).

Current CMB data clearly favours *adiabatic perturbations* as the only necessary ones to describe the universe today, while restricting the size of isocurvature perturbations to be negligible [6].

The next step to relate the primordial curvature perturbations with the CMB temperature perturbations is to study the physical processes that the perturbation modes undergo after entering the Hubble sphere. The nature of those processes is well known, and can be summarised into a series of *transfer functions* $\Delta_\ell(k)$, which project the primordial curvature perturbation to the harmonic coefficients of the CMB sky as

$$a_{\ell m} = 4\pi(-i)^\ell \int \frac{d^3\mathbf{k}}{(2\pi)^3} \Delta_\ell(k) \zeta(\mathbf{k}) Y_{\ell m}(\hat{\mathbf{k}}). \quad (1.69)$$

The effect of the transfer functions in the power spectrum can be divided in two sets of contributions: those acting at scales which are super-Hubble at the time of recombination, and those that had entered the Hubble sphere earlier, divided approximately by the scale of the multipole $\ell \approx 90$, as discussed in section 1.2.1.

Of the first ones, the main contribution comes from the *Sachs-Wolfe effect*, which is the gravitational redshift that the photons suffer at the last scattering surface due to the differences in the local gravitational potential. A smaller contribution comes from the *Integrated Sachs-Wolfe effect*, which consists on the gravitational redshift that the photons undergo during their journey to us, due to the difference in energy between descending and climbing a potential in an expanding, radiation- or dark matter-dominated Universe. The relevant part of the power spectrum, $l \lesssim 90$, results in a direct processing of the primordial one, keeping flat bar a factor $\ell(\ell + 1)$ coming from the projection of the flat waves in \mathbf{k} over the spherical sky.

At sub-Hubble scales, the cosmic fluid has been able to undergo local physical processes between leaving the Hubble-sphere and the last scattering surface. Therefore, on top of the Sachs-Wolfe spectrum, we will see the effect of these processes. The cold dark matter (CDM) fluid is decoupled from an initially coupled fluid of baryons and photons. CDM dominates the gravitational potential, and

the baryons+photons fluid oscillates inside the potential wells due to the photon radiation pressure. These stationary oscillations produce, at the time of decoupling of photons and baryons in the last scattering surface, the series of *acoustic peaks* that we can see on the CMB power spectrum. These peaks of approximately equal height in the spectrum are actually damped at small scales by the fact that the decoupling did not occur instantly, and the photons underwent scattering at scales of their mean free path at that time. This last effect is called *Silk damping*.

The effect of those physical processes in the CMB power spectrum can be seen in figure 1.5(a) of section 1.4.3. For a detailed study of them we refer the reader to thorough reviews such as [17]. The transfer functions are often computed with the help of cosmological codes, such as CLASS or CAMB. Here it is enough to keep track of the parameters of the cosmological model implied in them: (1) the ones referring to the Λ CDM background, namely the value of the expansion rate today (H_0) and the densities of baryons and CDM (Ω_b and Ω_{CDM}); (2) those referring to late-time effects, the optical depth due to reionisation τ_{reio} being the only one that we can constrain (the rest are treated as *nuisance parameters*, see later); and (3) parameters describing experimental effects, e.g. effect of calibration, of the particular survey, treated as nuisance parameters.

The equation (1.69) can be applied to the definitions of the CMB spectrum and bispectrum, in order to relate them to their primordial counterparts eq. (1.35a) and (1.35b). After some algebra (involving integrating angles between vectors \mathbf{k}_i 's, using properties of spherical harmonics, expanding the Dirac delta in Legendre polynomials...) we arrive at the expressions:

$$\langle a_{\ell_1 m_1} a_{\ell_2 m_2}^* \rangle = \delta_{\ell_1 \ell_2} \delta_{m_1 m_2} \frac{2}{\pi} \int_0^\infty dk k^2 \Delta_\ell^2(k) P_\zeta(k), \quad (1.70)$$

$$\begin{aligned} \langle a_{\ell_1 m_1} a_{\ell_2 m_2} a_{\ell_3 m_3} \rangle &= \mathcal{G}_{\ell_1 \ell_2 \ell_3}^{m_1 m_2 m_3} \left(\frac{2}{\pi} \right)^3 \iiint dk_1 dk_2 dk_3 (k_1 k_2 k_3)^2 \\ &\quad \Delta_{\ell_1}(k_1) \Delta_{\ell_2}(k_2) \Delta_{\ell_3}(k_3) B_\zeta(k_1, k_2, k_3) J_{\ell_1 \ell_2 \ell_3}(k_1, k_2, k_3), \end{aligned} \quad (1.71)$$

where

$$J_{\ell_1 \ell_2 \ell_3}(k_1, k_2, k_3) := \int x^2 dx j_{\ell_1}(k_1 x) j_{\ell_2}(k_2 x) j_{\ell_3}(k_3 x), \quad (1.72)$$

and the already mentioned *Gaunt integral* is

$$\mathcal{G}_{\ell_1 \ell_2 \ell_3}^{m_1 m_2 m_3} := \int d\Omega_{\hat{\mathbf{x}}} Y_{\ell_1 m_1}(\hat{\mathbf{x}}) Y_{\ell_2 m_2}(\hat{\mathbf{x}}) Y_{\ell_3 m_3}(\hat{\mathbf{x}}), \quad (1.73)$$

whose solution is eq. (1.60) and whose properties we have already discussed.

1.4.3 Experimental status

The CMB temperature power spectrum measured by the Planck satellite and released in March 2013 [5] can be seen in figure 1.5(a), with the best-fit Λ CDM model on top (solid line). As we can see, the concordance between the measured power spectrum and the Λ CDM prediction is stunning.

The CMB bispectrum found by Planck can be seen in figure 1.5(b). Its small size appears to fulfil the prediction for slow-roll inflation (see sec. 1.3.3), though there are hints of an oscillatory pattern with possible primordial origin [7, sec. 7.3.3].

1.5 Constraining inflation with the CMB – parameter extraction

Now that we have proven how the properties of the perturbations generated by inflation are imprinted in the CMB, we turn to the topic of how to extract that information from the measured CMB data of a real survey. The result is given as regions of the parameter space containing the most likely values of the cosmological parameters that generated the data at hand. To achieve that result, we will need a number of statistical tools, which we discuss in this section.

1.5.1 Bayes' theorem

Let \mathcal{M} be our model for the Universe, which depends on some parameters θ defined over a parameter space Θ . Let \mathcal{D} be a set of data that may be well described by the model \mathcal{M} . We are interested in the probability distribution of the parameters of the model $\mathcal{P}(\theta | \mathcal{D}, \mathcal{M})$, conditional on having observed the data \mathcal{D} , which we assume has been produced by the model \mathcal{M} . We call it *posterior pdf*⁸. It is often extracted from *Bayes' theorem*, which states

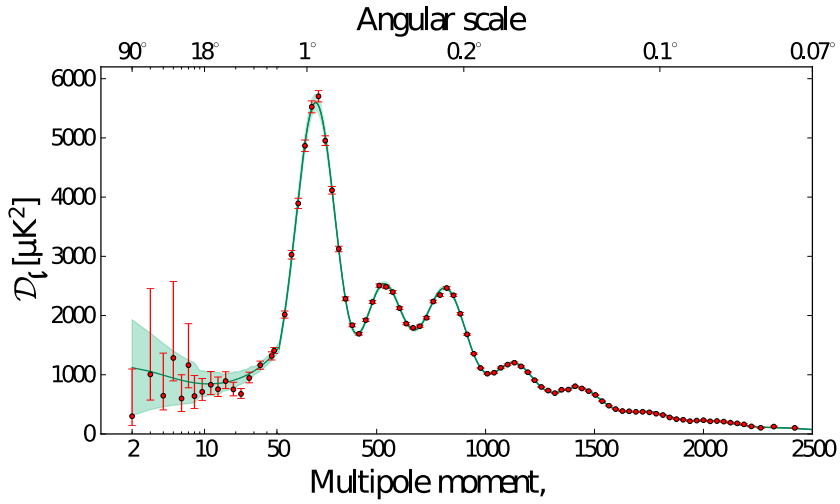
$$\mathcal{P}(\theta | \mathcal{D}, \mathcal{M}) = \frac{\mathcal{L}(\mathcal{D} | \mathcal{M}(\theta))}{\mathcal{Z}(\mathcal{D} | \mathcal{M})} \pi(\theta | \mathcal{M}) . \quad (1.74)$$

Here, we have introduced three more probability distributions:

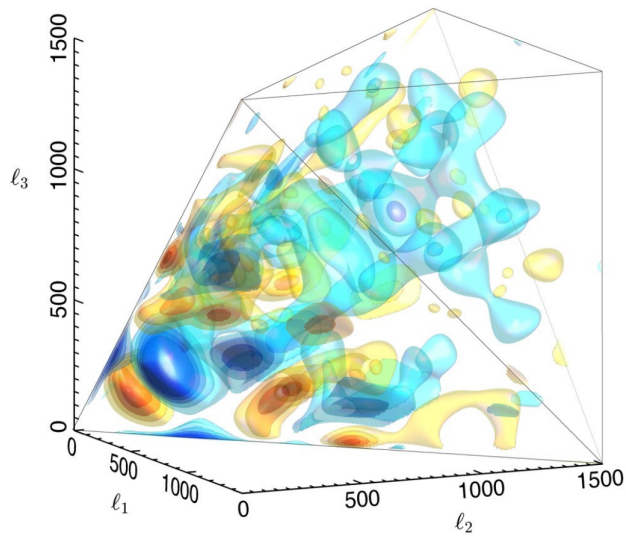
$\pi(\theta | \mathcal{M})$, , called **prior**, is the pdf of the values of the parameters θ within the model \mathcal{M} , which is assigned before knowing about the data \mathcal{D} .

$\mathcal{L}(\mathcal{D} | \mathcal{M}(\theta))$, called **likelihood**, is the pdf of all possible outcomes of the survey that produced the data \mathcal{D} , assuming that the hypothetical model \mathcal{M} is true, and the right values of its parameters are θ . It measures the compatibility of the data with the hypothesis.

⁸The *probability density function (pdf)* of a random variable x is a positive definite function $f(x)$ defined such that the probability of x being sampled in the (a, b) interval is equal to $\int_a^b f(x) dx$. The pdf must be normalised to 1 over the domain of x .



(a) Temperature power spectrum of Planck on March 2013, from [5]. D_ℓ stands for $\ell(\ell + 1)C_\ell/2\pi$, and the shaded area represents the cosmic variance. The solid line is the prediction of the best-fit Λ CDM model.



(b) Reconstructed bispectrum of Planck on March 2013, from [7] (in colour).

Figure 1.5: CMB power spectrum and bispectrum from Planck’s data release of March 2013.

$\mathcal{Z}(\mathcal{D}|\mathcal{M})$, called **marginal likelihood** or **evidence**, is the probability of all possible outcomes of the survey that produced the data \mathcal{D} , given that the model \mathcal{M} is true, and having marginalised (i.e. integrated) over every possible value of the parameters θ .

We will describe the prior and likelihood pdf's in the following sections, and ignore the evidence for now, since when dealing with parameter extraction it only amounts to an uninteresting normalisation constant. The result of the parameter extraction process will therefore be the region of the parameter space Θ over which the probability

$$\mathcal{P}(\theta|\mathcal{D}, \mathcal{M}) \propto \mathcal{L}(\mathcal{D}|\mathcal{M}(\theta)) \pi(\theta|\mathcal{M}) , \quad (1.75)$$

takes its highest values.

1.5.2 Prior

The prior pdf should encode two features:

Extension It should assign zero probability for those values of the theory which are considered not valid for the model, e.g. negative values of a mass.

Distribution Different approaches are possible, but one often tries to assign equal probability to values of the parameters among which there are no preferred ones, e.g. a uniform pdf in time for an instantaneous phenomenon whose timing we cannot predict. One can also choose a prior such that it lets the data, through the likelihood, be most informative when determining the constraints on the parameters (these priors are often called *non-informative*). For an extended review on different criteria for prior choice, see [26].

These aspects of the prior may present some problems:

Extension Some parameters, such as those controlling a perturbative expansion, have only *soft* limits, so their extension is not clear; e.g. the amplitude controlling a perturbative expansion may have as an upper limit 10^{-1} , 10^{-2} , 10^{-3} ...

Distribution We will try to assign equal probabilities to unpreferred values of the parameters, but what pdf this precisely means depends on the particular parametrisation of the model, since lack of preference for a parameter θ does not mean the same as lack of preference for θ^2 : a uniform pdf for θ transforms into a $\frac{1}{\theta}$ prior for θ^2 .

Despite the problems stated above, fortunately different choices of the prior make a very small difference for highly predictive data which impose strong restrictions on the parameters' values. In the pessimistic case of a not-so-restricted model, where the choice of the priors is important, care must be taken in clearly stating the choice of the prior and how it affects the result, by showing how the posterior varies for different prior choices.

1.5.3 Digression – Objectivity, frankness and Bayesian statistics

Some people see the existence of prior pdf's in Bayesian statistics as a flaw of the approach which would introduce *unnecessary subjectivity*, since the prior I am assigning may not be the same that someone else may assign. Let us argue that it is not *unnecessary*, and it is not more *subjective* than any other model assumption.

Necessity. Confidence intervals are regions of the parameter space built in such a way that the probability of the underlying true value of the parameters falling in those intervals, given the data, is equal to a certain value, usually 68% or 95%, which correspond respectively to the 1- and 2- σ intervals of a gaussian pdf. Confidence intervals are built from posterior samples (likelihood samples in the frequentist approach), such that they contain some fraction of the posterior mass (i.e. the integral of the posterior over those intervals amounts to that fraction of the total integral). It is easy to prove that the shape of those confidence intervals unavoidably depends on the choice of parametrisation of the model. The frequentist approach uses the Fischer information matrix to account for that dependence. The Bayesian approach does it in a different way: different parametrisations are equivalent to different prior choices. Therefore, in the introduction of prior pdf's is necessary in order to account for an effect that is already explicitly present in the frequentist approach.

Subjectivity. Objectivity in science is about the methods applied to reach the results, and about putting up-front every assumption of the model under test. The assumptions themselves, though they must be sane from a scientific point of view, are chosen subjectively, up to the physical intuition of the scientist, and may change under certain circumstances. Again, it is being straightforward about those assumptions which gives the scientific endeavour its objectivity. This is precisely what Bayesian statistics does: discussing a prior choice is not a trick to get the results that one desires; it is being frank about an *unavoidable* choice of assumptions.

1.5.4 Likelihood

As we stated, the likelihood function $\mathcal{L}(\mathcal{D}|\mathcal{M}(\theta))$ is the probability that the data \mathcal{D} is an actual realisation of the model \mathcal{M} . In our particular case, the data is the CMB power spectrum as measured from the map, while our model \mathcal{M} is our calculation of it starting from the primordial perturbations described in section 1.3 and projecting them in the CMB sky following section 1.4. Of course, \mathcal{M} may also be any modification of the Λ CDM model, like the one we test in chapters 2 and 3 of this thesis.

When comparing them both, one has to take into account the spurious effects that introduce differences between the power spectrum that we measure in the CMB and the one our model predicts. Those effects may be intrinsic to the instrument, such as the effect of the *beam window function* of the detector (real-world detectors, when pointed to one direction, give back not exactly the signal coming from that precise direction, but an integrated measurement that includes some signal coming from the surroundings of the direction to which we point), instrumental noise (some of the signal is generated by electronic noise in the detectors) or differences in calibration between different instruments of the survey; they may also be *foregrounds*, i.e. the physical effects that disturb the CMB photons during their journey towards us.

A likelihood function must take into account those effects and model them as effectively as possible. The likelihood function then takes the more exact form

$$\mathcal{L}(C_\ell^{\text{map}} | C_\ell^{\mathcal{M}}(\theta), \mathcal{M}^*(\eta)) , \quad (1.76)$$

where $C_\ell^{\mathcal{M}}(\theta)$ is the CMB power spectrum predicted by our model and parametrised by θ , and \mathcal{M}^* models the aforementioned instrumental and foreground effects, parametrised by η .

For didactic purposes, let us formulate a very basic likelihood function for a very basic, fictional CMB survey. For starters, we will ignore foreground effects on top of the CMB signal, assume full-sky coverage on a single frequency, and correct only for the effects of the beam of the detector and its electronic noise, and the fact that CMB maps have finite pixelisation.

The simplest *data model* hypothesis that we can make is

$$\mathbf{d} := \mathbf{s} + \mathbf{n} , \quad (1.77)$$

where the components d_i of the vector \mathbf{d} are the measured values of the temperature anisotropy $\Delta T/T$ corresponding to the pixel i of the map, with a total number of pixels N_{pix} ; we have divided this data into a linear combination of two components: the underlying CMB signal \mathbf{s} and the amount of signal given by the noise, \mathbf{n} . According to our cosmological model, the temperature anisotropies caused by inflation are gaussian. Their covariance, $\langle \Delta T_i/T \cdot \Delta T_j/T \rangle$, is, according to eq. (1.58)

$$\langle s_i s_j \rangle = \sum_\ell \frac{2\ell + 1}{4\pi} \hat{C}_\ell P_\ell(\alpha_{i,j}) , \quad (1.78)$$

where $\alpha_{i,j}$ is the angle between the centres of the pixels i and j . The power spectrum on the right hand side is directly calculated from the pixelised map. In order to extract the power spectrum corresponding to the underlying CMB signal, one has to take into account the effects of the finite beam of the experiment and that of the pixelisation.

In any detector the signal measured in a direction $\hat{\mathbf{n}}$ does not just come from it only, but also mixes in some signal from adjacent directions. This means that in our map the temperature fluctuation measured as coming from $\hat{\mathbf{n}}$ is the result of the convolution with a *beam window function* B :

$$\left(\frac{\widehat{\Delta T}}{T}\right)(\hat{\mathbf{n}}) = \int_{\Omega_{\hat{\mathbf{r}}}} \left(\frac{\Delta T}{T}\right)^{\text{CMB}}(\hat{\mathbf{r}}) B(\cos(\hat{\mathbf{r}}, \hat{\mathbf{n}})) \, \text{d}\Omega_{\hat{\mathbf{r}}}, \quad (1.79)$$

where we integrate over all possible directions $\hat{\mathbf{r}}$. If we make now a spherical transform, we get

$$\hat{a}_{\ell m} = \int_{\Omega_{\hat{\mathbf{n}}}} \left\{ \int_{\Omega_{\hat{\mathbf{r}}}} \left(\frac{\Delta T}{T}\right)^{\text{CMB}}(\hat{\mathbf{r}}) B(\cos(\hat{\mathbf{r}}, \hat{\mathbf{n}})) \, \text{d}\Omega_{\hat{\mathbf{r}}} \right\} Y_{\ell m}^*(\hat{\mathbf{n}}) \, \text{d}\Omega_{\hat{\mathbf{n}}} = a_{\ell m}^{\text{CMB}} B_{\ell}. \quad (1.80)$$

Notice how the spherical harmonics transformation turns the convolution with the beam window function into a product with the transformed beam window function B_{ℓ} . A typical shape for a beam is a gaussian one with variance σ_B^2 , whose spherical harmonic transform is $B_{\ell} = \exp(-1/2 \ell(\ell+1)\sigma_B^2)$.

After applying this and a similar correction for the pixel window function (each pixel integrates signal from a finite area) encoded by W_{ℓ} [24], we get the variance of the signal as a function of the underlying CMB spectrum

$$\langle s_i s_j \rangle = \sum_{\ell} \frac{2\ell+1}{4\pi} C_{\ell}^{\text{CMB}} B_{\ell}^2 W_{\ell}^2 P_{\ell}(\alpha_{i,j}), \quad (1.81)$$

We know the probability distribution for the signal part of the data: it follows a gaussian distribution with zero mean and the variance above. As for the electronic noise, we often assume it to be gaussian, with a variance $N_{i,j}$ (and zero mean). The sum of two gaussians is a gaussian, whose mean and variance are the sum of those of the components. Therefore, the pdf of the data in all pixels is the multivariate gaussian

$$\mathbf{d} \sim \mathcal{N}(0, \boldsymbol{\Sigma}), \quad (\boldsymbol{\Sigma})_{i,j} := \sum_{\ell} \frac{2\ell+1}{4\pi} C_{\ell}^{\text{CMB}} B_{\ell}^2 W_{\ell}^2 P_{\ell}(\alpha_{i,j}) + N_{i,j}. \quad (1.82)$$

This probability distribution is, of course, conditional on the underlying model \mathcal{M} giving the CMB power spectrum, parametrised by some variables θ , and on the models for the beam and the noise, that we will ignore in the future. Therefore, as this multivariate gaussian assigns a probability for the particular realisation of the data given an underlying model, we have precisely the *likelihood* we wanted:

$$\mathcal{L}(\mathbf{d} | \mathcal{M}(\theta)) = \frac{1}{(2\pi)^{N_{\text{pix}/2}} |\boldsymbol{\Sigma}|^{1/2}} e^{-\frac{1}{2} \mathbf{d} \boldsymbol{\Sigma}^{-1} \mathbf{d}}, \quad (1.83)$$

where the dependence on the model enters through the covariance matrix $\Sigma(\mathcal{M}(\theta))$.

The approach described above is a nice, simple one, but it is also doomed: inverting the matrix takes $\mathcal{O}(N_{\text{pix}}^3)$ operation: two orders come from the dimensions of the matrix, and the third one from the sum on ℓ , since the larger the resolution of the experiment is, ℓ_{max} , the finer the pixelisation needed. This approach makes sense only for low-resolution maps aimed at characterising the spectrum at low multipoles, $\ell \lesssim 50$, and even in that case the joint analysis of maps with multiple frequencies makes it computationally expensive, since we have to multiply N_{pix} by the number of maps. In addition to that, we still need to account for the effect of foregrounds, which introduce further computational complications. Still, the method described here can be used as a basis for the temperature power spectrum likelihoods of Planck are formulated [5], in particular for $\ell < 50$. For higher multipoles, the *central limit theorem* can be exploited to gain some simplicity.

The low- ℓ Planck C_ℓ likelihood

The low- ℓ likelihood is based on a more sophisticated version of the method described above. It is known as *Commander*, and it is presented in [18]. Let us sketch it here. As a first step, we include different foregrounds effects as components of the total temperature perturbation:

$$\mathbf{d} := \mathbf{s} + \mathbf{n} + \sum_i \mathbf{f}^{(i)}. \quad (1.84)$$

As for the CMB signal, we need a model for the foreground effects, \mathcal{M}^* with parameters η . As this method is to be applied to small multipoles only, the resolution of the sky maps is downgraded to gain some efficiency.

Let us now look at the joint pdf of the CMB signal \mathbf{s} , its underlying estimated power spectrum $\hat{C}_\ell^{\text{CMB}}$ (notice the difference with C_ℓ^{CMB} , given by the model \mathcal{M}), and the foreground effects $\mathbf{f}^{(i)}$, conditional to the measured temperature anisotropy \mathbf{d} , i.e. $\mathcal{P}(\mathbf{s}, \hat{C}_\ell^{\text{CMB}}, \mathbf{f}^{(i)} | \mathbf{d}, \mathcal{M}, \mathcal{M}^*)$. Marginalising over all possible splittings between CMB signal part and foreground effects, we would get the desired likelihood $\mathcal{P}(\hat{C}_\ell^{\text{CMB}} | \mathcal{M})$. But that is a very complicated distribution with lots of parameters coming both from the model for the CMB and the model for the foregrounds, and not even using a Monte Carlo method, as the one described in the next section, is this pdf easy to map out.

On the contrary, its conditional distributions for each of \mathbf{s} , $\hat{C}_\ell^{\text{CMB}}$ or $\mathbf{f}^{(i)}$ are much simpler: the first one,

$$\mathcal{P}(\mathbf{s} | \hat{C}_\ell^{\text{CMB}}, \mathbf{f}^{(i)}, \mathbf{d}, \mathcal{M}, \mathcal{M}^*) \equiv \mathcal{P}(\mathbf{s} | \mathbf{f}^{(i)}, \mathbf{d}, \mathcal{M}), \quad (1.85)$$

is, as we discussed, exactly a Gaussian distribution with covariance (1.81). The

second,

$$\mathcal{P}\left(\hat{C}_\ell^{\text{CMB}} \mid \mathbf{s}, \mathbf{f}^{(i)}, \mathbf{d}, \mathcal{M}, \mathcal{M}^*\right) \equiv \mathcal{P}\left(\hat{C}_\ell^{\text{CMB}} \mid \mathbf{s}\right), \quad (1.86)$$

can be easily calculated to be an *inverse gamma distribution*.⁹ The last one,

$$\mathcal{P}\left(\mathbf{f}^{(i)} \mid \mathbf{s}, \hat{C}_\ell^{\text{CMB}}, \mathbf{d}, \mathcal{M}, \mathcal{M}^*\right) \equiv \mathcal{P}\left(\mathbf{f}^{(i)} \mid \mathbf{s}, \mathbf{d}, \mathcal{M}^*\right), \quad (1.87)$$

has no simple analytical form, but can be mapped out numerically without much difficulty. When the single conditional distributions are simple enough, we can take a Monte Carlo approach known as *Gibbs sampling*, consisting on applying a Markov Chain algorithm on each of the distributions alternatively (the reader may want to come back to this section once having read the next one): at a step t of the chain, first sample a point \mathbf{s}_{t+1} from (1.85), then use the combination $(\mathbf{s}_{t+1}, \hat{C}_{\ell,t}^{\text{CMB}}, \mathbf{f}_t^{(i)})$ as a starting point to sample a point $\hat{C}_{\ell,t+1}^{\text{CMB}}$ from (1.86), and lastly, using $(\mathbf{s}_{t+1}, \hat{C}_{\ell,t+1}^{\text{CMB}}, \mathbf{f}_t^{(i)})$ sample a point $\mathbf{f}_t^{(i)}$ from (1.87), getting the following step of the chain, $(\mathbf{s}_{t+1}, \hat{C}_{\ell,t+1}^{\text{CMB}}, \mathbf{f}_{t+1}^{(i)})$; repeat until achieving convergence. Once we have enough samples, we can marginalise over \mathbf{s} and the foregrounds and use the result to create an approximated interpolating likelihood $\mathcal{L}\left(\hat{C}_\ell^{\text{CMB}} \mid \mathcal{M}\right)$.

The high- ℓ Planck C_ℓ likelihood

For higher multipoles, we need higher resolution maps, which makes the method above less efficient. Planck used the *CamSpec* algorithm [5, sec. 2.1], based on the *MASTER* approach [25].

Let $\tilde{a}_{\ell m}$ be the spherical transform in the pixelised map of the data \mathbf{d} , including the correction of a beam window function as in eq. (1.80). We can estimate from them a power spectrum, that we call *pseudo- C_ℓ* , as

$$\tilde{C}_\ell = \frac{1}{2\ell + 1} \sum_m |\tilde{a}_{\ell m}|^2. \quad (1.88)$$

This power spectrum contains contributions from the CMB and foregrounds, and a contribution from the instrumental noise that can be minimised if we use $\tilde{a}_{\ell m}$ of different maps to calculate this square (the instrumental noise is uncorrelated in the different instruments; though a small contribution is left, it is guaranteed to be unbiased, i.e. to have zero mean). It can be proven [25] that the underlying joint power spectrum of CMB and foregrounds, \hat{C}_ℓ , can be recovered from the pseudo- C_ℓ multiplying by a convolution matrix $M_{\ell\ell'}$ that accounts for the leaking between multipoles due to the finite beam window function, the pixelisation of the map and the use of non-full sky coverage (a big chunk of the sky, containing the galactic plane up to a elevation and a number of point sources, is discarded

⁹See e.g. http://en.wikipedia.org/wiki/Inverse-gamma_distribution.

to minimise the effect of the anisotropic part of the foregrounds). Since the convolution matrix can be calculated explicitly (see [5, app. A.1]), we can work directly with the pseudo- C_ℓ .

Working with the \tilde{C}_ℓ has an important advantage. Given isotropy of the signal,¹⁰ for equal ℓ all the $\tilde{a}_{\ell m}$ are distributed following the same pdf, with a well-defined mean and variance. On the other hand, according to eq. (1.88), \tilde{C}_ℓ is at each ℓ equal to the average of the $\tilde{a}_{\ell m}$ over m . For high values of ℓ (remember, here $\ell > 50$), up to a very good approximation the *central limit theorem* is fulfilled:¹¹ the pseudo- C_ℓ follow a simple gaussian distribution. Therefore, the likelihood can simply be written as a multivariate gaussian – the product of a gaussian for each ℓ . The covariance matrix Σ of the multivariate gaussian, giving the dependence between the different multipoles (and between different combinations of frequencies) is estimated from simulations performed on a fiducial model. Having precomputed it, the value of the gaussian likelihood can be computed in a very small amount of time.

As in the low- ℓ case, the likelihood is conditional on the models for the CMB power spectrum and the isotropic foreground effects, as well here as on the different calibration parameters for the maps used. Marginalising at the time of sampling over these *nuisance* effects one can get the desired likelihood $\mathcal{L}(\hat{C}_\ell^{\text{CMB}} | \mathcal{M})$.

1.5.5 Monte Carlo methods

Now that we have all the necessary ingredients to extract the posterior pdf of the parameters of the model and characterise it around its maximum, we may try to do so in the most naïve way: analytically maximising the product of prior and likelihood using a gradient method, i.e. following the direction of the function with the highest slope until we find its maximum. We will immediately find this approach to be practically unfeasible, due to problems such as

Non-analyticity of the likelihood: In the particular case of the CMB, the calculation of the CMB power spectrum from the primordial conditions, based on eq. (1.69), cannot be done analytically, but is the result of numerical solutions of a system of Boltzmann equations, often solved with the help of computers [30, 11].

Cost of calculating the likelihood: In the particular case of the CMB, the full calculation of the likelihood from the set of parameters of the model may take up to a few seconds. This discourages us from attempting a thorough sampling on a grid in the parameter space, aimed at constructing an analytic approximation to the likelihood as an interpolating function.

¹⁰The most anisotropic foregrounds, Via Lactea and point sources, have been masked away. The remaining ones are isotropic to a good approximation.

¹¹See e.g. http://en.wikipedia.org/wiki/Central_limit_theorem.

Size of the parameter space: The dimensionality of the typical parameter spaces, including interesting parameters of the model and uninteresting parameters modelling the survey’s shortcomings, easily goes to high values. This too prevents us from searching an interpolating approximation of the likelihood by sampling on a grid.

Complicated shape of the likelihood: Even in the optimistic case of an analytic likelihood, it is usually a very complicated function with many local maxima, in which a gradient method may get trapped.

These problems tell us about the desired features of an ideal solution: it needs a mechanism for not getting trapped in local maxima, often realised through some random jumping; it must sample as few points of the parameter space as possible, and it must scale well with the dimensionality of the parameter space.

The result of this method must be a *fair sample*, or set of pairs of points in the parameter space and their respective values of the likelihood, possibly including a relative *sampling weight*. *Fairness* of the sample means that in every region, the density of the sampling must be proportional to the probability density. If the goal is to obtain constraints for the parameters of the model, the samples only need to cover the region of the parameter space where the posterior has most of its probability mass.

We call *Monte Carlo methods* a broad family of random sampling algorithms aimed at solving this kind of problems.

1.5.6 Markov chain Monte Carlo

In this section we will start by briefly defining the general concept of a Markov chain, its expected properties, and the Metropolis-Hastings algorithm. Details and proofs can be found in [23, Ch. 1 & 4]

Let X_0, X_1, \dots, X_t be a sequence of random variables taking values on a *state space* E . A (discrete time) *Markov chain* is a sequence of such random variables X_0, X_1, \dots, X_t such that the probability of the random variable to take values in a particular subset $A \subset E$ in the next step depends *only* on the value taken in the current step:

$$\mathcal{P}(X_{t+1} \in A | X_0 = x_0, X_1 = x_1, \dots, X_t = x_t) = \mathcal{P}(X_{t+1} \in A | X_t = x_t) . \quad (1.89)$$

A Markov chain is *time-homogeneous* or *stationary* whenever this probability does not depend on the specific order of the step for which the last property is fulfilled:

$$\mathcal{P}(X_{t+1} \in A | X_t = x) = \mathcal{P}(X_t \in A | X_{t-1} = x) \quad \forall t , \quad (1.90)$$

i.e. $\mathcal{P}(X_{t+1} \in A | X_t = x)$ is independent of the order of the step, and we call it the *transition kernel*. The probability distribution of any step of a stationary

Markov chain is completely specified by its transition kernel and the probability distribution of the initial step.

A stationary Markov chain has *stationary* or *invariant distribution* ρ when, being ρ the initial probability distribution at step t ,

$$\mathcal{P}(X_{t+1} \in A | X_t \sim \rho) = \rho(A) \quad \forall t. \quad (1.91)$$

Thus, *the kernel of a stationary Markov chain is determined by its stationary distribution.*

As it should be obvious by now, we will try to build a Markov chain such that the stationary distribution is the pdf that we wish to sample, in this case the *posterior pdf* $\mathcal{P}(\theta | \mathcal{D}, \mathcal{M})$.

At this point, looking at eq. (1.91), it appears that the points in the chains are drawn from the stationary pdf ρ . One would be tempted to estimate the desired averages over ρ , $\langle f(X) \rangle_\rho$, using averages over the states along the chain, i.e. *ergodic* averages:

$$\bar{f}_n := \frac{1}{n+1} \sum_{i=0}^n f(X_i), \quad (1.92)$$

but there are two important caveats:

1. For the states of the chain to really be samples from ρ , according to eq. (1.91) all the previous states must be so, *including the initial state* X_0 , which obviously cannot be sampled from ρ yet, since sampling from ρ is precisely the problem at hand. Therefore, we need to ensure that the initial state will be *forgotten* at some point, leaving us with pure samples from ρ . We achieve so by discarding a number of initial states of the chain when calculating (1.92), which we call *burn-in states*.
2. Still, the samples are not *independent* from one another, but correlated samples from ρ . This needs not be a problem, provided that the samples are drawn in the correct proportion, i.e. drawing from $A \subset E$ must be proportional to $\rho(A)$, i.e. the sample, though correlated, must be *fair*.

Ensuring this two requirements, or having *convergence* of the path-average \bar{f}_n to the true expected value under the stationary pdf $\langle f \rangle_\rho$, is defined as the Markov chain being *ergodic*. In order to ensure ergodicity, one must prove three properties of the chain: that it is *irreducible*, i.e. it explores all subsets $A \subset E$ such that $\rho(A) \neq 0$, *recurrent*, i.e. an infinite chain reaches said regions infinitely often, and *aperiodic*, i.e. it does not transition cyclically through a fixed sequence of sets.

We now propose a very simple algorithm to build a Markov chain that is stationary and convergent, and which is the basis, with some improvements, of most of the widespread cosmological MCMC codes [29, 9]. It is called the *Metropolis-Hastings algorithm*.

Suppose a *proposal* pdf $\phi(Y|X_t)$, where X_t is the value at the current step. For example, $\phi(Y|X_t) \sim \mathcal{N}(X_t, \mathcal{C})$, a multivariate gaussian centred at X_t and with a fixed covariance matrix \mathcal{C} . Let us suppose the we draw a sample y from ϕ . Assuming ρ to be the stationary pdf of the chain, we build the quantity

$$\alpha(X_t, Y) := \min \left(1, \frac{\rho(Y) \phi(X_t | Y)}{\rho(X) \phi(Y | X_t)} \right). \quad (1.93)$$

Notice that $\alpha \in [0, 1]$. The new point Y is accepted or rejected as the next point of the chain with probability α . If it is rejected, take $X_{t+1} = X_t$. In any case, repeat for X_{t+2} . Notice how in eq. (1.93) the ratio of the stationary distribution drives the next step towards the maxima of this pdf. Notice too how the choice of a gaussian proposal distribution implies that the second fraction has no effect.

The proposal distribution ϕ and the stationary distribution of the chain ρ is all we need to build the Metropolis-Hasting Markov chain. It is easy to see that its kernel is

$$\mathcal{P}(X_{t+1} | X_t) = \phi(X_{t+1} | X_t) \alpha(X_t, X_{t+1}) + I(X_{t+1} = X_t) \left[1 - \int \phi(Y | X_t) \alpha(X_t, Y) dY \right], \quad (1.94)$$

where $I(\text{cond})$ is a function valued 1 if *cond* is true and 0 otherwise.

It can be proven that this chain converges towards the stationary distribution ρ regardless of the choice of the proposal distribution ϕ . This does not mean that this is not an important choice: the convergence will be faster the closest the proposal distribution is to the stationary distribution – a bad choice of ϕ will have bad consequences in the efficiency of the sampling of ρ : if ϕ is much more concentrated than ρ , we will not reach to explore the tails of the distribution ρ ; if ϕ is very spread, we will tend to draw candidate samples Y such that $\rho(Y) \ll \rho(X_y)$, away from the maxima, so we will very often reject them, resulting in a chain with many repeated steps and few different ones. Therefore, assuming a nearly-gaussian stationary pdf, one would ideally try to use a gaussian proposal pdf with a covariance matrix as close as possible to that of the stationary distribution.¹² In order to get such a covariance matrix, we can approximate it from the sample covariance of a small chain of sample of ρ .

1.5.7 Final remarks

Having described the likelihood and prior pdf's, and one of the Monte Carlo methods aimed at mapping the posterior, the next step is to actually use these tools to tackle the two most common computational tasks in statistical inference: *parameter inference* and *model selection* (in frequentist terms, equivalent to *hypothesis*

¹²In fact, it is advisable to use a covariance matrix for the proposal distribution that is a little broader than that of the stationary distribution, since the tails of the latter get better sampled this way.

testing). We will not go into much detail here, but just introduce how these two problems have been approached in the research performed for this thesis.

Parameter inference

Parameter inference is the problem of, given a model with some parameters, characterising the regions of the parameter space containing most of the posterior probability, i.e. containing the most likely underlying parameter values. These regions are called *confidence level regions* or *intervals*. Computing them requires a sampling method that produces *fair samples*, since we will estimate the probability corresponding to those regions with the proportion of the Monte Carlo samples falling inside them. Since confidence level intervals are, of course, centred around the maxima of the posterior, the sampling method used must guarantee that the regions of higher posterior value are thoroughly explored, as Markov chain Monte Carlo does.

If the resulting posterior is at least approximately gaussian, a set of nested confidence level intervals (usually 68% and 95%) summarises the posterior pdf well enough. In the opposite case, of very non-gaussian distribution with several regions of high probability, not only confidence intervals are not enough to summarise the information contained in the posterior, but also the simple Markov chain approach explained in the last section needs a unmanageably large amount of running time in order to guarantee that the sampling is fair. This is so because the chain gets *stuck* around one of the several maxima (or *modes*), and only rarely jumps between all of them, and only after a large number of *exchanges* between the modes can their relative mass probabilities be fairly represented.

The case of a non-gaussian distribution with several modes is prone to pop out whenever we attempt to constrain parameters of models which exploit small anomalies close to the signal-to-noise ratio of the data set; this is what we do in this study with CMB and LSS data. In these cases, one often prefers alternative methods to Markov chain Monte Carlo, specially aimed at mapping weirdly-shaped pdf's, such as *multi-modal nested sampling* [38, 21, 22, 20]. In the first part of this study, however, we managed to map a multi-modal posterior using solely MCMC's. The method we used is described in section 2.3.

Model selection

Model selection is the problem of assessing which one of a set of models is the most likely to have generated the data at hand, or equivalently which one is the most informative or predictive. The quantification of this predictivity is given by the *evidence*, defined in section 1.5.1, which is the marginalisation of the data likelihood over the priors allowed by the theory, i.e. the total probability of the model being the underlying one regardless of the values of its parameters. A short review of the procedure followed in *Bayesian model selection* can be found in section 3.3.

In particular, in this study we do not aim to characterise the total evidence of the model discussed in section 1.3.4, since we do not explore the full parameter region allowed by the model, but instead explore a significant patch of it and use model selection arguments to argue about the consistency between candidate signals in CMB and LSS data. The reader is referred to chapter 3 for the complete discussion. The sampling method used in this part of the study is the aforementioned multi-modal nested sampling, which is briefly described in section 4.3.

Bibliography

- [1] L. F. Abbott and M. B. Wise. Large-scale anisotropy of the microwave background and the amplitude of energy density fluctuations in the early universe. *Astrophys.J.Lett.*, 282:L47–L50, July 1984.
- [2] Ana Achucarro, Jinn-Ouk Gong, Sjoerd Hardeman, Gonzalo A. Palma, and Subodh P. Patil. Effective theories of single field inflation when heavy fields matter. *JHEP*, 1205:066, 2012, 1201.6342.
- [3] Ana Achucarro, Jinn-Ouk Gong, Gonzalo A. Palma, and Subodh P. Patil. Correlating features in the primordial spectra. *Phys.Rev.*, D87:121301, 2013, 1211.5619.
- [4] Viviana Acquaviva, Nicola Bartolo, Sabino Matarrese, and Antonio Riotto. Second order cosmological perturbations from inflation. *Nucl.Phys.*, B667:119–148, 2003, astro-ph/0209156.
- [5] P.A.R. Ade et al. Planck 2013 results. XV. CMB power spectra and likelihood. 2013, 1303.5075.
- [6] P.A.R. Ade et al. Planck 2013 results. XXII. Constraints on inflation. 2013, 1303.5082.
- [7] P.A.R. Ade et al. Planck 2013 Results. XXIV. Constraints on primordial non-Gaussianity. 2013, 1303.5084.
- [8] P.A.R. Ade et al. Planck 2013 results. XVI. Cosmological parameters. *Astron.Astrophys.*, 2014, 1303.5076.
- [9] Benjamin Audren, Julien Lesgourgues, Karim Benabed, and Simon Prunet. Conservative Constraints on Early Cosmology: an illustration of the Monte Python cosmological parameter inference code. *JCAP*, 1302:001, 2013, 1210.7183.
- [10] Daniel Baumann. TASI Lectures on Inflation. 2009, 0907.5424.

-
- [11] Diego Blas, Julien Lesgourgues, and Thomas Tram. The Cosmic Linear Anisotropy Solving System (CLASS) II: Approximation schemes. *JCAP*, 1107:034, 2011, 1104.2933.
- [12] T.S. Bunch and P.C.W. Davies. Quantum Field Theory in de Sitter Space: Renormalization by Point Splitting. *Proc.Roy.Soc.Lond.*, A360:117–134, 1978.
- [13] Clifford Cheung, Paolo Creminelli, A. Liam Fitzpatrick, Jared Kaplan, and Leonardo Senatore. The Effective Field Theory of Inflation. *JHEP*, 0803:014, 2008, 0709.0293.
- [14] Paolo Creminelli and Matias Zaldarriaga. Single field consistency relation for the 3-point function. *JCAP*, 0410:006, 2004, astro-ph/0407059.
- [15] Tamara M. Davis and Charles H. Lineweaver. Superluminal recession velocities. 2000, astro-ph/0011070.
- [16] Tamara M. Davis and Charles H. Lineweaver. Expanding confusion: common misconceptions of cosmological horizons and the superluminal expansion of the universe. *Proc.Astron.Soc.Austral.*, 2003, astro-ph/0310808.
- [17] S. Dodelson. *Modern Cosmology*. 2003.
- [18] H. K. Eriksen, J. B. Jewell, C. Dickinson, A. J. Banday, K. M. Górski, and C. R. Lawrence. Joint bayesian component separation and cmb power spectrum estimation. *The Astrophysical Journal*, 676(1):10, 2008.
- [19] J.R. Fergusson, M. Liguori, and E.P.S. Shellard. The CMB Bispectrum. *JCAP*, 1212:032, 2012, 1006.1642.
- [20] F. Feroz, M. P. Hobson, E. Cameron, and A. N. Pettitt. Importance Nested Sampling and the MultiNest Algorithm. *ArXiv e-prints*, June 2013, 1306.2144.
- [21] F. Feroz, M.P. Hobson, and M. Bridges. MultiNest: an efficient and robust Bayesian inference tool for cosmology and particle physics. *Mon.Not.Roy.Astron.Soc.*, 398:1601–1614, 2009, 0809.3437.
- [22] Farhan Feroz and M.P. Hobson. Multimodal nested sampling: an efficient and robust alternative to MCMC methods for astronomical data analysis. *Mon.Not.Roy.Astron.Soc.*, 384:449, 2008, 0704.3704.
- [23] W. R. Gilks, S. Richardson, and D. J. Spiegelhalter. *Markov Chain Monte Carlo In Practice*. Chapman and Hall/CRC, 1999.
- [24] K.M. Gorski, Eric Hivon, A.J. Banday, B.D. Wandelt, F.K. Hansen, et al. HEALPix - A Framework for high resolution discretization, and fast analysis of data distributed on the sphere. *Astrophys.J.*, 622:759–771, 2005, astro-ph/0409513.

- [25] E. Hivon, K.M. Gorski, C.B. Netterfield, B.P. Crill, S. Prunet, et al. Master of the cosmic microwave background anisotropy power spectrum: a fast method for statistical analysis of large and complex cosmic microwave background data sets. *Astrophys.J.*, 567:2, 2002, astro-ph/0105302.
- [26] Robert E. Kass and Larry Wasserman. The selection of prior distributions by formal rules. *Journal of the American Statistical Association*, 91(435):1343–1370, 1996.
- [27] L.V. Keldysh. Diagram technique for nonequilibrium processes. *Zh.Eksp.Teor.Fiz.*, 47:1515–1527, 1964.
- [28] Thomas S. Kuhn. *The structure of scientific revolutions*. University of Chicago Press, Chicago, 1970.
- [29] Antony Lewis and Sarah Bridle. Cosmological parameters from CMB and other data: a Monte- Carlo approach. *Phys. Rev.*, D66:103511, 2002, astro-ph/0205436.
- [30] Antony Lewis, Anthony Challinor, and Anthony Lasenby. Efficient computation of CMB anisotropies in closed FRW models. *Astrophys.J.*, 538:473–476, 2000, astro-ph/9911177.
- [31] M. Liguori, E. Sefusatti, J. R. Fergusson, and E. P. S. Shellard. Primordial Non-Gaussianity and Bispectrum Measurements in the Cosmic Microwave Background and Large-Scale Structure. *Advances in Astronomy*, 2010, 2010, 1001.4707.
- [32] Juan Martin Maldacena. Non-Gaussian features of primordial fluctuations in single field inflationary models. *JHEP*, 0305:013, 2003, astro-ph/0210603.
- [33] V. F. Mukhanov. Gravitational instability of the universe filled with a scalar field. *ZhETF Pisma Redaktsiiu*, 41:402–405, May 1985.
- [34] S. Perlmutter et al. Measurements of Omega and Lambda from 42 high redshift supernovae. *Astrophys.J.*, 517:565–586, 1999, astro-ph/9812133.
- [35] Adam G. Riess et al. Observational evidence from supernovae for an accelerating universe and a cosmological constant. *Astron.J.*, 116:1009–1038, 1998, astro-ph/9805201.
- [36] Matts Roos and S.M. Harun-or Rashid. How flat is the universe? 2000, astro-ph/0003040.
- [37] Misao Sasaki. Large Scale Quantum Fluctuations in the Inflationary Universe. *Prog.Theor.Phys.*, 76:1036, 1986.
- [38] John Skilling. Nested sampling. *AIP Conference Proceedings*, 735(1):395–405, 2004.

- [39] David Wands, Karim A. Malik, David H. Lyth, and Andrew R. Liddle. A New approach to the evolution of cosmological perturbations on large scales. *Phys.Rev.*, D62:043527, 2000, astro-ph/0003278.
- [40] Steven Weinberg. Adiabatic modes in cosmology. *Phys.Rev.*, D67:123504, 2003, astro-ph/0302326.
- [41] Steven Weinberg. Quantum contributions to cosmological correlations. *Phys.Rev.*, D72:043514, 2005, hep-th/0506236.

Chapter 2

Localized correlated features in the CMB power spectrum and primordial bispectrum from a transient reduction in the speed of sound

Foreword

This chapter is based on the published papers

Localized correlated features in the CMB power spectrum and primordial bispectrum from a transient reduction in the speed of sound

Ana Achúcarro, Vicente Atal, Pablo Ortiz, and Jesús Torrado

Published in Physical Review D89 (2014) 103006

Preprint in arXiv:1311.2552 [astro-ph.CO]

and

Inflation with moderately sharp features in the speed of sound: GSR and in-in formalism for power spectrum and bispectrum

Ana Achúcarro, Vicente Atal, Bin Hu, Pablo Ortiz, and Jesús Torrado

Published in Physical Review D90 (2014) 023511

Preprint in arXiv:1404.7522 [astro-ph.CO]

The results presented in them and reproduced here are the product of the combined effort of all its authors, who, as is customary in Theoretical Cosmology,

appear in alphabetical order.

As part of this Ph.D. thesis, I reproduce a major part both of the original publications, focusing on the parts in which my contribution was most significant, specially the sections concerning the parameter estimation and the interpretation of the results.

Abstract

We perform a search for localized oscillatory features in the Planck CMB power spectrum of the first year of observations, assuming that said features are caused by a transient reduction in the speed of sound of the adiabatic mode during effectively single-field, uninterrupted slow-roll inflation.

We find several fits, in which we perform several consistency checks and further analyses, such as its reproduction by the a different Boltzmann code, the study of their polarization signal in the CMB and their local significance at different angular scales.

For each of the best fits, we calculate the expected correlated signal in the primordial bispectrum, and compare it to the search for scale dependent bispectrum features carried out by the Planck collaboration. Where both searches overlap, we reproduce the Planck results reasonably well. In addition, some of our best fits lie outside the scales and frequency ranges searched by Planck, which calls for an extension in frequencies and envelopes of the templates used in Planck's search.

By exploiting correlations between different observables, our results strongly suggest that current and data, including the imminent 2014 Data Release of Planck, might already be sensitive enough to detect transient reductions in the speed of sound as mild as a few percent, opening a new window for the presence of extra degrees of freedom during inflation.

2.1 Introduction

The paradigm of inflation [47, 71, 72, 70, 55, 18] in its simplest realizations is consistent with the latest data releases from the Planck [7] and WMAP [28] satellites. However, hints of a primordial oscillatory signal in the CMB bispectrum [10] and of anomalies in the CMB power spectrum [28, 9] motivate a search for correlated features produced by inflationary scenarios beyond canonical single-field.¹ Such correlation is in general expected and will differ depending on its physical origin [34], so it can be used to discriminate among inflationary mechanisms.

On the theory side, several mechanisms that produce oscillatory features are being investigated. As first noted in [73], a step in the inflaton potential causes

¹By canonical single-field we mean slow-roll regime, Bunch-Davies vacuum, canonical kinetic terms and minimal coupling to gravity, with speed of sound $c_s = 1$.

features in the spectra [77, 6, 45, 21, 33, 19, 57, 12, 20, 75, 23], and novel methodologies have been developed in [74, 35, 38, 15, 63, 16] for more generic transient slow-roll violations. The effect of a variable speed of sound has also been analysed both in the power spectrum [2, 50, 5] (for sudden variations see [66, 63, 64, 24, 23]) and bispectrum [5, 16, 68] (see [24, 23] for sudden variations). Different initial vacuum states (see e.g. [37, 46, 61, 51]) or multi-field dynamics [44, 43, 69, 65] may also cause oscillations in the primordial spectra.

On the observational side, searches in the CMB power spectrum data have been performed for a variety of scenarios, such as transient slow-roll violations [36, 12, 26, 13, 25, 48, 27, 63], superimposed oscillations in the primordial power spectrum [56, 42, 17, 58, 67, 60, 59] and more general parametric forms (see [9] and references therein). In addition, the Planck collaboration searched for features in the CMB bispectrum for a number of theoretically motivated templates [10]. In none of these cases the statistical significance of the extended models has been found high enough to claim a detection. Still, it is becoming clear that hints of new physics (if any) are most likely to be detected in the correlation between different observables.

In this spirit, in the two papers presented in this chapter we search for transient reductions in the speed of sound of the adiabatic mode consistent with (effectively) single-field inflation and *uninterrupted* slow-roll. We do this by exploiting a very simple correlation between power spectrum and bispectrum noted in [5] and presented in section 1.3.4. While more general situations are possible, and have been considered elsewhere [15, 16], there is a particularly interesting regime for which the *complete* primordial bispectrum is obtained to leading order in slow-roll [5]. The amplitude and the rate of change of the speed of sound must be large enough to dominate over slow-roll effects while being small enough to allow a perturbative calculation of the effect on the power spectrum and bispectrum. We call transient reductions in this regime *mild and moderately sharp*.

Our test case consists of a gaussian reduction in the speed of sound occurring within the window of e -folds in which the scales corresponding to the angular scales probed by Planck exit the Hubble sound horizon. The functional form is inspired by soft turns along a multi-field inflationary trajectory with a large hierarchy of masses, a situation that is consistently described by an effective single-field theory [3, 2, 31, 4] (see also [44, 43]). Nevertheless we stress that reductions in the speed of sound are a more general phenomenon within effective field theory (and hence may have diverse physical origins).

Our statistical analysis of the Planck CMB power spectrum reveals several fits with a moderately improved likelihood compared to the best Λ CDM fit. We performed different tests to check the robustness of the fits found. For each of those fits we give the associated full primordial bispectrum. At the time of writing this thesis, the Planck bispectrum data have not yet been released but, due to a lucky coincidence, templates very similar to our predictions have already been tested by Planck [10] (inspired by a step in the potential). We find that the predicted bispectra for some of our fits are reasonably consistent with the best fits

of Planck. In addition, some of our best fits lie on a region of the parameter space not yet analysed by Planck. If confirmed, these correlations would constitute evidence for transient reductions in the speed of sound. It is interesting that rather mild reductions of the order of a few percent may already be observable in the data.

2.2 Our test case – A gaussian in e -folds

In this chapter, we attempt to fit to the CMB data the kind of features described in section 1.3.4. The features in the CMB temperature power spectrum originate from the perturbations in the scalar primordial power spectrum given by eq. (1.54), in terms of a reduction in the speed of sound $c_s(\tau)$.

We have chosen to parametrise the reduction in the speed of sound as a *gaussian* in e -folds N . This functional form is inspired by soft turns along a multi-field inflationary trajectory with a large hierarchy of masses, a situation that is consistently described by an effective single-field theory and uninterrupted slow roll [3, 2, 31, 4, 44, 43]. Our parametrisation reads:

$$u = 1 - c_s^{-2} = B e^{-\beta(N-N_0)^2} = B e^{-\beta\left(\ln\frac{\tau}{\tau_0}\right)^2}, \quad (2.1)$$

where $\beta > 0$ is the sharpness, $B < 0$ is the amplitude, and N_0 (or τ_0) is the instant of maximal reduction. Assuming slow-roll, the conformal time τ is related to the e -folds of inflation through $\ln(-\tau) = (N_{\text{in}} - N) - \ln(a_{\text{in}}H_0)$, where $a_{\text{in}} = a(N_{\text{in}})$ and N_{in} is the time when the last ~ 60 e -folds of inflation start. Notice that the quantity N_{in} is irrelevant, since all the quantities in e -folds are defined with respect to N_{in} .

There are two main criteria that we followed in order to determine the parameter regions that we would explore:

- (a) The SRFT calculation of the power spectrum and the bispectrum is valid for *mild and moderately sharp* reductions of the speed of sound. Also, the slow-roll contributions to the bispectrum are disregarded with respect to the terms arising from the reduced speed of sound (see [5] or section 1.3.4). This means that the amplitude $|u|$ and the rate of change $s \equiv \frac{\dot{c}_s}{c_s H}$ must be much smaller than one, while being (at least one of them) much larger than the slow-roll parameters. The rate of change s of the speed of sound (2.1) reads:

$$s(N) = \frac{dc_s}{c_s dN} = -\frac{B\beta(N - N_0) e^{-\beta(N-N_0)^2}}{1 - B e^{-\beta(N-N_0)^2}}. \quad (2.2)$$

Since we have to impose $|s| \ll 1$ for all values of N , it suffices to impose this condition at the point where $|s|$ takes its maximum value $|s(N_*)| = |s|_{\text{max}}$,

determined by

$$N_* = N_0 \pm \frac{1}{\sqrt{2\beta}} \sqrt{1 + \mathcal{O}(B)} \simeq N_0 \pm \frac{1}{\sqrt{2\beta}}, \quad (2.3)$$

which approximately corresponds to one standard deviation of our gaussian, and we have used that $|B| \ll 1$. Then the condition $|s|_{\max} \ll 1$ translates into $\beta \ll \frac{2e}{B^2} + \mathcal{O}(B^{-1})$. Altogether, the allowed region of our parameter space taking into account these constraints is

$$\mathcal{O}(\epsilon, \eta) \ll |B| \ll 1, \quad (2.4a)$$

$$\beta_{\min} \ll \beta \ll \frac{2e}{B^2}, \quad (2.4b)$$

$$N_{\text{bb}} < N_0 < N_{\text{end}}, \quad (2.4c)$$

where N_{bb} and N_{end} are respectively the (unknown) instants, in e -folds scale, of the beginning and the end of inflation; on the other hand, β_{\min} corresponds to the case in which $|s|_{\max} \sim \mathcal{O}(\epsilon, \eta)$. Notice that it is only necessary to satisfy one of the lower limits of eqs. (2.4a) or (2.4b).

- (b) The angular scales probed by Planck ($\ell = 2 - 2500$) roughly correspond to the momentum scales crossing the Hubble sound horizon during the first $N_{\text{CMB}} \simeq 7$ e -folds of the last ~ 60 e -folds of inflation. If the data resembles features due to a reduced speed of sound, it is most likely to find them within this *CMB window* (we choose to *look under the lamppost*). This translates into constraints on the parameters that determine the position and width of the feature, namely the sharpness β and the instant N_0 . They are chosen so that the reduction happens well within this CMB window. We took a very conservative definition for the total width of the reduction (in e -folds): ten standard deviations of the gaussian, $\Delta N = 10/\sqrt{2\beta}$, must fit within the observable window $[N_{\text{in}}, N_{\text{in}} + N_{\text{CMB}}]$. Then, the position N_0 and the sharpness β should satisfy

$$\frac{50}{N_{\text{CMB}}^2} < \beta, \quad (2.5a)$$

$$\frac{5}{\sqrt{2\beta}} < N_0 - N_{\text{in}} < N_{\text{CMB}} - \frac{5}{\sqrt{2\beta}}. \quad (2.5b)$$

This is a very conservative choice (or, the *lamppost* reaches actually further): (2.5a) and (2.5b) are more restrictive than the condition that the feature be observable: for example, any feature happening in a particular window has an effect on the modes that leave the horizon after the reduction in c_s has finished, as is shown by the fact that the transfer functions that relate primordial scales when they leave the Hubble sphere to scales in the CMB have a non-zero, finite width. In exchange for a more restrictive constraint,

we avoid degeneracies with the spectral index n_s and the optical depth τ_{reio} that could be caused by reductions with a very long wavelength in the power spectrum.

Finally, putting together the constraints described above, and prioritising the most restrictive of them in each case, we get the final set of bounds

$$\mathcal{O}(\epsilon, \eta) \ll |B| \ll 1, \quad (2.6a)$$

$$\frac{50}{N_{\text{CMB}}^2} < \beta \ll \frac{2e}{B^2}, \quad (2.6b)$$

$$\frac{5}{\sqrt{2\beta}} < N_0 - N_{\text{in}} < N_{\text{CMB}} - \frac{5}{\sqrt{2\beta}}. \quad (2.6c)$$

For computational purposes, we use the parameter $\ln(-\tau_0)$ instead of N_0 for the data analysis. The range for this parameter is taken to be more strongly restricted than by (2.6c):

$$4.4 \leq \ln(-\tau_0) \leq 6. \quad (2.7)$$

The features in the power spectrum and bispectrum are linearly oscillating, as well as those tested in one of the searches for bispectrum features by the Planck collaboration [10, sec. 7.3.3]. The oscillatory frequency is determined by τ_0 , and the range of frequencies covered in Planck's bispectrum analysis is equivalent to the interval $\ln(-\tau_0) \in [4.43, 5.34]$. This motivates us to search in the interval given above, which contains and slightly enlarges that of Planck's search, while at the same time avoids highly oscillating features (larger values of $|\tau_0|$) that make computational control difficult.

As a final step, we choose priors for the three parameters of the feature. In particular, we choose uniform priors in B , $\ln \beta$ and $\ln(-\tau_0)$, within the limits given respectively by eqs. (2.6a), (2.6b) and (2.7). The model-dependent bound $|B| \gg \mathcal{O}(\epsilon, \eta)$ is ignored a priori.

2.3 Methodology of the search

The power spectrum features caused by a transient reduction in the speed of sound described by eq. (2.1), are combined with the primordial spectrum of the Λ CDM Planck baseline model described in [11, sec. 2], parametrized by an amplitude A_s and a spectral index n_s . To do so, we solve the integral in eq. (1.54) using a Fast Fourier Transform. The primordial perturbations evolve in a flat FLRW universe parametrized by the densities of baryonic and cold dark matter, Ω_b and Ω_{cdm} , and the current expansion rate H_0 . The damping due to reionisation is parametrized by the optical depth τ_{reio} . Those 6 standard plus 3 feature parameters describe our cosmological model.

The evolution of the perturbations and their projection onto the CMB power spectrum is calculated with the Boltzmann code CLASS [52, 29]. In order to

incorporate our features to the primordial power spectrum, we needed to develop an extension to CLASS, which is described in chapter 4.

The resulting CMB is fitted to the ESA Planck mission temperature data of March 2013, using the likelihood provided by the experiment [8], and the low- ℓ CMB polarization data of the WMAP experiment [28]. We use flat priors on the 6 Λ CDM parameters and the 14 nuisance parameters of the likelihood [8]. For the parameters of the feature, we use the priors described in the last section. The posterior probability is then maximized over the prior bounds using Markov-Chain Monte-Carlo (MCMC) methods, making use of the MCMC sampler MONTE PYTHON [22].

Multi-modal sampling with Markov Chain Monte Carlo

As is usual when fitting small features on top of a large data set, we found the likelihood pdf (and hence the posterior) to be multi-modal. Although multi-modal distributions are sampled more efficiently with methods such as *multi-modal nested sampling* [41, 40], we managed to sample the posterior pdf by using only MCMC methods. As we explained in section 1.5.7, the reason why MCMC methods fall short when exploring multi-modal pdf's is the need for a very long sampling time in order for the jumping between different modes to occur enough to, at the same time, (1) sampling each of the modes fairly with respect to each other, and (2) finely sampling around each one of them. It is easy to show why it is difficult to have both: finely sampling around each of the modes requires a proposal distribution as close as possible to that of the mode itself, which automatically sets the step size in the parameter space to be much smaller than the distance between well-separated modes, making jumps between them unlikely; on the other hand, an extended proposal distribution characterises better the position of the different modes, but sets the step-size so large that the estimation of the confidence intervals of each of the modes is quite inaccurate, since the sampling around each of the maxima is scarce.

In this work, instead of finding a compromise solution, we took a two-steps approach. First, we sampled the posterior pdf with an extended proposal distribution, in order to find the rough position and shape of the different modes, but renouncing to get accurate parameter constrains for now.² After obtaining a big number of samples, we inspected the resulting *profile* of the posterior pdf in a grid – the profile pdf $\mathcal{P}(\alpha_i)$ in a grid cell i with respect to a subset of the full set of parameters $\{\alpha\} \subset \{\theta\}$ is the maximised pdf with respect to the remaining parameters and the cell volume, $\mathcal{P}(\alpha_i) = \max_{\{\theta\}-\{\alpha\},i} \mathcal{P}(\theta)$. Why the profile and not, as it is usual, the marginal pdf? Because the large extent of the proposal

²It is common in MCMC samplers, when there is no good estimate of the proposal distribution, to start the sampling process with an inaccurate estimate, and then use some of the first samples to obtain a more accurate one and to automatically restart the sampling with this one. Needless to say, in this setting this approach is not appropriate, since we do prefer a rough, long-tailed, inaccurate proposal pdf to be constant during the whole sampling process.

distribution produces a very scarce sampling that makes the different modes only barely visible as over-densities of samples (as local maxima of the marginal likelihood); instead, they are easier to see by directly inspecting the values of the likelihood on a coarse grid.

Second, once the rough shape of the pdf is known, provided that the different modes are clearly separated, one can crop regions of the parameter space containing each a single mode. Over each of those regions, using a rough estimate of the single-mode proposal distribution, one can obtain confidence intervals for the different parameters as one would normally do for uni-modal pdf's. Finally, each of the modes must be assigned a relative probability proportional to the total pdf mass under said mode.

Going back to the particular case under study, as our features are small and affect only a fraction of the data set, we expect to find only mild degeneracies of the feature parameters with the cosmological parameters. Due to the mild character of the degeneracies (that we confirmed a posteriori, cf. fig. 2.2), we expect the likelihood to show its multi-modal character only within the parameter subspace of the feature. Therefore, we started our search by mapping the multi-modal likelihood on this 3-dimensional subspace.

We started our analysis by sampling the parameter sub-space of the feature, $(B, \ln \beta, \ln(-\tau_0))$, with very long tailed chains, of order 5% of the width of the prior in each direction. After obtaining a big number of samples, we inspected the profile posterior in the plane $(\ln \beta, \ln(-\tau_0))$; it revealed the position and rough size of the different modes, and we used that information to crop uni-modal regions. We then reassessed the shape of the modes by sampling over the feature parameters only, and when their position and extension were sufficiently well determined, we resampled them allowing now the baseline Λ CDM and nuisance parameters to vary. With this, we got the definitive posterior probability distribution functions for the different modes.

In the following, χ^2 refers to the so-called *effective* χ^2 defined as $\chi_{\text{eff}}^2 = -2 \ln \mathcal{L}$ (see [76, p. 10]); in turn, $\Delta\chi^2$ stands for the difference with the corresponding best fit value of Planck baseline model, using the likelihoods mentioned above [11]: $\chi_{\text{eff, best-fit}}^2 = 9805.90$.

2.4 Summary and analysis of the results

The result of our search, having discarded small signals with $\Delta\chi^2 > -2$ over Λ CDM, is a series of five well-isolated bands with almost constant $\ln(-\tau_0)$ (i.e. frequency of oscillation of the feature in the primordial spectrum), in which the likelihood is *improved* with variable significance. We will call them, in order of decreasing $\ln(-\tau_0)$, *modes* \mathcal{A} to \mathcal{E} . The resulting profile likelihood can be seen in figure 2.1. For each of the modes showed in the figure, the relevant parameter data is given in table 2.1: the numbers in parentheses are the best fit values, and

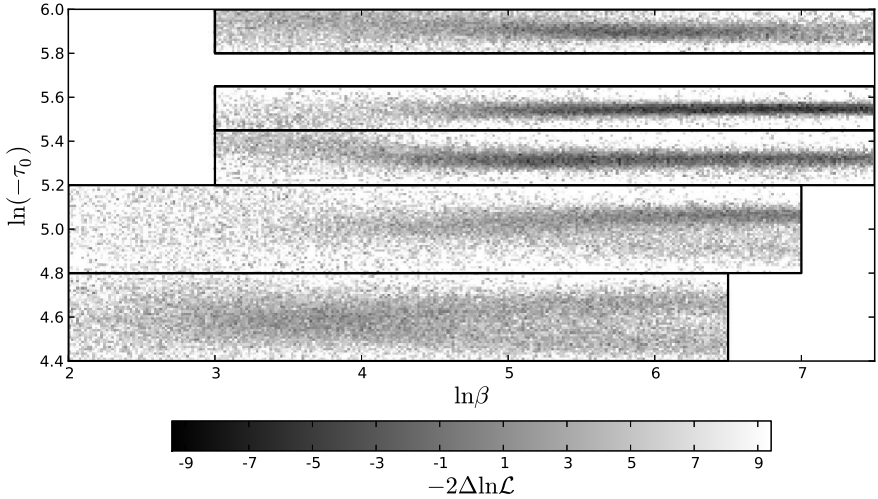


Figure 2.1: Profile of $\Delta\chi^2 = -2\Delta\ln\mathcal{L}$ for the features in the CMB power spectrum in the $(\ln\beta, \ln(-\tau_0))$ plane. We name each of the bands, in descending order of $\ln(-\tau_0)$, *modes* \mathcal{A} to \mathcal{E} . Regions with improvements of $-\Delta\chi^2 < 2$ have been discarded and are not shown in the plot.

Mode	$-B \times 10^2$	$\ln\beta$	$\ln(-\tau_0)$	$\Delta\chi^2$	s_{\max}
\mathcal{A}	(4.5) $3.7^{+1.6}_{-3.0}$	(5.7) $5.7^{+0.9}_{-1.0}$	(5.895) $5.910^{+0.027}_{-0.035}$	-4.3	0.33
\mathcal{B}	(4.2) 4.3 ± 2.0	(6.3) $6.3^{+1.2}_{-0.4}$	(5.547) $5.550^{+0.016}_{-0.015}$	-8.3	0.42
\mathcal{C}	(3.6) $3.1^{+1.6}_{-1.9}$	(6.5) $5.6^{+1.9}_{-0.7}$	(5.331) $5.327^{+0.026}_{-0.034}$	-6.2	0.40
\mathcal{D}	(4.4)	(6.5)	(5.06)	-3.3	0.48
\mathcal{E}^*	(1.5)	(4.0)	(4.61)	-2.2	0.05

Table 2.1: CMB power spectrum best fits (in parentheses), 68% c.l. intervals, effective $\Delta\chi^2$ at the best fit value, and maximum value of the speed of sound derivative s_{\max} , for each of the modes. The prediction for the bispectrum for \mathcal{E} is not reliable (see text).

the parameter ranges, when given, are 68% c.l. regions.

The amplitude B of the fits is rather small, $\mathcal{O}(10^{-2})$, and therefore comparable with neglected slow-roll terms. This means the bispectrum is dominated by terms of order $s = \dot{c}_s/(Hc_s)$. The maximum values of s at the best fits for the modes \mathcal{A} to \mathcal{E} in table 2.1 are respectively 0.33, 0.42, 0.40, 0.48, 0.05. Notice that the value of s for \mathcal{E} is also comparable to neglected terms, so the prediction for the bispectrum based on eq. (1.55) cannot be trusted in this case. We therefore disregard this mode in the comparison with the bispectrum.

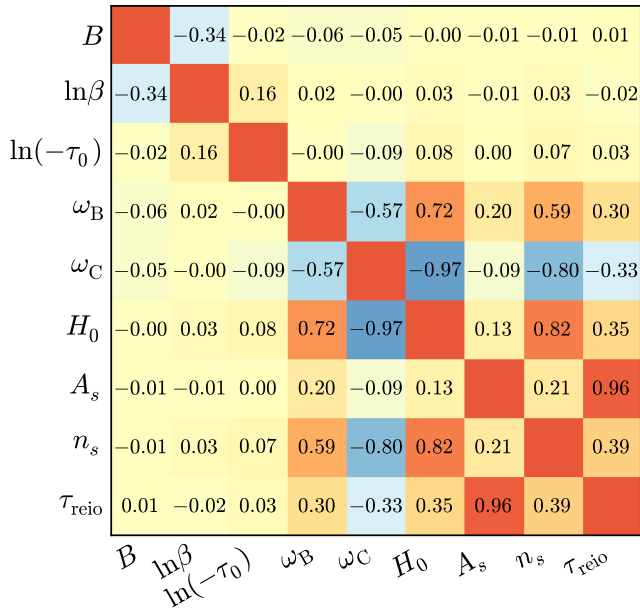


Figure 2.2: Correlation coefficients between the feature and the cosmological parameters for the mode \mathcal{B} . Notice the small correlations between the two sets of parameters, and the rather large negative correlation between B and $\ln\beta$.

For the modes \mathcal{A} , \mathcal{B} and \mathcal{C} the table 2.1 shows the 68% c.l. ranges. For bands \mathcal{B} and \mathcal{C} we were unable to put an upper bound on $\ln\beta$ due to a degeneracy between that parameter and the amplitude $|B|$, as we will explain below. For those two modes, the upper bound on $\ln\beta$ is set by the prior $s < 1$ in eq. (2.6b), which is saturated at $\ln\beta \simeq 7.5$.

The lower bands \mathcal{D} (and \mathcal{E}) are less significant and their likelihoods much less gaussian, so we only show their best fits. Despite their low significance, they are worthy of mention because they fall in the region overlapping with Planck's search for features in the bispectrum (see below).

The best fits and 68% c.l. ranges of the six Λ CDM parameters [11]³ are quite accurately reproduced, see table 2.2. As expected, we find only small degeneracies⁴ ($|\rho| \leq 0.15$) between the feature parameters and the Λ CDM parameters for modes \mathcal{A} , \mathcal{B} and \mathcal{C} . The correlation matrix for the mode \mathcal{B} is shown in fig. 2.2. For the less significant modes \mathcal{D} and \mathcal{E} , some of the correlations grow up to $|\rho| \leq 0.30$.

³See also the parameter tables at http://www.sciops.esa.int/wikiSI/planckpla/index.php?title=File:Grid_limit68.pdf&instance=Planck_Public_PLA.

⁴The correlation matrix is defined as $\rho_{ij} \equiv C_{ij}/\sqrt{C_{ii} \cdot C_{jj}}$, where C_{ij} are the covariance matrix elements corresponding to the parameters with indices i and j .

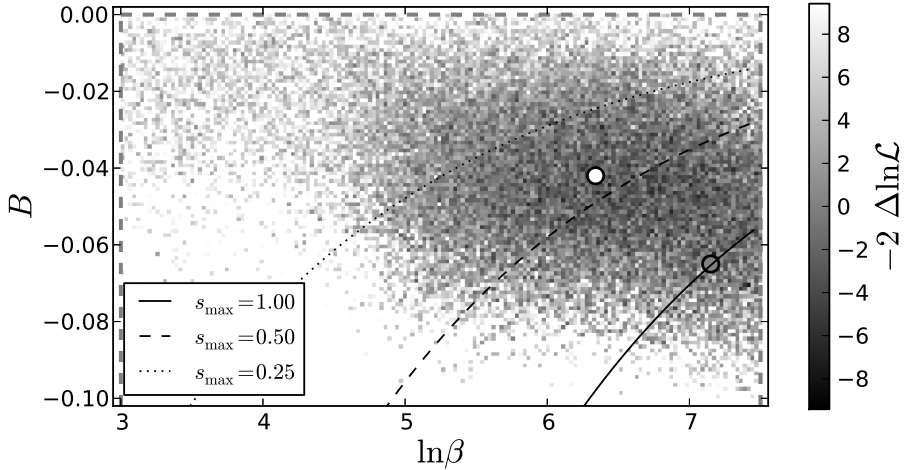


Figure 2.3: Profile of $\Delta\chi^2 = -2\Delta\ln\mathcal{L}$ for the mode \mathcal{B} in the $(\ln\beta, B)$ plane, showing the $\rho = -0.34$ degeneracy between those two parameters. Some lines of $s_{\max} = \text{const}$ are shown. Notice how the mode extends beyond the $s = 1$ prior limit.

This is expected, since for lower $\ln(-\tau_0)$ the frequency of the fits drops, getting closer to the frequency of the acoustic oscillations.

A gain of $|\Delta\chi^2| \lesssim 10$ is common in similar searches (see section 2.4.4 for a comparison with other searches for features in the CMB power spectrum), which suggests that CMB power spectrum data alone cannot justify the introduction of these features. Nevertheless, the aim of this chapter is to show that low-significance fits can still predict correlated features in the bispectrum which are possibly observable with the current data. Model selection should be done using the full parameter ranges allowed by the theory and taking into account both power spectrum and bispectrum, and, if possible, adding other data sets with uncorrelated systematic effects, such as Large Scale Structure (see chapter 3).

2.4.1 The degeneracy of B and $\ln\beta$ – upper limit of $\ln\beta$

In this section we comment on one characteristic of the modes \mathcal{B} and \mathcal{C} (and also \mathcal{D}): a positive correlation between $\ln\beta$ and $|B|$: the CMB temperature data is not able to restrict the maximum value of $\ln\beta$, as one can see in figure 2.1 and in the 1D marginalized likelihood of $\ln\beta$ in figure 2.6 (middle-right panel). In each mode, after some value of $\ln\beta$, the likelihood reaches a plateau with constant $\ln(-\tau_0)$; along this direction of increasing $\ln\beta$, the best-fit amplitude B grows (see fig. 2.3), correlated with $\ln\beta$ with correlation coefficient of order $\rho \sim -0.3$ (cf. fig. 2.2). The simultaneous growth of $|B|$ and $\ln\beta$ in some of these plateaus

causes that at some point the prior limit $s < 1$ in eq. (2.6b) gets saturated, in particular at $\ln \beta \simeq 7.5$ (see figure 2.3), and hence the prior sets the upper bound for $\ln \beta$.

From the CMB power spectrum point of view, the reason for this to happen is the following: along the direction of simultaneous increase of $\ln \beta$ and $|B|$, the feature in the *primordial* power spectrum broadens towards smaller scales, while the amplitude of the tail on the larger scales remains almost constant (see 2.4, top). Since at smaller scales much of the primordial signal is suppressed by diffusion damping in the CMB, no significance is gained along the degeneracy direction, causing a plateau in $\Delta\chi^2$. This can be seen illustrated for mode \mathcal{B} in figure 2.4: we compare two of the best fits of this mode, one sitting well within the prior bounds (white circle in figure 2.3), and a similar fit (grey circle in figure 2.3) that improves $\Delta\chi^2$ marginally and saturates the $s = 1$ bound. In figure 2.4 we can see the effect of those fits in the primordial and CMB temperature power spectrum. Notice how the big difference between both fits in the former gets diluted in the latter.

Can we resolve this ambiguity? Probably: photon diffusion at the last scattering surface has the effect of polarizing the CMB signal through Thomson scattering, so at smaller scales the polarization spectrum will contain information about the primordial spectrum, complementary to that of the temperature spectrum. Therefore, the difference at small scales between two fits in the same plateau (here, the dashed and dotted spectra in figure 2.4) is larger in the TE and EE CMB polarization spectra (see fig. 2.5). This suggests that the high- ℓ Planck polarization data, expected to be released along 2014, may be able to set stringer bounds on the maximum value of $\ln \beta$, as well as confirm that we are not fitting noise.

2.4.2 Cross-check with a different Boltzmann code

In order to make our results from CLASS+MONTE PYTHON more reliable, we cross-checked them with an independent Einstein-Boltzmann solver and a different MCMC sampler, namely CAMB [54] and COSMOMC [53]. As an example, in fig. 2.6 and tab. 2.2 we explicitly show this comparison for the most significant mode \mathcal{B} by varying both the primary Λ CDM parameters and the additional sound speed reduction parameters. We find excellent agreement between these two results.

2.4.3 Local improvement at different angular scales: $\Delta\chi^2(\ell)$

Given a fit to the CMB power spectrum of some feature model, it is interesting to know in which ranges of multipoles the feature describes the data better than the baseline Λ CDM model. This kind of *local improvement* can only be calculated approximately, since the temperature data points at different multipoles are in general correlated. Nevertheless, even a qualitative analysis can shed some light on where the feature fits better the data than the baseline model.

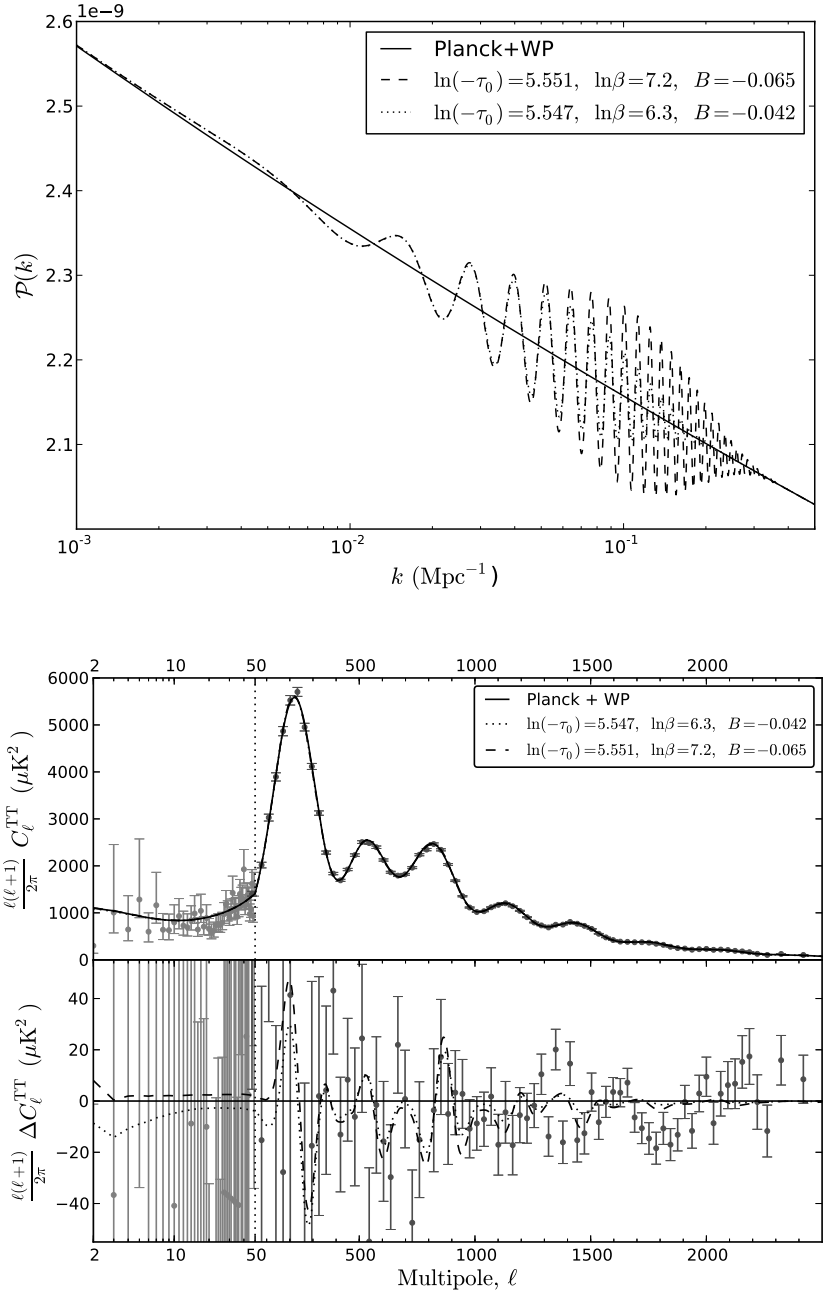


Figure 2.4: Comparison of the two fits indicated in figure 2.3 with a white circle (dotted line) and a grey circle (dashed line), in the primordial power spectrum and the TT CMB power spectrum.

2.4 Summary and analysis of the results

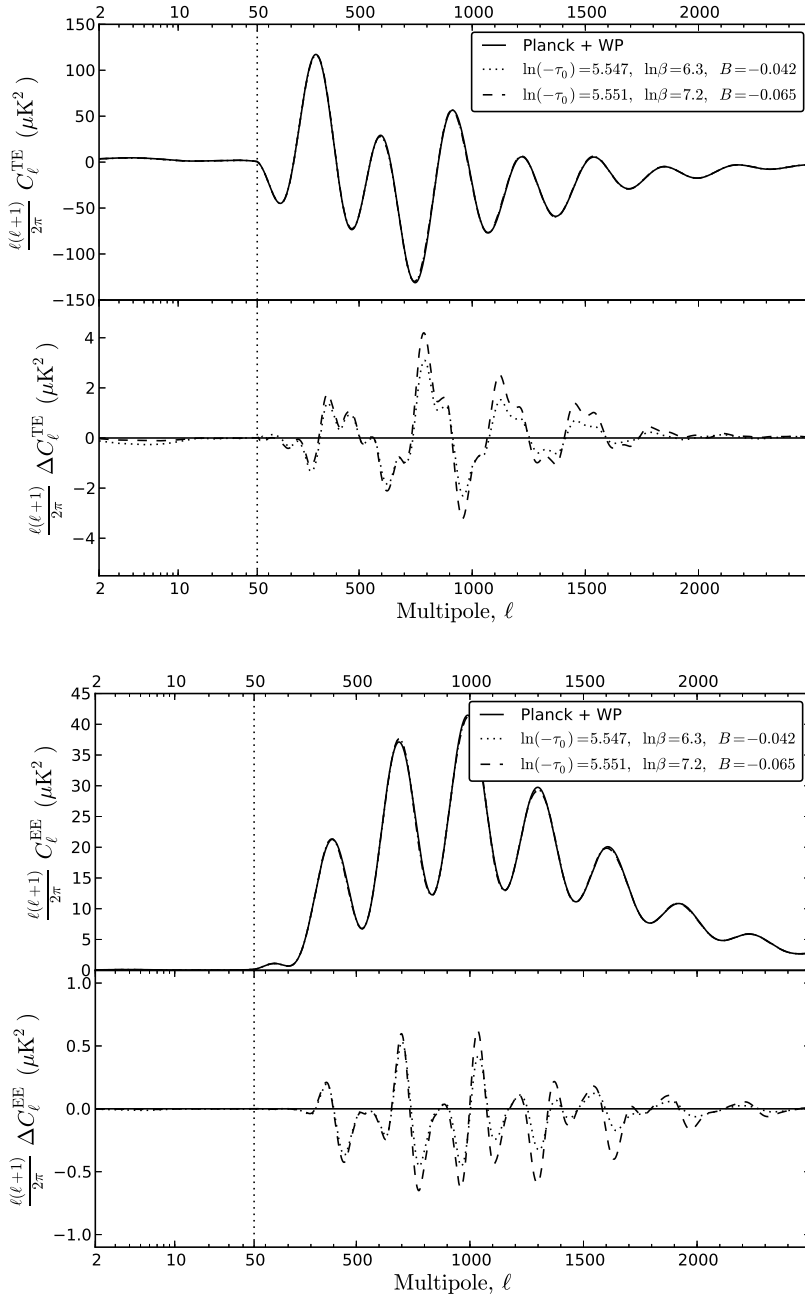


Figure 2.5: Comparison of the two fits indicated in figure 2.3 with a white circle (dotted line) and a grey circle (dashed line), in the TE and EE CMB power spectra.

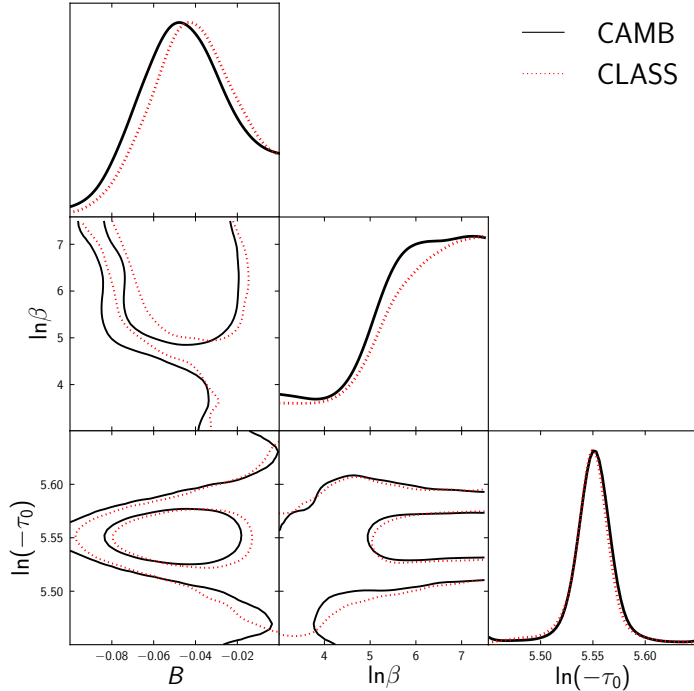


Figure 2.6: CAMB+CosmoMC vs. CLASS+MONTE PYTHON consistency check: 1D and 2D marginalized posterior distributions of the sound speed reduction parameters for the mode \mathcal{B} .

We have studied the local improvements along the multipoles of the four relevant fits, modes \mathcal{A} to \mathcal{D} (we show the result for mode \mathcal{B} in figure 2.7). To do that, we have binned the multipoles with $\Delta\ell = 20$ and substituted pieces of the best fit for each mode into the best fit of the Λ CDM baseline model. For the sake of simplicity, we use for this analysis the preliminary fits found by keeping the cosmological and nuisance parameters fixed to their best fit values (hence the small difference in the total $\Delta\chi^2$ between fig. 2.7 and tab. 2.1).

The results show that mode \mathcal{A} gains its significance mostly in the first and third peak and loses some of it in the second; mode \mathcal{B} (see fig. 2.7) and \mathcal{C} gain most of their significance in the third peak, lose some of it in the fourth peak and improve a little again in the fifth and sixth. The mode \mathcal{D} does not fit well the first and second peaks, gains most of its significance in the third peak, and some more in the fifth and sixth peaks.

<i>Planck</i> +WP			
Parameter	CAMB	CLASS	Baseline [11]
$100\Omega_b h^2$	2.208 ± 0.027	2.214 ± 0.029	2.205 ± 0.028
$\Omega_c h^2$	0.1204 ± 0.0026	0.1203 ± 0.0027	0.1199 ± 0.0027
τ_{reio}	0.089 ± 0.013	0.090 ± 0.013	$0.089^{+0.012}_{-0.014}$
H_0	67.16 ± 1.14	67.29 ± 1.21	67.3 ± 1.2
n_s	0.9600 ± 0.0070	0.9598 ± 0.0074	0.9603 ± 0.0073
$\ln(10^{10} A_s)$	3.090 ± 0.023	3.088 ± 0.024	$3.089^{+0.024}_{-0.027}$
B	$-0.045^{+0.045}_{-0.034}$ (95%c.l.)	$-0.041^{+0.041}_{-0.031}$ (95%c.l.)	—
$\ln \beta$	$6.00^{+1.50}_{-3.00}$ (95%c.l.)	$6.06^{+1.44}_{-2.18}$ (95%c.l.)	—
$\ln(-\tau_0)$	5.55 ± 0.06 (95%c.l.)	5.55 ± 0.05 (95%c.l.)	—
χ_{bf}^2	9797.25	9797.58	9805.90

Table 2.2: CAMB+CosmoMC vs. CLASS+MONTE PYTHON consistency check: mean values and 68% (or 95% where indicated) confidence intervals for the primary Λ CDM parameters and the additional sound speed reduction parameters for the mode \mathcal{B} . We also show the parameter ranges found by the Planck collaboration [11] for a featureless model.

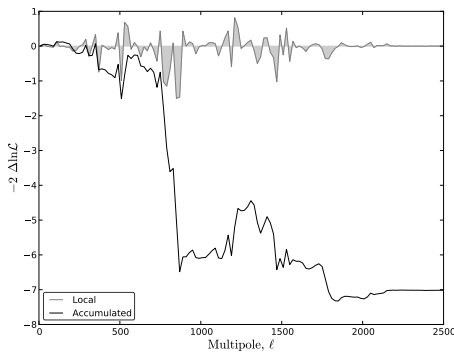


Figure 2.7: Local gain in the likelihood of the best fit of mode \mathcal{B} along the multipoles. The grey area shows the local difference in each bin, and the black line shows the accumulated difference for increasing multipoles.

2.4.4 Comparison with other searches for features in the CMB power spectrum

Due to the Fourier transform in eq. (1.54), our features oscillate as $\exp(i2k\tau_0)$. Thus it is natural to compare to other searches for linearly oscillating features in the Planck CMB power spectrum.

Ref. [59] searches for non-localized features with frequencies that compare to ours as $\omega_2 = 2|\tau_0|$. In the overlapping region, $\omega_2 \in [160, 810]$, they find peaks at roughly $\ln(-\tau_0) \sim \{5.0, 5.1, 5.3, 5.6, 5.7\}$ ($|\Delta\chi_{\text{bf}}^2| \simeq 8$). We find three peaks in this region with similar significance; it could be that the discrepancies come from

signals at scales at which our (localized) features are negligible.

Also, the Planck collaboration [9, sec. 8] searches for features motivated by step-inflation, using the parametrization proposed in [13] with a frequency $\eta_f = |\tau_0|$. The profile likelihood in [9, fig. 19, middle] reveals peaks at $\ln \eta_f \in [4.5, 4.8]$ ($|\Delta\chi_{\text{bf}}^2| \simeq 2$) and $\ln \eta_f \in [5.3, 5.7]$ ($|\Delta\chi_{\text{bf}}^2| \simeq 8$), which is consistent with our results.

It is worth noting that in both searches above the overall best fit occurs at $\ln(-\tau_0) \simeq 8.2$ ($|\Delta\chi_{\text{bf}}^2| \sim 14$), too high a frequency for the scope of this work. In [9], and also later in [25, 62], this particular fit has been interpreted as a signal from a step in the inflationary potential. However, in [14, 30] it is argued that the best-fit values of the feature parameters lie outside the allowed theoretical bounds, making its interpretation as a step in the potential inconsistent.

2.5 Comparison with the search for features in Planck's bispectrum

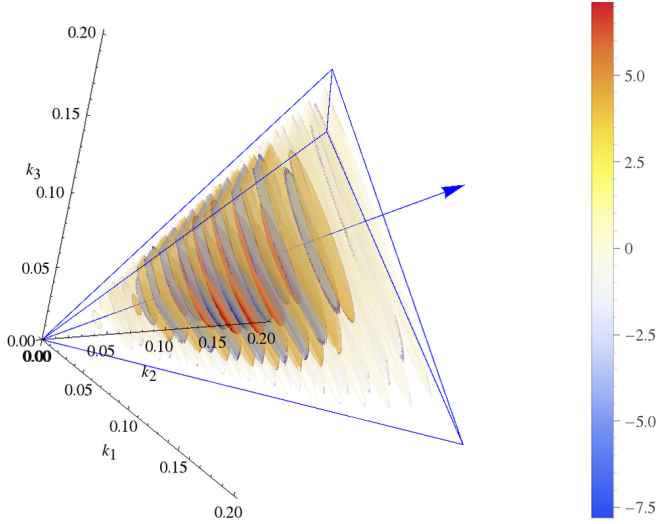
Now that we have put the reliability of our results to the test, we are in a good place to make predictions on the kind of features we expect to see in the bispectrum of the next data release of Planck, if any. They are simply those given by eq. (1.55) evaluated within the c.l. intervals in table 2.1, with relative probabilities to be found given by the best fit likelihood values of each mode. As an example, the bispectrum corresponding to the best fit of mode \mathcal{B} can be seen in fig. 2.8). While we wait for the next data release of the Planck survey, we can try to assess the fulfilment of this predictions based on the preliminary results for the bispectrum published in the Planck data release of March 2013 [10].

A search for linearly oscillatory features was performed in Planck's bispectrum (cf. [10, sec. 7.3.3]), using as a template [32]

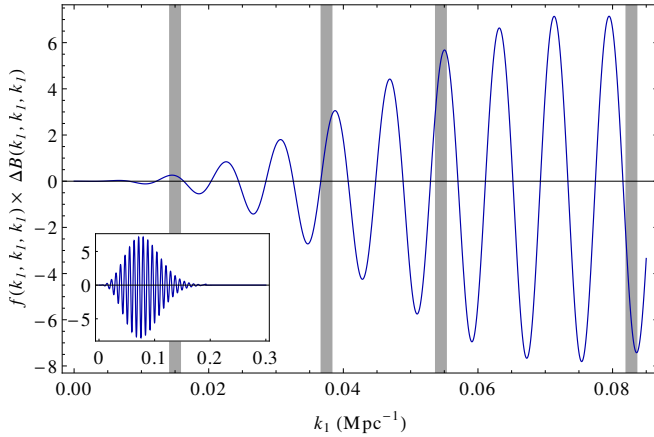
$$B(k_1, k_2, k_3) = \frac{6A^2 f_{\text{NL}}^{\text{feat}}}{(k_1 k_2 k_3)^2} \sin \left(2\pi \frac{\sum_{i=1}^3 k_i}{3k_c} + \phi \right), \quad (2.8)$$

where $A = A_s k_*^{1-n_s}$, A_s and n_s being the amplitude and spectral index of the primordial power spectrum, and $k_* = 0.05 \text{ Mpc}^{-1}$ a pivot scale. They sampled the amplitude $f_{\text{NL}}^{\text{feat}}$ over a coarse grid of wavelengths k_c and phases ϕ .

Our features also present a linearly oscillatory pattern, which comes from the Fourier transform in (1.54). These oscillations enter the bispectrum approximately as $\exp(i \sum_i k_i \tau_0)$, cf. eq. (1.55) and (1.54), which compares to Planck's search as $\tau_0 \approx 2\pi/(3k_c)$. Thus, Planck's search falls inside $\ln(-\tau_0) \in [4.43, 5.34]$, while ours spans up to $\ln(-\tau_0) = 6$ ($k_c = 0.00519 \text{ Mpc}^{-1}$). The overlap includes our modes \mathcal{C} and \mathcal{D} (and also the discarded \mathcal{E}). For every combination of the feature parameter values in the regions of high likelihood, one can find a combination of the parameters in [10] (including a gaussian envelope as described there) such that the correlation between both shapes at the primordial level is at least 95%.



(a) Full 3D primordial bispectrum (in colour in the the on-line version of [1])



(b) Equilateral limit. The grey stripes show the approximate scales of the first four acoustic peaks in the CMB power spectrum, and a zoom-out is shown at the lower-left corner. Most of the signal at high k , i.e. small scales, would be suppressed by diffusion damping when transferred to the CMB.

Figure 2.8: Prediction for the *primordial* bispectrum for the best fit of mode \mathcal{B} , normalized by $f(k_1, k_2, k_3) = (10/3) [(2\pi)^2 A_s k_*^{1-n_s}]^{-2} \prod_i k_i^3 / \sum_i k_i^3$.

The search in [10] is later supplemented with a gaussian envelope centred at scales corresponding to the first acoustic peak, which dampens the signal in subsequent peaks for decreasing values of a falloff Δk .⁵ The envelope generally improves the significance, except for the 2σ signal at $k_c = 0.01375, 0.01500 \text{ Mpc}^{-1}$. This suggests that this band’s significance comes mostly from the second and third peaks (the signal from the fourth on would be most likely damped out).

In comparison, our best fits to the power spectrum predict bispectrum features which are mild at the first peak and more intense from the second peak onwards. The higher the value of $\ln \beta$, the smaller the scale at which the feature peaks. In the range of $\ln(-\tau_0)$ probed here, we were not able to reproduce the improvement Planck appears to see for features at the first peak. On the other hand, we find good matching around the second and third peak scales between the best fit of \mathcal{D} with $k_c = 0.01327 \text{ Mpc}^{-1}$ and the 2.3σ signal of Planck at $k_c = 0.01375 \text{ Mpc}^{-1}$ with $f_{\text{NL}}^{\text{feat}} = 345$ and $\phi = \pi/2$ (see fig. 2.9). A similar but milder qualitative matching also occurs on the same scales between the best fit of \mathcal{C} with $k_c = 0.01014 \text{ Mpc}^{-1}$ and Planck’s 2.6σ signal with $k_c = 0.01125 \text{ Mpc}^{-1}$. Although these matchings are not easy to quantify at the moment of writing this thesis, they suggest enlarging the search in [10] to test envelopes centred at smaller scales, and also to cover the frequencies corresponding to modes \mathcal{A} and \mathcal{B} .

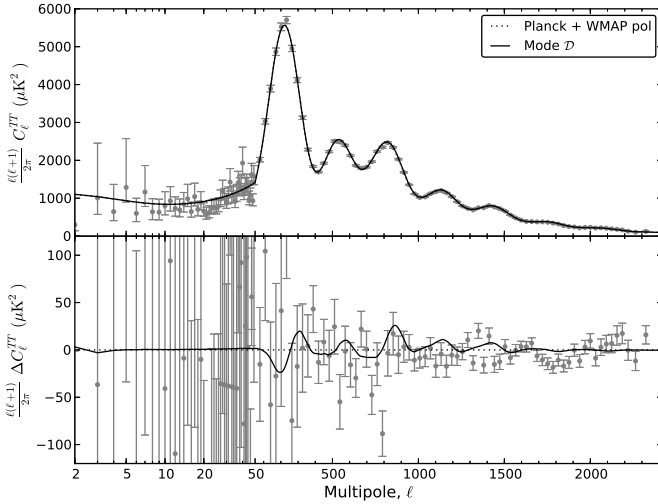
Note that we have quoted the fits to the Bispectrum of Planck without applying the *look-elsewhere effect*. This effect will be properly taken into account when a full study of the Bayesian evidence is performed in a future work, and it is expected to reduce the significance in a much smaller amount [39] than that quoted in [10], since the signals in both data sets, spectrum and bispectrum, are sampled over a single parameter space.

2.6 Conclusions and discussion

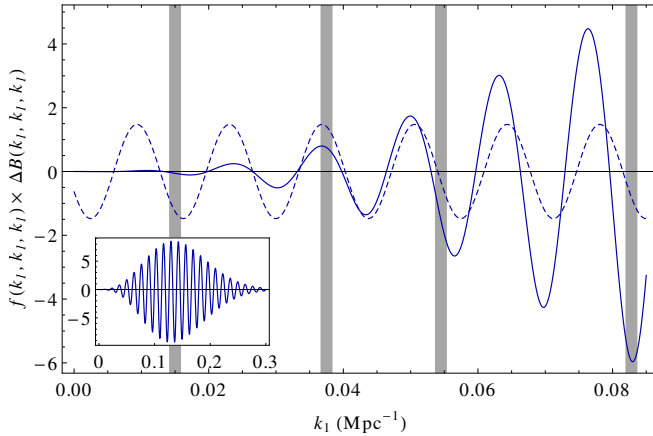
We have carried out a statistical search for localized oscillatory features in the CMB power spectrum produced by a transient reduction in the speed of sound. We have found a number of fits and we have performed additional tests to the results. Namely, we have tried to replicate them using independent codes and found practically equal results; we have studied more explicitly the small degeneracies among the cosmological and feature parameters, and proposed the CMB TE and EE polarization spectra as a way to break degeneracies among the latter; and finally we have investigated at which multipoles each of our fits describe the CMB temperature data better than the baseline Λ CDM model.

For each of the modes, we have calculated the associated primordial bispectra. Because of the small amplitude at the best fits, the bispectrum prediction closely resembles that of step inflation, tested by the Planck collaboration, since a transient slow-roll violation switches on the same operator in the cubic action. It is then straightforward to compare our prediction with the templates used in that

⁵James Fergusson, private communication.



(a) Comparison of Planck's CMB power spectrum (dotted) and the corresponding best fit of the mode \mathcal{D} (solid).



(b) Comparison along the equilateral direction of Planck's 2.3σ *primordial* bispectrum fit with $k_c = 0.01375 \text{ Mpc}^{-1}$ (dashed), and the expected signal in the *primordial* bispectrum for the best fit of \mathcal{D} (solid). Both bispectra are normalized by $f(k_1, k_2, k_3) = (10/3) \left((2\pi)^2 A_s k_*^{1-n_s} \right)^{-2} \prod_i k_i^3 / \sum_i k_i^3$. The grey stripes show the approximate scales corresponding to the first four acoustic peaks in the CMB power spectrum. Although our signal extends beyond those scales (see zoom-out at the lower-left corner), from the third peak on, the primordial signal is highly suppressed by diffusion damping when transferred to the CMB.

Figure 2.9: Features corresponding to the best fit of the mode \mathcal{D} (see table 2.1), for which the comparison with Planck analysis for the bispectrum is possible.

search, and the agreement is surprisingly good. This is remarkable, considering that these bispectrum features are *predicted from a search in the CMB power spectrum* with a very simple *ansatz* for c_s .

The functional form chosen for the reduction in the speed of sound is inspired by soft turns in a multi-field inflationary trajectory with a large hierarchy of masses, a situation that is consistent with an effectively single-field description with uninterrupted slow-roll. Other functional forms and parameter ranges are under investigation. We stress that our analysis is independent of the physical mechanism behind the reduction.

We emphasize that the CMB power spectrum data alone can hardly justify the introduction of features on top of the Λ CDM model; a gain of $|\Delta\chi^2| \lesssim 10$ is not uncommon. However, as we have shown, low-significance fits in the power spectrum can still predict correlated features that may be observable in the CMB bispectrum. Therefore, model selection should take into account both observables simultaneously.

The ability to make predictions in a wider region of the parameter space of features is of particular relevance, since new data sets may allow us to explore it. Besides, since different experiments generally have different foregrounds and systematics, a joint analysis could reduce the contamination of the primordial signal on the overlapping scales. In particular, we later extended our search to large scale structure surveys, see [49] or chapter 3.

Our results suggest that, by exploiting correlations between different observables, current data might already be sensitive enough to detect transient reductions in the speed of sound as mild as a few percent, opening a new window for the presence of extra degrees of freedom during inflation.

Bibliography

- [1] Ana Achúcarro, Vicente Atal, Pablo Ortiz, and Jesus Torrado. Localized correlated features in the CMB power spectrum and primordial bispectrum from a transient reduction in the speed of sound. *Phys.Rev.*, D89:103006, 2014, 1311.2552.
- [2] Ana Achúcarro, Jinn-Ouk Gong, Sjoerd Hardeman, Gonzalo A. Palma, and Subodh P. Patil. Features of heavy physics in the CMB power spectrum. *JCAP*, 1101:030, 2011, 1010.3693.
- [3] Ana Achúcarro, Jinn-Ouk Gong, Sjoerd Hardeman, Gonzalo A. Palma, and Subodh P. Patil. Mass hierarchies and non-decoupling in multi-scalar field dynamics. *Phys.Rev.*, D84:043502, 2011, 1005.3848.
- [4] Ana Achúcarro, Jinn-Ouk Gong, Sjoerd Hardeman, Gonzalo A. Palma, and Subodh P. Patil. Effective theories of single field inflation when heavy fields matter. *JHEP*, 1205:066, 2012, 1201.6342.

- [5] Ana Achucarro, Jinn-Ouk Gong, Gonzalo A. Palma, and Subodh P. Patil. Correlating features in the primordial spectra. *Phys.Rev.*, D87:121301, 2013, 1211.5619.
- [6] Jennifer A. Adams, Bevan Cresswell, and Richard Easther. Inflationary perturbations from a potential with a step. *Phys.Rev.*, D64:123514, 2001, astro-ph/0102236.
- [7] P.A.R. Ade et al. Planck 2013 results. I. Overview of products and scientific results. 2013, 1303.5062.
- [8] P.A.R. Ade et al. Planck 2013 results. XV. CMB power spectra and likelihood. 2013, 1303.5075.
- [9] P.A.R. Ade et al. Planck 2013 results. XXII. Constraints on inflation. 2013, 1303.5082.
- [10] P.A.R. Ade et al. Planck 2013 Results. XXIV. Constraints on primordial non-Gaussianity. 2013, 1303.5084.
- [11] P.A.R. Ade et al. Planck 2013 results. XVI. Cosmological parameters. *Astron.Astrophys.*, 2014, 1303.5076.
- [12] Peter Adshead, Cora Dvorkin, Wayne Hu, and Eugene A. Lim. Non-Gaussianity from Step Features in the Inflationary Potential. *Phys.Rev.*, D85:023531, 2012, 1110.3050.
- [13] Peter Adshead and Wayne Hu. Fast Computation of First-Order Feature-Bispectrum Corrections. *Phys.Rev.*, D85:103531, 2012, 1203.0012.
- [14] Peter Adshead and Wayne Hu. Bounds on non-adiabatic evolution in single-field inflation. *Phys.Rev.*, D89:083531, 2014, 1402.1677.
- [15] Peter Adshead, Wayne Hu, Cora Dvorkin, and Hiranya V. Peiris. Fast Computation of Bispectrum Features with Generalized Slow Roll. *Phys.Rev.*, D84:043519, 2011, 1102.3435.
- [16] Peter Adshead, Wayne Hu, and Vin?cius Miranda. Bispectrum in Single-Field Inflation Beyond Slow-Roll. *Phys.Rev.*, D88:023507, 2013, 1303.7004.
- [17] Moumita Aich, Dhiraj Kumar Hazra, L. Sriramkumar, and Tarun Souradeep. Oscillations in the inflaton potential: Complete numerical treatment and comparison with the recent and forthcoming CMB datasets. *Phys.Rev.*, D87:083526, 2013, 1106.2798.
- [18] Andreas Albrecht and Paul J. Steinhardt. Cosmology for Grand Unified Theories with Radiatively Induced Symmetry Breaking. *Phys.Rev.Lett.*, 48:1220–1223, 1982.

- [19] Frederico Arroja, Antonio Enea Romano, and Misao Sasaki. Large and strong scale dependent bispectrum in single field inflation from a sharp feature in the mass. *Phys.Rev.*, D84:123503, 2011, 1106.5384.
- [20] Frederico Arroja and Misao Sasaki. Strong scale dependent bispectrum in the Starobinsky model of inflation. *JCAP*, 1208:012, 2012, 1204.6489.
- [21] Amjad Ashoorioon and Axel Krause. Power Spectrum and Signatures for Cascade Inflation. 2006, hep-th/0607001.
- [22] Benjamin Audren, Julien Lesgourgues, Karim Benabed, and Simon Prunet. Conservative Constraints on Early Cosmology: an illustration of the Monte Python cosmological parameter inference code. *JCAP*, 1302:001, 2013, 1210.7183.
- [23] Nicola Bartolo, Dario Cannone, and Sabino Matarrese. The Effective Field Theory of Inflation Models with Sharp Features. *JCAP*, 1310:038, 2013, 1307.3483.
- [24] Rachel Bean, Xingang Chen, Girma Hailu, S.-H. Henry Tye, and Jiajun Xu. Duality Cascade in Brane Inflation. *JCAP*, 0803:026, 2008, 0802.0491.
- [25] M. Benetti. Updating constraints on inflationary features in the primordial power spectrum with the Planck data. *Phys.Rev.*, D88(8):087302, October 2013, 1308.6406.
- [26] Micol Benetti, Massimiliano Lattanzi, Erminia Calabrese, and Alessandro Melchiorri. Features in the primordial spectrum: new constraints from WMAP7+ACT data and prospects for Planck. *Phys.Rev.*, D84:063509, 2011, 1107.4992.
- [27] Micol Benetti, Stefania Pandolfi, Massimiliano Lattanzi, Matteo Martinelli, and Alessandro Melchiorri. Featuring the primordial power spectrum: new constraints on interrupted slow-roll from CMB and LRG data. *Phys.Rev.*, D87:023519, 2013, 1210.3562.
- [28] C.L. Bennett et al. Nine-Year Wilkinson Microwave Anisotropy Probe (WMAP) Observations: Final Maps and Results. *Astrophys.J.Suppl.*, 208:20, 2013, 1212.5225.
- [29] Diego Blas, Julien Lesgourgues, and Thomas Tram. The Cosmic Linear Anisotropy Solving System (CLASS) II: Approximation schemes. *JCAP*, 1107:034, 2011, 1104.2933.
- [30] Dario Cannone, Nicola Bartolo, and Sabino Matarrese. Perturbative Unitarity of Inflationary Models with Features. *Phys.Rev.*, D89:127301, 2014, 1402.2258.

- [31] Sebastian Cespedes, Vicente Atal, and Gonzalo A. Palma. On the importance of heavy fields during inflation. *JCAP*, 1205:008, 2012, 1201.4848.
- [32] Xingang Chen, Richard Easther, and Eugene A. Lim. Large Non-Gaussianities in Single Field Inflation. *JCAP*, 0706:023, 2007, astro-ph/0611645.
- [33] Xingang Chen, Richard Easther, and Eugene A. Lim. Generation and Characterization of Large Non-Gaussianities in Single Field Inflation. *JCAP*, 0804:010, 2008, 0801.3295.
- [34] Clifford Cheung, Paolo Creminelli, A. Liam Fitzpatrick, Jared Kaplan, and Leonardo Senatore. The Effective Field Theory of Inflation. *JHEP*, 0803:014, 2008, 0709.0293.
- [35] Jeongyeol Choe, Jinn-Ouk Gong, and Ewan D. Stewart. Second order general slow-roll power spectrum. *JCAP*, 0407:012, 2004, hep-ph/0405155.
- [36] Laura Covi, Jan Hamann, Alessandro Melchiorri, Anze Slosar, and Irene Sorbera. Inflation and WMAP three year data: Features have a Future! *Phys.Rev.*, D74:083509, 2006, astro-ph/0606452.
- [37] Ulf H. Danielsson. A Note on inflation and transPlanckian physics. *Phys.Rev.*, D66:023511, 2002, hep-th/0203198.
- [38] Cora Dvorkin and Wayne Hu. Generalized Slow Roll for Large Power Spectrum Features. *Phys.Rev.*, D81:023518, 2010, 0910.2237.
- [39] J.R. Fergusson, H.F. Gruetjen, E.P.S. Shellard, and M. Liguori. Combining power spectrum and bispectrum measurements to detect oscillatory features. 2014, 1410.5114.
- [40] F. Feroz, M.P. Hobson, and M. Bridges. MultiNest: an efficient and robust Bayesian inference tool for cosmology and particle physics. *Mon.Not.Roy.Astron.Soc.*, 398:1601–1614, 2009, 0809.3437.
- [41] Farhan Feroz and M.P. Hobson. Multimodal nested sampling: an efficient and robust alternative to MCMC methods for astronomical data analysis. *Mon.Not.Roy.Astron.Soc.*, 384:449, 2008, 0704.3704.
- [42] Raphael Flauger, Liam McAllister, Enrico Pajer, Alexander Westphal, and Gang Xu. Oscillations in the CMB from Axion Monodromy Inflation. *JCAP*, 1006:009, 2010, 0907.2916.
- [43] X. Gao, D. Langlois, and S. Mizuno. Oscillatory features in the curvature power spectrum after a sudden turn of the inflationary trajectory. *JCAP*, 10:23, 2013, 1306.5680.

- [44] Xian Gao, David Langlois, and Shuntaro Mizuno. Influence of heavy modes on perturbations in multiple field inflation. *JCAP*, 1210:040, 2012, 1205.5275.
- [45] Jinn-Ouk Gong. Breaking scale invariance from a singular inflaton potential. *JCAP*, 0507:015, 2005, astro-ph/0504383.
- [46] Brian R. Greene, Koenraad Schalm, Gary Shiu, and Jan Pieter van der Schaar. Decoupling in an expanding universe: Backreaction barely constrains short distance effects in the CMB. *JCAP*, 0502:001, 2005, hep-th/0411217.
- [47] Alan H. Guth. The Inflationary Universe: A Possible Solution to the Horizon and Flatness Problems. *Phys.Rev.*, D23:347–356, 1981.
- [48] Jan Hamann, Laura Covi, Alessandro Melchiorri, and Anze Slosar. New Constraints on Oscillations in the Primordial Spectrum of Inflationary Perturbations. *Phys.Rev.*, D76:023503, 2007, astro-ph/0701380.
- [49] Bin Hu and Jesús Torrado. Searching for primordial localized features with CMB and LSS spectra. 2014, 1410.4804.
- [50] Wayne Hu. Generalized Slow Roll for Non-Canonical Kinetic Terms. *Phys.Rev.*, D84:027303, 2011, 1104.4500.
- [51] Mark G. Jackson and Koenraad Schalm. Model Independent Signatures of New Physics in the Inflationary Power Spectrum. *Phys.Rev.Lett.*, 108:111301, 2012, 1007.0185.
- [52] Julien Lesgourgues. The Cosmic Linear Anisotropy Solving System (CLASS) I: Overview. 2011, 1104.2932.
- [53] Antony Lewis and Sarah Bridle. Cosmological parameters from CMB and other data: a Monte- Carlo approach. *Phys. Rev.*, D66:103511, 2002, astro-ph/0205436.
- [54] Antony Lewis, Anthony Challinor, and Anthony Lasenby. Efficient computation of CMB anisotropies in closed FRW models. *Astrophys.J.*, 538:473–476, 2000, astro-ph/9911177.
- [55] Andrei D. Linde. A New Inflationary Universe Scenario: A Possible Solution of the Horizon, Flatness, Homogeneity, Isotropy and Primordial Monopole Problems. *Phys.Lett.*, B108:389–393, 1982.
- [56] Jerome Martin and Christophe Ringeval. Superimposed oscillations in the WMAP data? *Phys.Rev.*, D69:083515, 2004, astro-ph/0310382.
- [57] Jerome Martin and L. Sriramkumar. The scalar bi-spectrum in the Starobinsky model: The equilateral case. *JCAP*, 1201:008, 2012, 1109.5838.

- [58] P. D. Meerburg, R. A. M. J. Wijers, and J. P. van der Schaar. WMAP7 constraints on oscillations in the primordial power spectrum. *MNRS*, 421:369–380, March 2012, 1109.5264.
- [59] P. Daniel Meerburg and David N. Spergel. Searching for Oscillations in the Primordial Power Spectrum: Constraints from Planck (Paper II). *Phys.Rev.*, D89:063537, 2014, 1308.3705.
- [60] P. Daniel Meerburg, David N. Spergel, and Benjamin D. Wandelt. Searching for Oscillations in the Primordial Power Spectrum: Perturbative Approach (Paper I). *Phys.Rev.*, D89:063536, 2014, 1308.3704.
- [61] Pieter Daniel Meerburg, Jan Pieter van der Schaar, and Pier Stefano Corasaniti. Signatures of Initial State Modifications on Bispectrum Statistics. *JCAP*, 0905:018, 2009, 0901.4044.
- [62] Vinicius Miranda and Wayne Hu. Inflationary Steps in the Planck Data. *Phys.Rev.*, D89:083529, 2014, 1312.0946.
- [63] Vinicius Miranda, Wayne Hu, and Peter Adshead. Warp Features in DBI Inflation. *Phys.Rev.*, D86:063529, 2012, 1207.2186.
- [64] Masahiro Nakashima, Ryo Saito, Yu-ichi Takamizu, and Jun’ichi Yokoyama. The effect of varying sound velocity on primordial curvature perturbations. *Prog.Theor.Phys.*, 125:1035–1052, 2011, 1009.4394.
- [65] Toshifumi Noumi and Masahide Yamaguchi. Primordial spectra from sudden turning trajectory. *JCAP*, 1312:038, 2013, 1307.7110.
- [66] Minjoon Park and Lorenzo Sorbo. Sudden variations in the speed of sound during inflation: features in the power spectrum and bispectrum. *Phys.Rev.*, D85:083520, 2012, 1201.2903.
- [67] Hiranya Peiris, Richard Easther, and Raphael Flauger. Constraining Monodromy Inflation. *JCAP*, 1309:018, 2013, 1303.2616.
- [68] Raquel H. Ribeiro. Inflationary signatures of single-field models beyond slow-roll. *JCAP*, 1205:037, 2012, 1202.4453.
- [69] Ryo Saito and Yu-ichi Takamizu. Localized Features in Non-Gaussianity from Heavy Physics. *JCAP*, 1306:031, 2013, 1303.3839.
- [70] K. Sato. First Order Phase Transition of a Vacuum and Expansion of the Universe. *Mon.Not.Roy.Astron.Soc.*, 195:467–479, 1981.
- [71] Alexei A. Starobinsky. Relict Gravitation Radiation Spectrum and Initial State of the Universe. (In Russian). *JETP Lett.*, 30:682–685, 1979.

- [72] Alexei A. Starobinsky. Dynamics of Phase Transition in the New Inflationary Universe Scenario and Generation of Perturbations. *Phys.Lett.*, B117:175–178, 1982.
- [73] Alexei A. Starobinsky. Spectrum of adiabatic perturbations in the universe when there are singularities in the inflation potential. *JETP Lett.*, 55:489–494, 1992.
- [74] Ewan D. Stewart. The Spectrum of density perturbations produced during inflation to leading order in a general slow roll approximation. *Phys.Rev.*, D65:103508, 2002, astro-ph/0110322.
- [75] Yu-ichi Takamizu, Shinji Mukohyama, Misao Sasaki, and Yoshiharu Tanaka. Non-Gaussianity of superhorizon curvature perturbations beyond δN formalism. *JCAP*, 1006:019, 2010, 1004.1870.
- [76] Licia Verde. Statistical methods in cosmology. *Lect.Notes Phys.*, 800:147–177, 2010, 0911.3105.
- [77] Li-Min Wang and Marc Kamionkowski. The Cosmic microwave background bispectrum and inflation. *Phys.Rev.*, D61:063504, 2000, astro-ph/9907431.

Chapter 3

Adding Large Scale Structure data into the search

Foreword

This chapter is based on the e-print (submitted to *Physical Review D*)

Searching for primordial localized features with CMB and LSS spectra

Bin Hu, Jesús Torrado

Submitted to Physical Review D

Preprint in arXiv:1410.4804 [astro-ph.CO]

The results presented in it and reproduced here are the product of the combined effort of all its authors, who, as is customary in Theoretical Cosmology, appear in alphabetical order. In this short chapter, I reproduce a major part of the original publication, omitting the introductory content which has already been presented in the previous chapters.

Abstract

Inspired by the study of mild transient reductions in the speed of sound of the adiabatic mode during inflation, we search for a primordial localized feature imprinted in cosmic microwave background and large-scale structure formation observables. We find some common oscillatory patterns both in the Planck CMB temperature power spectrum and the WiggleZ galaxy spectrum. By performing independent searches with these two data sets, we find a coincidence in the most significant mode previously found by Achúcarro *et al.* 2013 by using only Planck data. Furthermore, the joint data analysis shows that the oscillation frequency of

the feature gets better constrained, and the amplitude marginally deviates from zero, unlike what was observed using only Planck data. Besides the parameter estimation, we also discuss the Bayesian evidence. The addition of WiggleZ data mildly enhances the significance of the best mode found in the Planck data.

3.1 Introduction

As discussed in the last chapter there exist several hints of oscillatory signals in the CMB power spectrum [10, 7] and bispectrum [8]. This motivates a search for such kind of features produced by inflationary scenarios beyond canonical single-field.¹ A short review of the literature on those attempts can be seen in the Introduction of the last chapter. In none of those cases the statistical significance of the extended models has been found to be high enough to claim a detection, with the improvement of experimental accuracy we are now at the threshold of verifying or falsifying these models.

In this thesis we focus on searching for oscillatory features in the scenario of a transient reduction in the speed of sound, reviewed in section 1.3.4. Our test case, introduced in the last chapter (and in [2]), consists of a gaussian reduction in the speed of sound occurring within the window of e -folds corresponding to the angular scales probed by CMB and large-scale structure (LSS) surveys. Its functional form is consistent with a reduction in the speed of sound resulting from a soft turn along the inflationary trajectory in a multi-field theory in which the mass hierarchy is large enough to allow for an effective single-field description [4, 3, 12, 5] (though one should keep in mind that a similar reduction in the speed of sound may result from a different high-energy completion of the effective field theory).

Since it is the same curvature perturbations that set the initial conditions for CMB anisotropies and large-scale structure distributions, the primordial oscillatory signals should be imprinted in all the observables of CMB anisotropy and LSS tracers, like CMB spectra, bispectra, galaxy spectra, etc. Based on this consideration, in this chapter and in the original publication [17] we search for primordial oscillatory features from a transient reduction in the speed of sound of adiabatic curvature perturbations via both CMB anisotropy temperature spectrum of the Planck satellite as well as galaxy distribution spectrum of the WiggleZ telescope. The rest of this chapter is organised as follows. In sec. 3.2, we will briefly review the theoretical set-up. In sec. 3.3, we will introduce the methodology of parameter estimation and model selection which is adopted in this work as well as the data sets used. Then, we arrive at our results and discuss them in sec. 3.4. Finally, we conclude in sec. 3.5.

¹By canonical single-field we mean slow-roll regime, Bunch-Davies vacuum, canonical kinetic terms and minimal coupling to gravity, with speed of sound $c_s = 1$.

3.2 Review of the model

In this chapter and the original publication [17], we search for localised features due to a transient reduction in the speed of sound of the adiabatic mode during inflation (see sec. 1.3.4) parametrised as a gaussian in e -folds. The shape tested here is the same previously tested against Planck CMB data only, and it is described in detail in section 2.2 in the last chapter, together with the allowed ranges of its parameters. Very briefly, the resulting feature in the primordial spectrum is

$$\frac{\Delta\mathcal{P}}{\mathcal{P}}(k) = k \int_{-\infty}^0 d\tau u(\tau) \sin(2k\tau) , \quad (3.1)$$

where the reduction in the speed of sound is parametrised as

$$u = 1 - c_s^{-2} = B e^{-\beta(N-N_0)^2} = B e^{-\beta\left(\ln\frac{\tau}{\tau_0}\right)^2} . \quad (3.2)$$

The parameters of the feature: the amplitude $B < 0$, the sharpness $\beta > 0$, and the instant of maximal reduction N_0 (or $\tau_0 < 0$) fall within the region

$$\mathcal{O}(\epsilon, \eta) \ll |B| \ll 1 , \quad (3.3a)$$

$$\frac{50}{N_{\text{CMB}}^2} < \beta \ll \frac{2e}{B^2} , \quad (3.3b)$$

$$4.3 \leq \ln(-\tau_0) \leq 6.0 . \quad (3.3c)$$

For the precise meaning of the quantities that appear here, see sec. 2.2.

3.3 Methodology and data sets

In this work we solve the Einstein-Boltzmann hierarchy by using CAMB [20] and sample the parameter space using different approaches in order to fulfil two different purposes. On one hand, for parameter estimation, we use the thermodynamic Markov chain Monte Carlo (MCMC) sampler, COSMOMC [19]. In detail, we use a Metropolis-Hastings algorithm to generate chains of samples for a set of cosmological parameters. On the other hand, for Bayesian evidence computation and model selection, we adopt the multi-modal nested sampler, MULTINEST [15, 16, 14] which implements an extended form of the nested sampling algorithm [28, 27, 22, 21, 26]. This is because the dependence of the evidence on the prior requires that the prior space is adequately sampled, even in the regions of low likelihood. This makes evidence evaluation at least an order of magnitude more costly than parameter estimation.

In what follows we make a brief review of the concepts of evidence and Bayesian ratio. The Bayesian ratio is defined as the ratio of the probabilities of each of the

two models being the true one underlying a given a set of data \mathbf{D} :

$$R = \frac{P(M_1|\mathbf{D})}{P(M_0|\mathbf{D})} = \frac{\mathcal{Z}_1 P(M_1)}{\mathcal{Z}_0 P(M_0)} = \frac{\mathcal{Z}_1}{\mathcal{Z}_0}. \quad (3.4)$$

Here, $P(M_1)/P(M_0)$ is the probability ratio for the two models *a priori*, which is conventionally set to unity; the *evidence* \mathcal{Z} of a model M is the marginalised likelihood of the data, i.e. the probability of having obtained the data \mathbf{D} integrated over all possible values of the model parameters $\boldsymbol{\theta}$:

$$\mathcal{Z} = \int \mathcal{L}(\mathbf{D}|M(\boldsymbol{\theta})) \pi(\boldsymbol{\theta}) d^D \boldsymbol{\theta}, \quad (3.5)$$

where $\mathcal{L}(\mathbf{D}|M(\boldsymbol{\theta}))$, $\pi(\boldsymbol{\theta})$ and D are, respectively, the likelihood of the data, the prior of the parameters in the model and the dimensionality of the parameter space. In this work, we will use M_1 and M_0 to denote the feature and featureless Λ CDM models; the cosmological parameter ranges we studied are listed in table 3.1. And the multidimensional integration in eq. (3.5) was sampled via the multi-modal implementation of the nested sampling algorithm MULTINEST [15, 16, 14].

Parameter	Range (min, max)
$\Omega_b h^2$	(0.005, 0.100)
$\Omega_c h^2$	(0.01, 0.99)
$100\vartheta_*$	(0.5, 10.0)
τ_{reio}	(0.01, 0.80)
n_s	(0.9, 1.1)
$\ln(10^{10} A_s^2)$	(2.7, 4.0)
B	(-0.2, 0)
$\ln \beta$	(0, 7.5)
$\ln(-\tau_0)$	(4.3, 6.0)

Table 3.1: List of the parameters used in the multi-modal nested sampling. Besides these parameters, we also sample and marginalise over the fourteen nuisance parameters of the Planck likelihood and one bias parameter of the WiggleZ likelihood. We have sampled B up to -0.5 , but nothing interesting was found beyond the upper value cited in this table.

The Bayesian evidence measures the predictivity of a model: the integral in eq. (3.5) is bigger the more amount of likelihood mass falls inside the regions with substantial prior probability, and also the smaller is the volume \mathcal{V} of the parameter space allowed by the theory, since the prior distribution goes roughly like $\pi \sim \mathcal{V}^{-1}$. In turn, the Bayesian ratio quantifies the relative predictivity of two models given a data set: if its value is much smaller than one, the model M_0 is a more likely explanation of the data than the model M_1 , and vice versa. In the

frequentist approach, this is comparable to the increase of p -values² due to the *look-elsewhere effect*. For example, in particle physics, if one allows the predicted mass of a particle to vary within a broad range, the p -value of an apparent peak in particle production with a corresponding mass within this range will increase, just because a wider range of energies makes a random, non-physical peak-like feature more likely. Correspondingly, this indicates that the evidence of this model with a new parameter, like the new particle’s mass, gets reduced.

On the other hand, the Bayesian ratio can also be used as an indicator of the correlation between two data sets with respect to an extended model M_1 based on a simpler model M_0 : if the predictivity of the extended model with respect to the basis model increases when adding the new data set, this is an indication of the regions of high probability in the likelihood of the extended model being similar in the two data sets. Otherwise, the product of the likelihoods of both data sets would amount to a smaller evidence ratio than that of the single data sets.

As for the data sets, we use the measurements of CMB temperature anisotropy³ [9] from the first data release of the Planck survey. Its temperature power-spectrum likelihood is divided into low- ℓ ($\ell < 50$) and high- ℓ ($\ell \geq 50$) parts (see sec. 1.5.4). In order to break the well-known parameter degeneracy between the reionisation optical depth τ_{reio} and the scalar index n_s , the low- ℓ WMAP polarisation likelihood (WP) is used [9]. Finally, the unresolved foregrounds are marginalised over, assuming wide priors on the relevant nuisance parameters as described in [6].

Since several interesting feature modes are hinted at by using only Planck temperature spectrum (see chapter 2 or [2]), a natural step is to cross check these results with other observables seeded by the same initial conditions, coming from different experiments whose systematic uncertainties are different from Planck’s. We use the measurements of the galaxy power spectrum made by the WiggleZ Dark Energy Survey.⁴ As described in [24], we use the power spectrum measured from spectroscopic redshifts of 170 352 blue emission line galaxies over a volume of $\sim 1 \text{ Gpc}^3$ [13]. The covariance matrices as given in [24] are computed using the method described by [11]. The best model proposed for non-linear corrections to the matter power spectrum was calibrated against simulations. It has already been demonstrated that linear theory predictions are as good a fit to the data as the calibrated model up to $k \sim 0.2 h/\text{Mpc}$ [24, 25]. For these reasons we restrict ourselves to scales smaller than $k_{\text{max}} = 0.2 h/\text{Mpc}$ and use the linear theory prediction only. We also marginalise over a linear galaxy bias for each of the four

²From Wikipedia.org, a p -value is the probability of obtaining a test statistic result at least as extreme as the one that was actually observed, assuming that the null hypothesis is true. A researcher will often “reject the null hypothesis” when the p -value turns out to be less than a predetermined significance level, often 0.05 or 0.01. Such a result indicates that the observed result would be highly unlikely under the null hypothesis.

³<http://pla.esac.esa.int/pla/aio/planckProducts.html>

⁴<http://smp.uq.edu.au/wigglez-data>

redshift bins.

3.4 Results and discussion

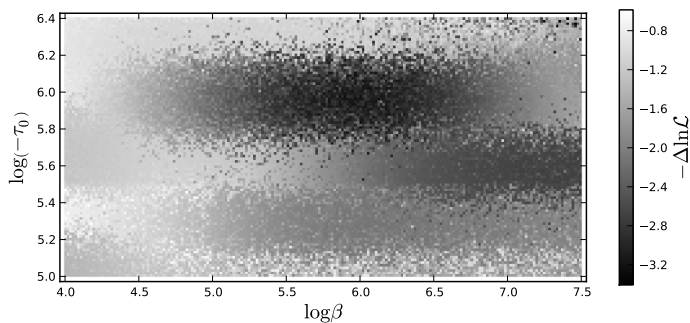
In order to justify or falsify this model, we should go beyond CMB observables from the Planck satellite. A feature in the primordial spectrum of density perturbations will seed both CMB anisotropies and the tracers of matter perturbation, such as the galaxy distribution. Thus, if those features are big enough we should observe them via all those windows.

Based on the findings of the previous study with Planck temperature power spectrum (see chapter 2 and [2, 1]), we sample the same region of the parameter space using *only* the galaxy power spectrum from the WiggleZ Dark Energy Survey. The result is shown in fig. 3.1(a). In particular we show the profile likelihood of the sample in the plane $(\ln \beta, -\ln(-\tau_0))$. The upper limit of $\ln(-\tau_0)$ has been slightly extended, and the lower one slightly shrunk, in order to limit the interval to the region in which the improvement in the likelihood is significant (but we will later restore the limits of chapter 2 in the evidence computation).

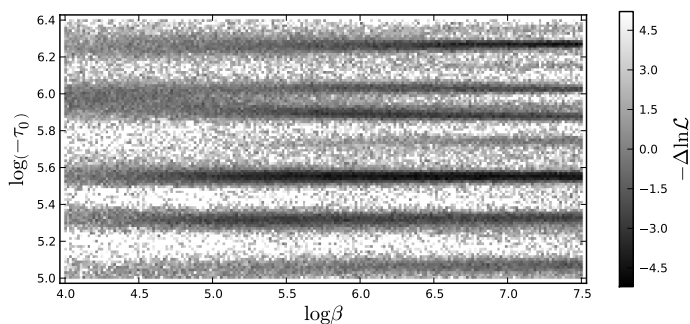
As we can see, in the WiggleZ posterior there exist three diffused modes. In particular, comparing figs. 3.1(a) and 3.1(b) with the naked eye there seems to exist a coincidence between WiggleZ and Planck results around $\ln(-\tau_0) \sim 6.0$, $\ln(-\tau_0) \sim 5.55$ and $\ln(-\tau_0) \sim 5.3$, which were three of the most significant modes detected in the previous work [2], named respectively modes \mathcal{A} , \mathcal{B} and \mathcal{C} (see table 2.1). In order to test such coincidence, we repeated the search combining both data sets. The results are reported in fig. 3.1(c). The well-isolated modes previously found in the Planck data are accurately reproduced (compare figs. 3.1(b) and 3.1(c), and also see fig. 3.2(a)). In addition we observe an unfolding of mode \mathcal{A} and a new mode at $\ln(-\tau_0) \sim 6.3$ which survives the addition of the WiggleZ data; both of them will be the subject of future work. We have checked that there exists an enhancement of more than 20% in the value of the likelihood improvement ($\Delta \ln \mathcal{L}$) in modes \mathcal{B} and \mathcal{C} , while that of mode \mathcal{A} shows no enhancement.

Later, we isolated and re-sampled using MCMC methods each of the four individual modes found in [2] (see fig. 3.2) with the joint data sets. The corresponding results are shown in the fig. 3.2(a). We can see that the individual modes are separated quite well in the $\ln(-\tau_0)$ direction.

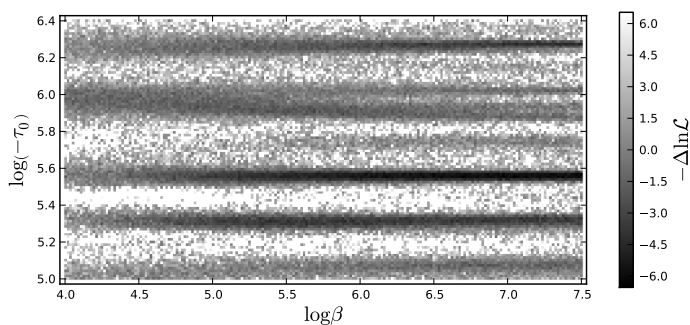
If we force ourselves to focus on one particular mode, such as mode \mathcal{B} , we can obtain quite stringent constraints on the feature parameters, like those demonstrated in chapter 2, e.g. in table 2.1 or fig. 2.6. However, finding stringent constraints does not mean that this result has a very strong statistical significance, because the parameter space volume of the feature model is much larger than that of the *vanilla* Λ CDM model. So, even if there exists a local patch in the parameter space with highly peaked likelihood, the evidence of this signature could still be suppressed greatly by the big volume of the extra parameter space,



(a) WiggleZ



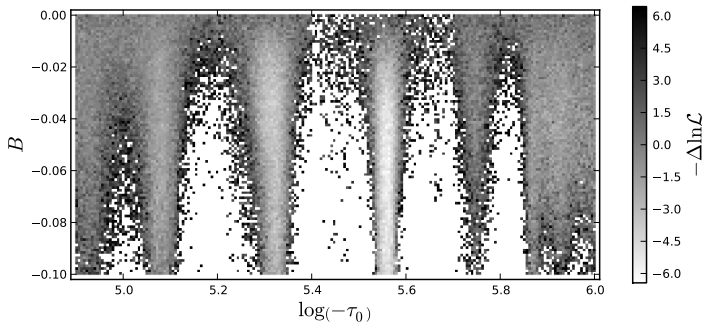
(b) Planck



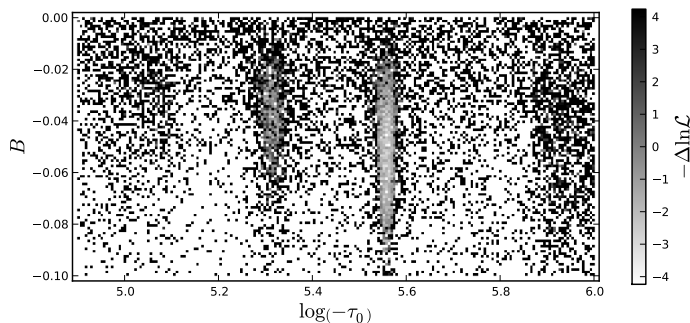
(c) Planck+WiggleZ

Figure 3.1: Profile parameter distribution of the MCMC sampling in the $(\ln \beta, -\ln(-\tau_0))$ plane, for the different combinations of data sets. It shows the coincidence between the fits found in Planck and WiggleZ at $\ln(-\tau_0) \sim 5.3$ and $\ln(-\tau_0) \sim 5.55$, and their enhancement of 20% in likelihood improvement. The difference in the likelihood (Δ) is calculated against the best fit value of Λ CDM in the different data sets. The regions where there is no significant improvement over the best fit of the Λ CDM model are not shown.

as discussed in the previous section.



(a) MCMC sampling



(b) Multi-modal nested sampling

Figure 3.2: Profile likelihood in the $(\ln(-\tau_0), B)$ plane for Planck+WiggleZ, for the different sampling methods. It demonstrates how the multi-modal nested sampling algorithm samples more thoroughly the regions of low likelihood. The regions not samples are shown in white (in the B&W version, not to be confused with the light grey areas of high likelihood). The difference in the likelihood (Δ) is calculated against the best fit value of Λ CDM in the different data sets.

Inspired by the fact that there exists a relatively significant reduction in the likelihood value of the feature model in the best fits compared with that of the featureless Λ CDM model, (e.g. for mode B the joint data analysis gives $-2\Delta \ln \mathcal{L} \sim 10$), we are motivated to compute the Bayesian ratio of the feature model. The statistical results are summarised in table 3.2, fig. 3.2(b) and fig. 3.3.

A comparison between the results of the MCMC and multi-modal nested samplings, showing the consistency between them, can be seen in fig. 3.2. The main difference between both sub-plots is due to the more thorough sampling of the tails of the distribution (points in parameter space with low likelihood value)

Model	Data set	$-2 \ln \mathcal{L}$	$\ln \mathcal{Z}$	R
M_1	Planck	9801.918 (9796.27)	-4955.61 ± 0.31	$\exp(0.46) \simeq 1.6$
M_0	Planck	9807.154 (9805.90)	-4956.07 ± 0.31	
M_1	Planck+WiggleZ	10253.570 (10249.20)	-5183.05 ± 0.32	$\exp(0.62) \simeq 1.9$
M_0	Planck+WiggleZ	10262.042 (10258.80)	-5183.67 ± 0.31	

Table 3.2: Multi-modal nested sampling results of feature (M_1) and non-feature (M_0) models with the different data sets. The likelihood values in the third column are given at the best fit, first the nested sampling value, and second, in parenthesis, the MCMC sampling value.

achieved by multi-modal nested sampling: these points are crucial to get a reliable evidence estimation, which is the goal of the nested-sampling algorithms, but almost irrelevant to parameter estimation, at which MCMC excel. In table 3.2, we can see that the resulting best-fit likelihood values from multi-modal nested sampling are also consistent with those coming from MCMC sampling, though, as expected, the former a little bit lower than the latter, since the sampling around the maxima is more thorough in MCMC's.

In the first place, the Bayesian ratios listed in table 3.2 tell us that, taking into account only the part of the parameter space described in sec. 2.2, there would apparently exist a slightly positive preference for the feature model: $R \sim 1.9$ (Planck + WiggleZ) vs. 1.6 (Planck) (though, according to the conventional criterion [18] it is *barely worth mentioning*). We must emphasise that in this paper we did not cover all the parameter regime allowed by theory, which sets no lower bound for τ_0 , but instead the regime in which the features are most likely to be detectable by Planck. Despite the expected corrections, the slightly favourable value of the Bayesian evidence in the observable regime makes us optimistic about the enlargement of the parameter space and the addition of new data sets, namely Planck's polarisation power spectrum and bispectrum. This optimism is also backed up by how, as discussed in the sec. 3.3, the increase in the Bayesian ratio when adding the WiggleZ data indicates a positive correlation between the features found in both data sets; nevertheless, when put into the context of the error bars for the evidences cited in table 3.2, the claim gets milder.

Also, on the positive side, as can be seen in fig. 3.3, the addition of the WiggleZ data set clearly pushes the marginalised distribution towards bigger amplitudes of the feature with respect to using Planck data only, which on the one hand is an indication of a positive correlation between the sets, and on the other hand reinforces the overall likelihood of the presence of a feature against the null hypothesis.

3.5 Conclusions and outlook

In this chapter we searched for primordial oscillatory signals inspired by a transient reduction in the sound speed of the adiabatic curvature perturbation via

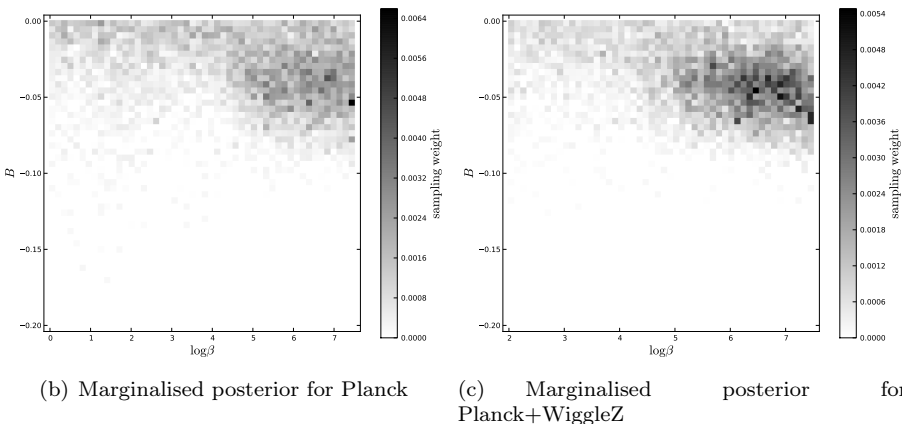
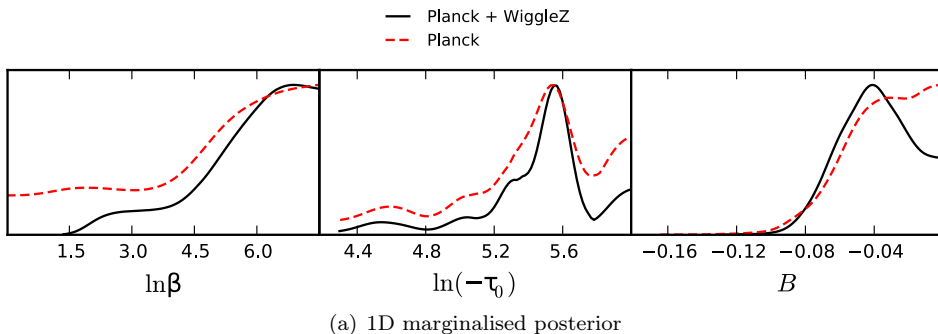


Figure 3.3: Multi-modal nested sampling results: 1D marginalised posterior distribution for the feature parameters and 2D marginalised posterior distribution in the plane $(\ln \beta, B)$, with and without the WiggleZ data set. Notice how the addition of the WiggleZ data set increases the overall likelihood of a feature with a non-zero amplitude.

CMB (Planck) and LSS (WiggleZ) windows. First of all, by analysing both data sets separately, we found some common oscillatory patterns both in the Planck CMB temperature power spectrum and the WiggleZ galaxy spectrum. Interestingly, we found a coincidence in the most significant mode previously found by Achúcarro *et al.* 2013 [2] by using only Planck data. Second, the joint data analysis showed that the oscillation frequency of the feature gets better constrained, and the amplitude marginally deviates from zero, unlike what was observed by using only Planck data. Besides parameter estimation, we also calculated the Bayesian evidence for the purpose of model selection by using multi-modal nested sampling. For a full model selection study, the prior must be extended and sampled in the full parameter range allowed by the theory. Our results show that,

if we were to ignore the parts of the parameter space not sampled here, there would exist a slightly positive preference for the feature model, Bayesian factor $R \sim 1.9$ (Planck + WiggleZ), vs. 1.6 (Planck). Therefore, we are optimistic about enlarging the sampled parameter range and using additional data sets, specially Planck's polarisation power spectra and temperature bispectrum.

The Bayesian evidence analysis shows that although there exists a relatively large improvement in the likelihood value ($-2\Delta \ln \mathcal{L} \sim 10$) in several particular parameter regimes, due to the relatively large number of extra parameters (3) and their broad ranges of variation (look-elsewhere effect), the present Planck temperature and WiggleZ matter power spectra data still lack significance to claim a detection. However, due to the correlations between temperature and polarisation modes of the power spectrum and the correlations with the bispectra given by the model of transient reductions in the speed of sound, the present results have specific *predictions* for the TE cross-correlation spectrum (C_ℓ^{TE}) [1] and the temperature bispectrum ($B_{\ell_1 \ell_2 \ell_3}^{\text{TTT}}$) [2, 1] which can be detected with the upcoming Planck data release 2014. Particularly, the new fast bispectrum estimator of oscillatory features from [23] should be able to cover the frequency where the most significant mode that we found is located.

In the light of the additional WiggleZ data, we update the predictions stated in chapter 2 and [2, 1], based on the high correlation between the bispectrum features studied there and the phenomenological oscillatory shape tested by the Planck collaboration and given in [8, eq. (16)].⁵ In the parameters used by the Planck collaboration, we expect to find a feature with zero phase, and wavelength in the 95% c.l. interval $k_c \in (0.0078, 0.0083)$ from mode \mathcal{B} , or $k_c \in (0.0099, 0.0110)$ from mode \mathcal{C} . As happened when using only Planck data [1], a degeneracy between B and $\ln \beta$ prevents us from setting accurate predictions for the amplitude and envelope of the feature. Nevertheless, for all values of the parameters along the degeneracy, the signal is most significant on the scales beyond the second acoustic peak, and reaches its maximum around the third or fourth peak.

Bibliography

- [1] Ana Achúcarro, Vicente Atal, Bin Hu, Pablo Ortiz, and Jesus Torrado. Inflation with moderately sharp features in the speed of sound: GSR and in-in formalism for power spectrum and bispectrum. *Phys.Rev.*, D90:023511, 2014, 1404.7522.
- [2] Ana Achúcarro, Vicente Atal, Pablo Ortiz, and Jesus Torrado. Localized correlated features in the CMB power spectrum and primordial bispectrum from a transient reduction in the speed of sound. *Phys.Rev.*, D89:103006, 2014, 1311.2552.

⁵For every combination of the feature parameter values in the regions of high likelihood, one can find a combination of the parameters in [8] (including a gaussian envelope as described there) such that the correlation between both shapes at the primordial level is at least 95%.

- [3] Ana Achucarro, Jinn-Ouk Gong, Sjoerd Hardeman, Gonzalo A. Palma, and Subodh P. Patil. Features of heavy physics in the CMB power spectrum. *JCAP*, 1101:030, 2011, 1010.3693.
- [4] Ana Achucarro, Jinn-Ouk Gong, Sjoerd Hardeman, Gonzalo A. Palma, and Subodh P. Patil. Mass hierarchies and non-decoupling in multi-scalar field dynamics. *Phys.Rev.*, D84:043502, 2011, 1005.3848.
- [5] Ana Achucarro, Jinn-Ouk Gong, Sjoerd Hardeman, Gonzalo A. Palma, and Subodh P. Patil. Effective theories of single field inflation when heavy fields matter. *JHEP*, 1205:066, 2012, 1201.6342.
- [6] P.A.R. Ade et al. Planck 2013 results. XV. CMB power spectra and likelihood. 2013, 1303.5075.
- [7] P.A.R. Ade et al. Planck 2013 results. XXII. Constraints on inflation. 2013, 1303.5082.
- [8] P.A.R. Ade et al. Planck 2013 Results. XXIV. Constraints on primordial non-Gaussianity. 2013, 1303.5084.
- [9] P.A.R. Ade et al. Planck 2013 results. XVI. Cosmological parameters. *Astron.Astrophys.*, 2014, 1303.5076.
- [10] C.L. Bennett et al. Nine-Year Wilkinson Microwave Anisotropy Probe (WMAP) Observations: Final Maps and Results. *Astrophys.J.Suppl.*, 208:20, 2013, 1212.5225.
- [11] C. Blake, S. Brough, M. Colless, W. Couch, S. Croom, T. Davis, M. J. Drinkwater, K. Forster, K. Glazebrook, B. Jelliffe, R. J. Jurek, I.-H. Li, B. Madore, C. Martin, K. Pimbblet, G. B. Poole, M. Pracy, R. Sharp, E. Wisnioski, D. Woods, and T. Wyder. The WiggleZ Dark Energy Survey: the selection function and $z = 0.6$ galaxy power spectrum. *MNRAS*, 406:803–821, August 2010, 1003.5721.
- [12] Sebastian Cespedes, Vicente Atal, and Gonzalo A. Palma. On the importance of heavy fields during inflation. *JCAP*, 1205:008, 2012, 1201.4848.
- [13] M. J. Drinkwater, R. J. Jurek, C. Blake, D. Woods, K. A. Pimbblet, K. Glazebrook, R. Sharp, M. B. Pracy, S. Brough, M. Colless, W. J. Couch, S. M. Croom, T. M. Davis, D. Forbes, K. Forster, D. G. Gilbank, M. Gladders, B. Jelliffe, N. Jones, I.-H. Li, B. Madore, D. C. Martin, G. B. Poole, T. Small, E. Wisnioski, T. Wyder, and H. K. C. Yee. The WiggleZ Dark Energy Survey: survey design and first data release. *MNRAS*, 401:1429–1452, January 2010, 0911.4246.
- [14] F. Feroz, M. P. Hobson, E. Cameron, and A. N. Pettitt. Importance Nested Sampling and the MultiNest Algorithm. *ArXiv e-prints*, June 2013, 1306.2144.

- [15] F. Feroz, M.P. Hobson, and M. Bridges. MultiNest: an efficient and robust Bayesian inference tool for cosmology and particle physics. *Mon.Not.Roy.Astron.Soc.*, 398:1601–1614, 2009, 0809.3437.
- [16] Farhan Feroz and M.P. Hobson. Multimodal nested sampling: an efficient and robust alternative to MCMC methods for astronomical data analysis. *Mon.Not.Roy.Astron.Soc.*, 384:449, 2008, 0704.3704.
- [17] Bin Hu and Jesús Torrado. Searching for primordial localized features with CMB and LSS spectra. 2014, 1410.4804.
- [18] S.H. Jeffreys. *The Theory of Probability*. Oxford University Press, 1961.
- [19] Antony Lewis and Sarah Bridle. Cosmological parameters from CMB and other data: a Monte- Carlo approach. *Phys. Rev.*, D66:103511, 2002, astro-ph/0205436.
- [20] Antony Lewis, Anthony Challinor, and Anthony Lasenby. Efficient computation of CMB anisotropies in closed FRW models. *Astrophys.J.*, 538:473–476, 2000, astro-ph/9911177.
- [21] Andrew R Liddle. Information criteria for astrophysical model selection. *Mon.Not.Roy.Astron.Soc.*, 377:L74–L78, 2007, astro-ph/0701113.
- [22] Pia Mukherjee, David Parkinson, and Andrew R. Liddle. A nested sampling algorithm for cosmological model selection. *Astrophys.J.*, 638:L51–L54, 2006, astro-ph/0508461.
- [23] M. Münchmeyer, F. Bouchet, M. Jackson, and B. Wandelt. The Komatsu Spergel Wandelt estimator for oscillations in the cosmic microwave background bispectrum. 2014, 1405.2550.
- [24] D. Parkinson, S. Riemer-Sørensen, C. Blake, G. B. Poole, T. M. Davis, S. Brough, M. Colless, C. Contreras, W. Couch, S. Croom, D. Croton, M. J. Drinkwater, K. Forster, D. Gilbank, M. Gladders, K. Glazebrook, B. Jelliffe, R. J. Jurek, I.-h. Li, B. Madore, D. C. Martin, K. Pimblet, M. Pracy, R. Sharp, E. Wisnioski, D. Woods, T. K. Wyder, and H. K. C. Yee. The WiggleZ Dark Energy Survey: Final data release and cosmological results. *Phys.Rev.*, D86(10):103518, November 2012, 1210.2130.
- [25] Signe Riemer-Sørensen, David Parkinson, and Tamara M. Davis. Combining Planck with Large Scale Structure gives strong neutrino mass constraint. 2013, 1306.4153.
- [26] R. Shaw, Michael Bridges, and M.P. Hobson. Clustered nested sampling: Efficient Bayesian inference for cosmology. *Mon.Not.Roy.Astron.Soc.*, 378:1365–1370, 2007, astro-ph/0701867.

3.5 Bibliography

- [27] Skilling Sivia D. *Data Analysis; a Bayesian tutorial*. Oxford University Press, 2006.
- [28] John Skilling. Nested sampling. *AIP Conference Proceedings*, 735(1):395–405, 2004.

Chapter 4

Peer-reviewed and published cosmological code

4.1 Introduction

In this chapter we describe some pieces of code which were developed in order to be able to tackle some of the problems presented in the previous chapters, and to prepare the tools for future research.

Calculating is a fundamental part of Theoretical Physics research. The very act of carrying out the algebraic or numeric integral of a 2-loop process is arguably not Physics *per se* – as some of my professors would say, it is just cranking the *mathematical coffee mill*. Physics is to be found in the motivation of the problem, in the choice of the integration method, in the approximations made and those deliberately not made, in the method used to test the result, and in the interpretation of it in the context of the theory.

Together with algebraic calculations, computer-assisted calculations are essential in Theoretical Physics, specially when heavy numerical computations, randomisation or simulations are involved. The challenge in this cases is often carrying out the calculations in a manageable amount of time, controlling all possible errors.

Creating the tools for computer-assisted calculations, *programming* or *coding*, *is* Physics research in the same way as algebraic calculations are: Physics is in the choice of the algorithms, the approximations, the means to control the errors, the interpretation of the result... all that based on the nature of the problem and its physical context.

In order to carry out the research presented in this thesis, and also in order to facilitate similar research by our peers, we created a small number of tools that have been published under an open source license as an integral part of two Cosmological codes, CLASS and MONTE PYTHON, having previously been

reviewed by the authors of the respective codes. In the next sections we describe them briefly.

4.2 Arbitrary Primordial Power Spectrum for CLASS

In chapter 2, we have attempted to fit a modified shape of the slow-roll, single field primordial power spectrum to the Planck CMB data. In order to accomplish that, we needed to integrate into a cosmological code the ability to start from an arbitrary primordial power spectrum. It would be desirable for the primordial power spectrum to be at the same time (1) calculated on-the-fly from a series of parameters, (2) easily modified without the need to maintain many different compiled versions of the cosmological code, and (3) the relevant parameters should be easily handled by a Monte Carlo sampler.

We found those requirements to be satisfied more easily when integrating them into the Boltzmann code CLASS [2], due, among other things, to the cleanness and modularity of its code and the effective support from its authors in implementing the modifications presented here.

With the requirements stated above at hand, we opted for modifying CLASS minimally to allow it to launch an external program and retrieve from it the primordial power spectrum as a table in plain text, from which CLASS creates an internal interpolating function. The external power spectrum generator gets the values of the necessary parameters through CLASS itself, either as defined in a CLASS input file or fed by a Monte Carlo sampler. This way, CLASS does not need to be recompiled when modifying the shape of the primordial power spectrum, and the external generator can be coded in any language that appeals the researcher, following minimum requirements. Even the case of a precomputed table of values of the primordial power spectrum is trivially included, through the use of the `cat` command of UNIX-like systems.

The main disadvantage of this external-program approach, as opposed to hard coding the power spectrum, is the delay inherent to interfacing through plain text. Fortunately, this delay is small compared to the most time-consuming part of the cosmological code: the calculation of the transfer functions.

This modification of CLASS, together with the necessary documentation written by the author of this thesis, was reviewed by one of the authors of CLASS, Julien Lesgourgues, and integrated into the main code and released to the community in CLASS version 2.1, on March 2014.

As a simple example we show here how easy it is to implement an oscillatory feature on top of the primordial scalar power spectrum:

$$\mathcal{P}(k) = \left(A_s \left(\frac{k}{k_0} \right)^{n_s-1} \right) \left(1 + B \sin \left(2\pi \frac{k}{k_l} + \phi \right) \right). \quad (4.1)$$

```

P_k_ini type = external_Pk
command = python external_Pk/generate_Pk_sin.py
custom1 = 0.05 # Pivot scale
custom2 = 2.215e-9 # Amplitude of the power spectrum
custom3 = 0.9624 # Spectral index of the power spectrum
custom4 = 0.0 # Amplitude of the feature
custom5 = 0.002 # Wavelength of the feature
custom6 = 0 # Phase of the feature

# Retrieving the necessary parameters
import sys
k_0 = float(sys.argv[1]) # Pivot scale
A = float(sys.argv[2]) # Amplitude of the power spectrum
n_s = float(sys.argv[3]) # Spectral index of the power spectrum
B = float(sys.argv[4]) # Amplitude of the feature
k_l = float(sys.argv[5]) # Wavelength of the feature
phi = float(sys.argv[6]) # Phase of the feature

# P(k) calculation
from math import exp, sin, pi
def P(k):
    return (A * (k/k_0)**(n_s-1.) *
            (1 + B * sin(2*pi*k/k_l + phi)))

# Limits for k and precision
k_min, k_max = 1.e-6, 0.75
k_per_decade_primordial = 1000.

# Producing the values of P(k)
k = k_min
while k <= k_max:
    print "%.18g_%.18g" % (k, P(k))
    k = k * 10.**(1./float(k_per_decade_primordial))

```

Figure 4.1: **Top:** lines of the CLASS input file defining the use of the oscillatory spectrum. **Bottom:** PYTHON script that generates the spectrum of eq. (4.1).

As we see, the whole spectrum is parametrised by the global amplitude A_s and spectral index n_s , together with the oscillation amplitude B , its wavelength k_l and its phase ϕ . In order for CLASS to use that as a primordial spectrum, it is enough to add to the CLASS input file the lines on the upper box of figure 4.1, where the contents of the file `generate_Pk_sin.py` can be seen in the bottom of the same figure. Such a simple code fulfils all the necessary requirements. The resulting primordial and CMB spectra can be seen in figure 4.2.

4.3 Interfacing of MULTINEST into MONTE PYTHON

Bayesian statistics judges the adequacy of some physical models over others in terms of their predictivity: more predictive models are preferred over less predictive ones. Predictivity of a model is the joint effect of how well it describes the data together with how restricted is its range of predictions. The joint measurement of both aspects is the *Bayesian evidence*, equal to the integral of the

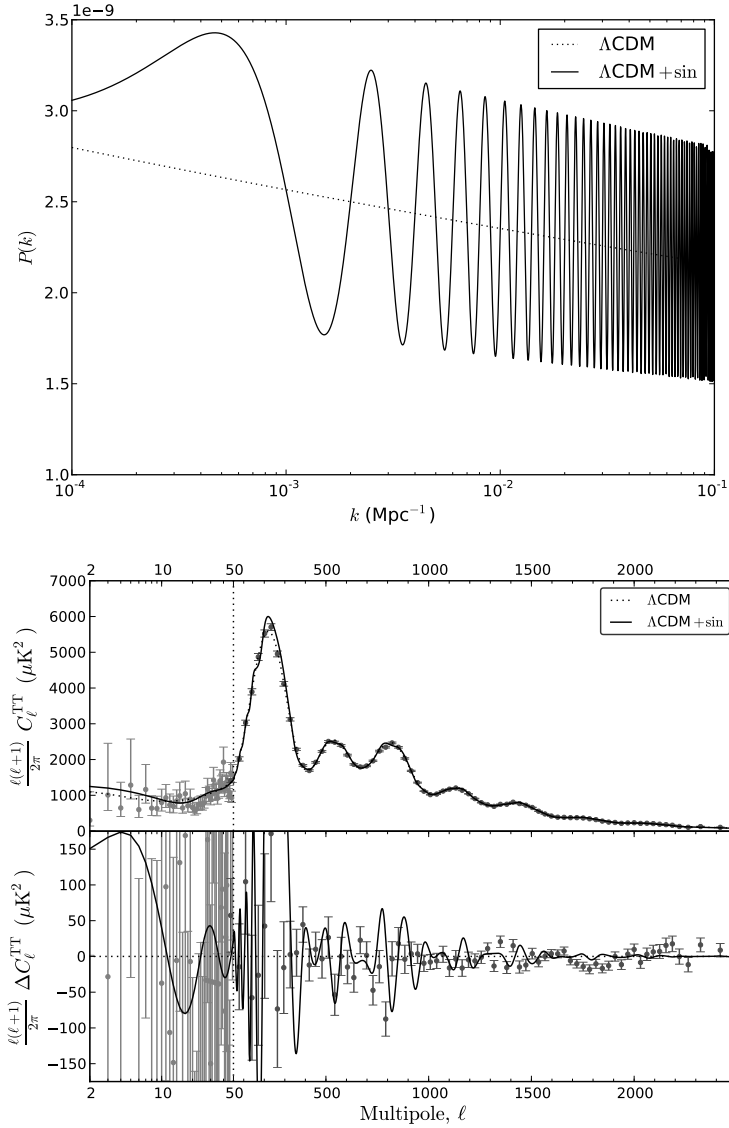


Figure 4.2: **Top:** Primordial scalar power spectrum of eq. (4.1), assuming Planck’s best fit values for A_s and n_s , and some random values for the parameters of the oscillation. **Bottom:** Resulting (lensed) CMB temperature power spectrum.

likelihood and the *prior*:

$$B_{\mathcal{M}} = \int_{\Omega} \mathcal{L}(\mathcal{D}|\mathcal{M}(\omega)) \pi(\omega|\mathcal{M}) d\omega , \quad (4.2)$$

\mathcal{D} being a set of data, and \mathcal{M} a physical model parametrised by the quantities ω , which take values on a set Ω with probability $\pi(\omega|\mathcal{M})$.

Computing the Bayesian evidence is a hard task to accomplish, which in general requires methods different from those used for *parameter inference* (i.e. estimating the parameter values that best fit the data and their distribution around those values). While Markov chain Monte Carlo methods (MCMC) are one efficient method for parameter inference, they fall short when used for computation of the Bayesian evidence, mostly due to their lack of sampling in the areas of the parameter space away from the best fit, which in practice do not affect the confidence intervals of the parameters, but can add up to a significant fraction of the total value of the evidence. An alternative sampling method is needed.

Nested sampling [8] is one of those methods aimed at calculating accurately the Bayesian evidence. Its adequacy arises, on the one hand, from how it samples the parameter space, climbing from the lowest to the highest values of the likelihood allowed by the prior ranges; and, on the other hand, on its slow scaling with the number of dimensions of the parameter space. One particular enhancement over nested sampling is the MULTINEST algorithm [5, 6, 4]. MULTINEST improves on nested sampling by adding an ellipsoidal-decomposition algorithm that allows both for sampling of weirdly-shaped distributions and for simultaneous sampling of multiple *modes*, or regions of high probability, in complicated probability distributions that may contain several of them (this is precisely our case, see chapters 2 and 3). In addition to an accurate calculation of the Bayesian evidence of complicated distributions, MULTINEST is also able to produce a fair sample of the parameter space under the likelihood, that can be used for parameter inference in a similar way as the chains of samples coming from MCMC's.¹

All that makes MULTINEST a very interesting tool for data analysis, which would be desirable to use along the common MCMC methods. In order to do so, we wish to combine MULTINEST with the necessary computational cosmological tools, mainly Boltzmann codes and experimental likelihoods. This is naturally achieved by interfacing MULTINEST through an already established cosmological MCMC sampler, such as COSMOMC [7] or MONTE PYTHON [1]. Since the Boltzmann code used in this thesis was initially mostly CLASS [2], it made sense to create this interface for the companion sampler MONTE PYTHON.

The interface written by the author of this thesis and the main author of MONTE PYTHON, Benjamin Audren, starts from PYMULTINEST, the PYTHON wrapper of MULTINEST written by Johannes Buchner [3], which takes care of the

¹Since the samples of MULTINEST are scarcer, but the sampling is faster, the sample from MULTINEST can also be used to roughly estimate the covariance matrix of the likelihood, and then use it to make more efficient an MCMC, which will characterise the distribution around the minimum more thoroughly – a great idea of Benjamin Audren.

FORTTRAN–PYTHON communication in a neat way. MULTINEST’s input, both physical and sampling parameters, is passed through the standard input methods of MONTE PYTHON (parameter file and command line, respectively), and the output of MULTINEST is simultaneously

- kept unmodified in its raw format in a separate folder for later additional analyses;
- used to create MCMC-like samples in MONTE PYTHON format from the fair samples of MULTINEST, in order to use the same MONTE PYTHON analysis tools. The different modes are separated in different, independent *chain folders*.

In addition, our interface adds the capability, not present in the current version of MULTINEST, of using as *clustering parameters* any combination of them, not necessarily those in the first positions.

This interface, together with the necessary documentation written by the author of this thesis, was integrated into the main code and released to the community with MONTE PYTHON version 2.0, on March 2014.

Together with the interface, we created a simple example likelihood with 3 distinct modes:

$$\mathcal{L}(\mathcal{D} | \mathbf{v}) = \prod_{i=1}^3 \exp \left\{ -\frac{1}{2} (\mathbf{v} - \boldsymbol{\mu}_i) \boldsymbol{\Sigma}_i^{-1} (\mathbf{v} - \boldsymbol{\mu}_i) \right\}, \quad (4.3)$$

where $\mathbf{v} := (H_0, \omega_b, \omega_{\text{CDM}})$ are the parameters of the model and the data \mathcal{D} enters through the central values $\boldsymbol{\mu}_i$ and the covariance matrices $\boldsymbol{\Sigma}_i$:

$$\boldsymbol{\mu}_1 = (67.0, 0.02225, 0.0120), \quad \boldsymbol{\Sigma}_1 = \begin{pmatrix} 0.1 & 2 \cdot 10^{-5} & 2 \cdot 10^{-4} \\ 2 \cdot 10^{-5} & 2 \cdot 10^{-7} & 2.4 \cdot 10^{-7} \\ 2 \cdot 10^{-4} & 2.4 \cdot 10^{-7} & 5 \cdot 10^{-6} \end{pmatrix}, \quad (4.4a)$$

$$\boldsymbol{\mu}_2 = (69.5, 0.02300, 0.0170), \quad \boldsymbol{\Sigma}_2 = \begin{pmatrix} 0.3 & 2 \cdot 10^{-5} & 3.5 \cdot 10^{-4} \\ 2 \cdot 10^{-5} & 1.2 \cdot 10^{-7} & 1.4 \cdot 10^{-7} \\ 3.5 \cdot 10^{-4} & 1.4 \cdot 10^{-7} & 2 \cdot 10^{-6} \end{pmatrix}, \quad (4.4b)$$

$$\boldsymbol{\mu}_3 = (71.5, 0.02180, 0.0100), \quad \boldsymbol{\Sigma}_3 = \begin{pmatrix} 0.2 & 5.5 \cdot 10^{-5} & 3 \cdot 10^{-4} \\ 5.5 \cdot 10^{-5} & 4 \cdot 10^{-7} & 5 \cdot 10^{-7} \\ 3 \cdot 10^{-4} & 5 \cdot 10^{-7} & 5 \cdot 10^{-6} \end{pmatrix}. \quad (4.4c)$$

The result of the sampling of this likelihood using MULTINEST through the interface described in this section is show in fig. 4.3. The dashed lines show the cubic prior regions corresponding to each of the modes, cut automatically by MULTINEST and stored as three different MONTE PYTHON chains.

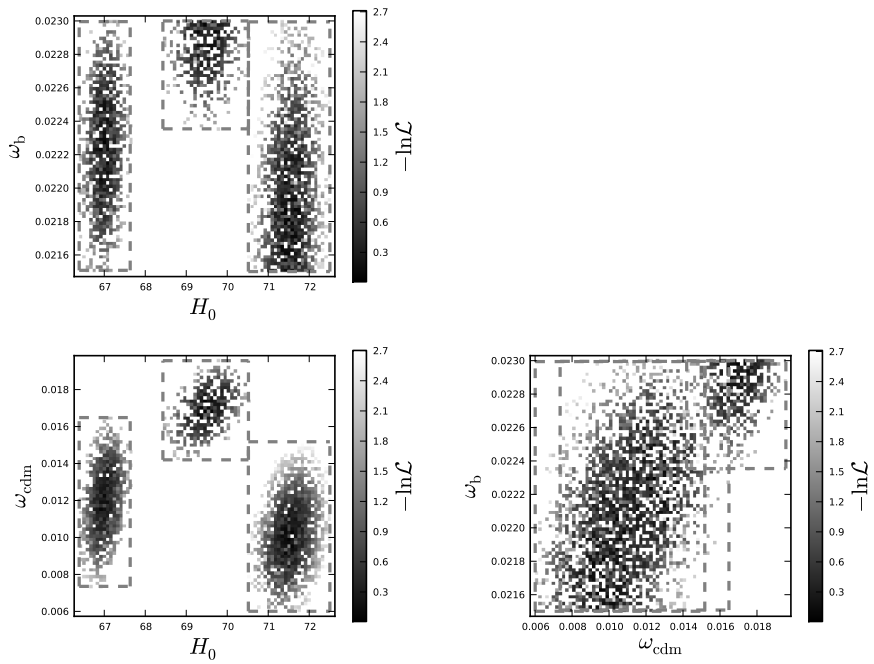


Figure 4.3: Profile of the sampling of the likelihood given by eq. (4.3), using MULTINEST interfaced through MONTE PYTHON.

Bibliography

- [1] Benjamin Audren, Julien Lesgourgues, Karim Benabed, and Simon Prunet. Conservative Constraints on Early Cosmology: an illustration of the Monte Python cosmological parameter inference code. *JCAP*, 1302:001, 2013, 1210.7183.
- [2] Diego Blas, Julien Lesgourgues, and Thomas Tram. The Cosmic Linear Anisotropy Solving System (CLASS) II: Approximation schemes. *JCAP*, 1107:034, 2011, 1104.2933.
- [3] J. Buchner, A. Georgakakis, K. Nandra, L. Hsu, C. Rangel, et al. X-ray spectral modelling of the AGN obscuring region in the CDFS: Bayesian model selection and catalogue. 2014, 1402.0004.
- [4] F. Feroz, M. P. Hobson, E. Cameron, and A. N. Pettitt. Importance Nested Sampling and the MultiNest Algorithm. *ArXiv e-prints*, June 2013, 1306.2144.
- [5] F. Feroz, M.P. Hobson, and M. Bridges. MultiNest: an efficient and robust Bayesian inference tool for cosmology and particle physics. *Mon.Not.Roy.Astron.Soc.*, 398:1601–1614, 2009, 0809.3437.
- [6] Farhan Feroz and M.P. Hobson. Multimodal nested sampling: an efficient and robust alternative to MCMC methods for astronomical data analysis. *Mon.Not.Roy.Astron.Soc.*, 384:449, 2008, 0704.3704.
- [7] Antony Lewis and Sarah Bridle. Cosmological parameters from CMB and other data: a Monte- Carlo approach. *Phys. Rev.*, D66:103511, 2002, astro-ph/0205436.
- [8] John Skilling. Nested sampling. *AIP Conference Proceedings*, 735(1):395–405, 2004.

Part II

Geometry of Heterotic
Orbifolds

Chapter 5

Classification of symmetric toroidal orbifolds

Foreword

This chapter is based on the published paper

Classification of symmetric toroidal orbifolds

Maximilian Fischer, Michael Ratz, Jesús Torrado, and
Patrick K.S. Vaudrevange

Published in the Journal of High Energy Physics 1301 (2013) 084

Preprint in arXiv:1209.3906 [hep-th]

The results presented in it are the product of the combined effort of all its authors, with a special mention to Maximilian Fischer (though, as is customary in High Energy Theoretical Physics, the order of the authors is alphabetical).

As part of this Ph.D. thesis, I reproduce literally a major part of the original publication. In the parts in which my contribution was not significant, only the main results are shown, and discussions are referred to the published paper. This includes, in particular, the calculation of the residual SUSY and the Hodge numbers, and the classification of the non-Abelian cases. In addition, I made a major contribution to the ancillary products of the paper, both to the results and the algorithms used to compute them. These are not reproduced here for reasons of space, but they can be found in <http://einrichtungen.ph.tum.de/T30e/codes/ClassificationOrbifolds>.

Abstract

We provide a complete classification of six-dimensional symmetric toroidal orbifolds which yield $\mathcal{N} \geq 1$ supersymmetry in 4D for the heterotic string. Our strategy is based on a classification of crystallographic space groups in six dimensions. We find in total 520 inequivalent toroidal orbifolds, 162 of them with Abelian point groups such as \mathbb{Z}_3 , \mathbb{Z}_4 , \mathbb{Z}_6 -I etc. and 358 with non-Abelian point groups such as S_3 , D_4 , A_4 etc. We also briefly explore the properties of some orbifolds with Abelian point groups and $\mathcal{N} = 1$; in particular we comment on the possible mechanisms (local or non-local) of gauge symmetry breaking.

5.1 Introduction

Heterotic string model building has received an increasing attention in the past few years. The perhaps simplest heterotic compactifications are based on Abelian toroidal orbifolds [18, 19]. Unlike in the supergravity compactifications on Calabi-Yau manifolds one has a clear string theory description. In addition, the scheme is rich enough to produce a large number of candidate models that may yield a stringy completion of the (supersymmetric) standard model [35, 12] (for a review see e.g. [45]). At the same time, symmetric orbifolds have a rather straightforward geometric interpretation (cf. e.g. [40, 27, 13]). In fact, the geometric properties often have immediate consequences for the phenomenological features of the respective models. One obtains an intuitive understanding of discrete R symmetries in terms of remnants of the Lorentz group of compact space, of the appearance of matter as complete multiplets of the Grand Unified Theory (GUT), due to localization properties and gauge group topographies, as well as of flavor structures.

Despite their simplicity, symmetric toroidal orbifolds provide us with a large number of different settings, which have, rather surprisingly, not been fully explored up to now. In the past, different attempts of classifying parts of these compactifications have been made [3, 21, 26, 17]. As we shall see (in Section 5.5.1) some of these classifications are mutually not consistent, and incomplete. The perhaps most complete classification is due to Donagi and Wendland (DW) [21], who focus on $\mathbb{Z}_2 \times \mathbb{Z}_2$ orbifolds. In this chapter (and in the original publication) we provide a complete classification of symmetric Abelian and non-Abelian heterotic orbifolds that lead to $\mathcal{N} \geq 1$ supersymmetry (SUSY) in four dimensions.

The structure of this chapter is as follows: in Section 5.2 we discuss the tools used to construct toroidal orbifolds. Later, in Section 5.3, we present a way from crystallography to classify all possible space groups and apply it to string compactifications. Then, in Section 5.4 we impose the condition of $\mathcal{N} = 1$ SUSY in 4D (though in this chapter only a general explanation of the procedure is given, see the original publication [25] for details). Section 5.5 is devoted to a survey of the resulting orbifolds, and to a comparison with previous results from the literature [3, 21, 26, 17]. Finally, in Section 5.6 we briefly discuss our results.

In various appendices we collect more detailed information on our classification program. Appendix 5.A contains some details on lattices, in Appendix 5.B we survey the already known 2D orbifolds. The original publication [25] contains an additional appendix containing detailed tables of our results.

5.2 Construction of toroidal orbifolds

We start our discussion with the construction of toroidal orbifolds [18, 19]. There are two equivalent ways of constructing such objects: (i) one can start from the Euclidean space \mathbb{R}^n and divide out a discrete group S , the so-called space group. (ii) Alternatively, one can start with an n -dimensional lattice Λ , to be defined in detail in Section 5.2.2, which determines a torus \mathbb{T}^n and divide out some discrete symmetry group G . Note that G , the so-called orbifolding group as defined in Section 5.2.5, is in general not equal to the point group introduced in Section 5.2.3. That is, a toroidal orbifold is defined as

$$\mathbb{O} = \mathbb{R}^n/S = \mathbb{T}^n/G. \quad (5.1)$$

Even though we are mostly interested in the case $n = 6$ we will keep n arbitrary. In the following, we will properly define the concepts behind Equation (5.1), closely following [10].

5.2.1 The space group S

Let S be a discrete subgroup of the group of motions in \mathbb{R}^n , i.e. every element of S leaves the metric of the space invariant. If S contains n linearly independent translations, then it is called a space group (of degree n). Such groups appear already in crystallography: they are the symmetry groups of crystal structures, which in turn are objects whose symmetries comprise discrete translations.

Every element g of a space group S can be written as a composition of a mapping ϑ that leaves (at least) one point invariant and a translation by some vector $\boldsymbol{\lambda}$, i.e. $g = \boldsymbol{\lambda} \circ \vartheta$ for $g \in S$ (one can think of ϑ as a discrete rotation or inversion). This suggests to write a space group element as¹

$$g = (\vartheta, \boldsymbol{\lambda}), \quad (5.2)$$

and it acts on a vector $\boldsymbol{v} \in \mathbb{R}^n$ as

$$\boldsymbol{v} \xrightarrow{g} \vartheta \boldsymbol{v} + \boldsymbol{\lambda}. \quad (5.3)$$

Let $h = (\omega, \boldsymbol{\tau}) \in S$ be another space group element. Then the composition $h \circ g$ is given by $(\omega \vartheta, \omega \boldsymbol{\lambda} + \boldsymbol{\tau})$.

¹In the mathematical literature the reverse notation $g = (\boldsymbol{\lambda}, \vartheta)$ is also common, since the normal subgroup element is usually written to the left, and the lattice Λ is a normal subgroup of the space group.

5.2.2 The lattice Λ

Let S be a space group. The subgroup Λ of S consisting of all translations in S is the lattice of the space group. Note that for a general element $g = (\vartheta, \boldsymbol{\lambda}) \in S$ the vector $\boldsymbol{\lambda}$ does not need to be a lattice vector. Elements $g = (\vartheta, \boldsymbol{\lambda}) \in S$ with $\boldsymbol{\lambda} \notin \Lambda$ are called roto-translations.

Since a space group is required to contain n linear independent translations, every lattice contains a basis $\boldsymbol{\epsilon} = \{\mathbf{e}_i\}_{i \in \{1, \dots, n\}}$ and the full lattice is spanned by the \mathbf{e}_i (with integer coefficients), i.e. an element $\boldsymbol{\lambda} \in \Lambda$ can be written as $\boldsymbol{\lambda} = n_i \mathbf{e}_i$, summing over $i = 1, \dots, n$ and $n_i \in \mathbb{Z}$. Clearly, the choice of basis is not unique. For example, for a given lattice Λ take two bases $\boldsymbol{\epsilon} = \{\mathbf{e}_1, \dots, \mathbf{e}_n\}$ and $\boldsymbol{f} = \{\mathbf{f}_1, \dots, \mathbf{f}_n\}$ and define $B_{\boldsymbol{\epsilon}}$ and $B_{\boldsymbol{f}}$ as matrices whose columns are the basis vectors in $\boldsymbol{\epsilon}$ and \boldsymbol{f} , respectively. Then the change of basis is given by a unimodular matrix M (i.e. $M \in \text{GL}(n, \mathbb{Z})$) as

$$B_{\boldsymbol{\epsilon}} M = B_{\boldsymbol{f}}. \quad (5.4)$$

On the other hand, one can decide whether two bases $\boldsymbol{\epsilon}$ and \boldsymbol{f} span the same lattice by computing the matrix $M = B_{\boldsymbol{\epsilon}}^{-1} B_{\boldsymbol{f}}$ and checking whether or not it is an element of $\text{GL}(n, \mathbb{Z})$.

5.2.3 The point group P

For a space group S with elements of the form $(\vartheta, \boldsymbol{\lambda})$, the set P of all ϑ forms a finite group ([10, p. 15]), the so-called point group of S . The elements of a point group are sometimes called twists or rotations. However, in general a point group can also contain inversions and reflections, i.e. $\vartheta \in \text{O}(n)$.

The point group P of S maps the lattice of S to itself. Hence, similarly to the change of lattice bases, point group elements can be represented by $\text{GL}(n, \mathbb{Z})$ (i.e. unimodular) matrices. When written in the $\text{GL}(n, \mathbb{Z})$ basis, we append the twists by an index indicating the lattice basis, while the $\text{O}(n)$ (or $\text{SO}(n)$) representation of the twist is denoted without an index. For example, the twist $\vartheta \in \text{O}(n)$ is denoted as $\vartheta_{\boldsymbol{\epsilon}}$ in the lattice basis $\boldsymbol{\epsilon} = \{\mathbf{e}_1, \dots, \mathbf{e}_n\}$ such that $\vartheta \mathbf{e}_i = (\vartheta_{\boldsymbol{\epsilon}})_{ji} \mathbf{e}_j$ and $\vartheta_{\boldsymbol{\epsilon}} = B_{\boldsymbol{\epsilon}}^{-1} \vartheta B_{\boldsymbol{\epsilon}}$. Furthermore, under a change of basis as in Equation (5.4) the twist transforms according to

$$\vartheta_{\boldsymbol{f}} = M^{-1} \vartheta_{\boldsymbol{\epsilon}} M. \quad (5.5)$$

Given these definitions, and because the lattice is always a normal subgroup of the space group (i.e. rotation \circ translation \circ (rotation) $^{-1}$ = translation), the space group S has a semi-direct product structure iff the point group P is a subgroup of it, i.e. $P \subset S$. In that case

$$S = P \ltimes \Lambda, \quad (5.6)$$

and one can write the orbifold as

$$\mathbb{O} = \mathbb{R}^n / (P \ltimes \Lambda) = \mathbb{T}^n / P. \quad (5.7)$$

In general, however, the point group is not a subgroup of the space group and thus the space group is not necessarily a semi-direct product of its point group with its lattice. More precisely, in general the point group P is not equal to the orbifolding group G of Equation (5.1) because of the possible presence of roto-translations, as we will see in an example in Section 5.2.4.

5.2.4 Examples: space groups with \mathbb{Z}_2 point group

In this section, we give two examples of space groups in two dimensions with \mathbb{Z}_2 point group (see app. 5.B) in order to illustrate the discussion of the previous sections.

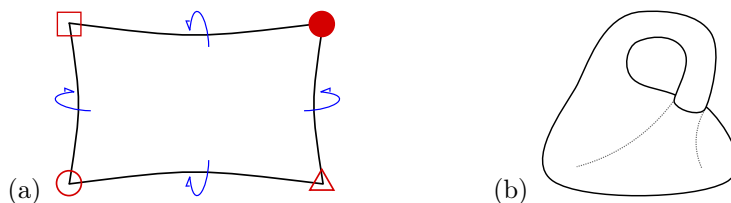


Figure 5.1: Two-dimensional examples: (a) “pillow” and (b) Klein bottle. In case (a) the arrows indicate a wrap-around and the symbols indicate fixed points.

A simple example: the “pillow”

The first of our examples is the well known two-dimensional “pillow”, see Figure 5.1(a). The space group S is generated as

$$S = \langle (\mathbb{1}, \mathbf{e}_1), (\mathbb{1}, \mathbf{e}_2), (\vartheta, \mathbf{0}) \rangle, \quad (5.8)$$

and can be realized as the semi-direct product of the oblique lattice Λ (see Appendix 5.A.3) and the point group $P = \{\mathbb{1}, \vartheta\}$. In detail, the lattice is given as $\Lambda = \{n_1 \mathbf{e}_1 + n_2 \mathbf{e}_2, n_i \in \mathbb{Z}\}$ using the basis $\mathbf{e} = \{\mathbf{e}_1, \mathbf{e}_2\}$. ϑ is a rotation by π , i.e. it acts on the lattice basis vectors as

$$\vartheta \mathbf{e}_i = -\mathbf{e}_i \quad \text{for} \quad i = 1, 2. \quad (5.9)$$

Therefore, it can be represented by a $\text{GL}(2, \mathbb{Z})$ matrix

$$\vartheta_{\mathbf{e}} = \begin{pmatrix} -1 & 0 \\ 0 & -1 \end{pmatrix}. \quad (5.10)$$

Since $\vartheta^2 = \mathbb{1}$, the point group is \mathbb{Z}_2 .

Another example: the Klein bottle

Let us take a look at a more advanced example: the space group of a Klein bottle, see Figure 5.1(b). Here, the space group is generated by two orthogonal lattice vectors (which thus span a primitive rectangular lattice Λ) $\{\mathbf{e}_1, \mathbf{e}_2\}$, and an additional element g ,

$$S = \langle (\mathbb{1}, \mathbf{e}_1), (\mathbb{1}, \mathbf{e}_2), g \rangle \quad \text{with} \quad g = (\vartheta, \frac{1}{2}\mathbf{e}_1) \quad \text{and} \quad \vartheta_{\mathbf{c}} = \begin{pmatrix} 1 & 0 \\ 0 & -1 \end{pmatrix}. \quad (5.11)$$

g acts on a vector $\mathbf{v} = v^1\mathbf{e}_1 + v^2\mathbf{e}_2$ as

$$\mathbf{v} \xrightarrow{g} \vartheta \mathbf{v} + \frac{1}{2}\mathbf{e}_1 = v^1\mathbf{e}_1 - v^2\mathbf{e}_2 + \frac{1}{2}\mathbf{e}_1. \quad (5.12)$$

Notice that even though the point group is \mathbb{Z}_2 (i.e. $\vartheta^2 = \mathbb{1}$), g generates a finite group isomorphic to \mathbb{Z}_2 only on the torus $\mathbb{T}^2 = \mathbb{R}^2/\Lambda$, but not on the Euclidean space \mathbb{R}^2 , because $g^2 = (\mathbb{1}, \mathbf{e}_1) \neq (\mathbb{1}, \mathbf{0})$. In other words, since the generator g also contains a translation $\frac{1}{2}\mathbf{e}_1 \notin \Lambda$, it is not a point group element but a roto-translation.

Obviously, this space group cannot be written as a semi-direct product of a lattice and a point group, as is always the case when we have roto-translations.

5.2.5 The orbifolding group G

Due to the possible presence of roto-translations, it is clear that in general space groups cannot be described by lattices and point groups only. Therefore, we will need to define an additional object, the orbifolding group (see [21]). Loosely speaking, the orbifolding group G is generated by those elements of S that have a non-trivial twist part, identifying elements which differ by a lattice translation. Hence, if there are no roto-translations the orbifolding group G is equal to the point group P . In other words, the orbifolding group may contain space group elements with non-trivial, non-lattice translational parts. Combining the orbifolding group G and the torus lattice Λ generates the space group $S = \langle \{G, \Lambda\} \rangle$.

Hence, we can define the orbifold as

$$\mathbb{O} = \mathbb{R}^n/S = \mathbb{R}^n/\langle \{G, \Lambda\} \rangle = (\mathbb{R}^n/\Lambda)/G = \mathbb{T}^n/G. \quad (5.13)$$

Orbifolds can be manifolds (see e.g. Figure 5.1(b)), but in general, they come with singularities which can not be endowed with smooth maps (see e.g. Figure 5.1(a)).

5.3 Equivalences of space groups

In the context of string orbifold compactifications, some physical properties of a given model directly depend on the choice of its space group. These features are

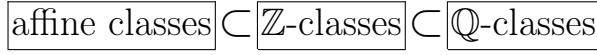


Figure 5.2: Sketch of the classification of space groups.

common to whole sets of space groups and can be related to some mathematical properties. Using the latter, one can define equivalence classes of space groups. In detail, there are three kinds of equivalence classes suitable to sort space groups S with certain physical and corresponding mathematical properties. These classes are:

1. the \mathbb{Q} -class (see Section 5.3.3) determines the point group P contained in S and hence the number of supersymmetries in 4D and the number of geometrical moduli;
2. the \mathbb{Z} -class (see Section 5.3.2) determines the lattice Λ of S and hence the nature of the geometrical moduli;
3. the affine class (see Section 5.3.1) determines the flavor group and the nature of gauge symmetry breaking (i.e. local vs. non-local gauge symmetry breaking).

Each \mathbb{Q} -class can contain several \mathbb{Z} -classes and each \mathbb{Z} -class can contain several affine classes, see Figure 5.2. In other words, for every point group there can be several inequivalent lattices and for every lattice there can be several inequivalent choices for the orbifolding group (i.e. with or without roto-translations).

In the following, we will discuss in detail why the concept of affine classes is advantageous to classify physically inequivalent space groups. This is standard knowledge among crystallographers and can for instance be found in more detail in [10].

5.3.1 Affine classes of space groups

Two space groups S_1 and S_2 of degree n belong to the same affine class (i.e. $S_1 \sim S_2$) if there is an affine mapping $f : \mathbb{R}^n \rightarrow \mathbb{R}^n$ such that

$$f^{-1} S_1 f = S_2 . \tag{5.14}$$

An affine mapping $f = (A, t)$ on \mathbb{R}^n consists of a translation t and a linear mapping A , that is, it allows for rescalings and rotations. Therefore, this definition enables us to distinguish between space groups that actually describe different symmetries and space groups which are just the ones we already know, looked upon from a different angle or distance. Then, for a given representative space group of an affine class a non-trivial affine transformation A that leaves the point group invariant (i.e. $A^{-1} P A = P$) corresponds to a change of the geometrical data. In the context of superstring compactifications this corresponds to a change of values

of the geometrical moduli. That is, affine transformations amount to moving in the moduli space of the respective compactification. Hence, we will only be interested in one representative for every affine class.

It turns out that, for a given dimension n , there exists only a finite number of affine classes of space groups [10, p. 10]. Hence, classifying all affine classes of space groups enables a complete classification of orbifolds for a fixed number of dimensions. In this chapter, we focus on the six-dimensional case.

Example in two dimensions

Let us illustrate this at the $\mathbb{T}^2/\mathbb{Z}_2$ example, or “pillow”, with $\vartheta = -\mathbb{1}$ given in Section 5.2.4. As discussed there, the lattice is oblique, i.e. one can choose any linear independent vectors \mathbf{e}_1 and \mathbf{e}_2 as basis vectors. Define a space group S by choosing

$$\mathbf{e}_1 = \begin{pmatrix} r_1 \\ 0 \end{pmatrix} \quad \text{and} \quad \mathbf{e}_2 = \begin{pmatrix} r_2 \cos(\alpha) \\ r_2 \sin(\alpha) \end{pmatrix}. \quad (5.15)$$

This space group is in the same affine class as \tilde{S} with basis vectors

$$\tilde{\mathbf{e}}_1 = \begin{pmatrix} 1 \\ 0 \end{pmatrix} \quad \text{and} \quad \tilde{\mathbf{e}}_2 = \begin{pmatrix} 0 \\ 1 \end{pmatrix}. \quad (5.16)$$

This can be seen explicitly using the affine transformation $f = (A, \mathbf{0})$ with

$$A = \begin{pmatrix} r_1 & r_2 \cos(\alpha) \\ 0 & r_2 \sin(\alpha) \end{pmatrix} \quad \text{and} \quad A^{-1} = \begin{pmatrix} \frac{1}{r_1} & -\frac{1}{r_1 \tan(\alpha)} \\ 0 & \frac{1}{r_2 \sin(\alpha)} \end{pmatrix}. \quad (5.17)$$

Take an arbitrary element $g = (\vartheta, n_i \mathbf{e}_i)$ with $n_i \in \mathbb{Z}$ for $i = 1, 2$. Then

$$(f^{-1} g f)(\mathbf{x}) = (f^{-1} g)(A\mathbf{x}) = f^{-1}(\vartheta A\mathbf{x} + n_i \mathbf{e}_i) \quad (5.18a)$$

$$= \vartheta \mathbf{x} + A^{-1}(n_i \mathbf{e}_i) = \vartheta \mathbf{x} + n_i \tilde{\mathbf{e}}_i = \tilde{g} \mathbf{x} \quad (5.18b)$$

for $\mathbf{x} \in \mathbb{R}^2$ and $\tilde{g} = (\vartheta, n_i \tilde{\mathbf{e}}_i) \in \tilde{S}$. Therefore, $S \sim \tilde{S}$ and there is only one affine class of $\mathbb{T}^2/\mathbb{Z}_2$ space groups with $\vartheta = -\mathbb{1}$.

This should be compared with the $\mathbb{T}^2/\mathbb{Z}_3$ orbifold (see app. 5.B), where the angle between the basis vectors \mathbf{e}_i and their length ratio are fixed, such that the corresponding moduli space is different. Hence, it is clear that $\mathbb{T}^2/\mathbb{Z}_2$ and $\mathbb{T}^2/\mathbb{Z}_3$ are two different orbifolds. This demonstrates the advantages of using affine classes for the classification of space groups.

5.3.2 \mathbb{Z} -classes of space groups

As discussed above, we can sort space groups into affine classes. This can be refined further by grouping affine classes according to common properties of their

point groups. Following the argument in Section 5.2.3, the elements of the point group can be written in the lattice basis as elements of $\text{GL}(n, \mathbb{Z})$. Therefore, a point group is a finite subgroup of the unimodular group on \mathbb{Z} .

Take two space groups S_1 and S_2 . For $i = 1, 2$, the space group S_i contains a lattice Λ_i and its point group in the lattice basis is denoted by P_i , i.e. $P_i \subset \text{GL}(n, \mathbb{Z})$. Then, the two space groups belong to the same \mathbb{Z} -class (or in other words to the same arithmetic crystal class) if there exists an unimodular matrix U (i.e. $U \in \text{GL}(n, \mathbb{Z})$) such that (cf. the parallel discussion around Equation (5.14))

$$U^{-1} P_1 U = P_2, \tag{5.19}$$

see Equation (5.5). That is, if the point groups are related by a change of lattice basis (using U), the space groups belong to the same \mathbb{Z} -class. Hence, \mathbb{Z} -classes classify the inequivalent lattices.

If two space groups belong to the same \mathbb{Z} -class, they have the same *form space* (see app. 5.A.1) and, physically, they possess the same amount and nature of geometrical moduli. However, as we have stressed before, space groups from the same \mathbb{Z} -class are not necessarily equivalent because of the possible presence of roto-translations. In other words, space groups from the same \mathbb{Z} -class can belong to different affine classes and can hence be inequivalent.

5.3.3 \mathbb{Q} -classes of space groups

As before in Section 5.3.2, take two space groups S_1 and S_2 . For $i = 1, 2$, the point group in the lattice basis associated to the space group S_i is denoted by P_i , i.e. $P_i \subset \text{GL}(n, \mathbb{Z})$. Then, the two space groups belong to the same \mathbb{Q} -class (or in other words to the same geometric crystal class) if there exists a matrix $V \in \text{GL}(n, \mathbb{Q})$ such that

$$V^{-1} P_1 V = P_2. \tag{5.20}$$

Obviously, if two space groups belong to the same \mathbb{Z} -class they also belong to the same \mathbb{Q} -class, hence the inclusion sketch in Figure 5.2. In contrast to \mathbb{Z} -classes, \mathbb{Q} -classes do not distinguish between inequivalent lattices. However, if two space groups belong to the same \mathbb{Q} -class, the commutation relations and the orders of the corresponding point groups are the same. Therefore, they are isomorphic as crystallographic point groups. They also possess form spaces of the same dimension, i.e. they have the same number of moduli. What is important for physics is that all space groups in the same \mathbb{Q} -class share a common holonomy group (cf. Section 5.4). This allows us to identify settings that yield $\mathcal{N} = 1$ SUSY in 4D. In particular, in order to determine the number of SUSY generators, it is sufficient to consider only one representative from every \mathbb{Q} -class.

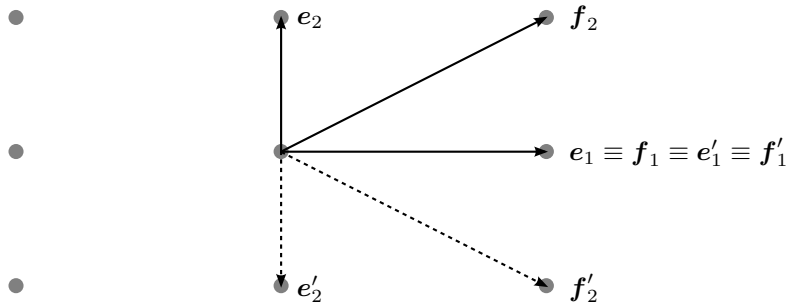


Figure 5.3: Two different bases for the p-rectangular lattice: $\mathbf{e} = \{\mathbf{e}_1, \mathbf{e}_2\}$ and $\mathbf{f} = \{\mathbf{f}_1, \mathbf{f}_2\}$, and the action of the point group generator (primed vectors).

5.3.4 Some examples

Before going to six dimensions, let us illustrate the above definitions with some easy examples of two-dimensional \mathbb{Z}_2 orbifolds, taken from Appendix 5.B.

Space groups in the same \mathbb{Z} -class

Consider the affine class $\mathbb{Z}_2\text{-II-1-1}$, as defined in Appendix 5.B. As there are no roto-translations, the orbifolding group is equal to the point group and is generated by ϑ , a reflection at the horizontal axis. Now, let this reflection act on a lattice, first spanned by the basis vectors $\mathbf{e} = \{\mathbf{e}_1, \mathbf{e}_2\}$ and second spanned by $\mathbf{f} = \{\mathbf{f}_1, \mathbf{f}_2\}$, see Figure 5.3. The two corresponding space groups read

$$S_{\mathbf{e}} = \langle (\vartheta, \mathbf{0}), (\mathbf{1}, \mathbf{e}_1), (\mathbf{1}, \mathbf{e}_2) \rangle \quad \text{with} \quad \vartheta_{\mathbf{e}} = \begin{pmatrix} 1 & 0 \\ 0 & -1 \end{pmatrix}, \quad (5.21)$$

$$S_{\mathbf{f}} = \langle (\vartheta, \mathbf{0}), (\mathbf{1}, \mathbf{f}_1), (\mathbf{1}, \mathbf{f}_2) \rangle \quad \text{with} \quad \vartheta_{\mathbf{f}} = \begin{pmatrix} 1 & 2 \\ 0 & -1 \end{pmatrix}, \quad (5.22)$$

where $\vartheta_{\mathbf{e}} \neq \vartheta_{\mathbf{f}}$ because they are given in their corresponding lattice bases. However, it is easy to see that they are related by the $\text{GL}(2, \mathbb{Z})$ transformation

$$U = \begin{pmatrix} 1 & 1 \\ 0 & 1 \end{pmatrix} \quad \text{with} \quad U^{-1} \vartheta_{\mathbf{e}} U = \vartheta_{\mathbf{f}}, \quad (5.23)$$

cf. Equation (5.19). Therefore, they belong to the same \mathbb{Z} -class. Hence, as we actually knew from the start, they act on the same lattice and the matrix U just defines the associated change of basis precisely as in Equation (5.4).

Space groups in the same \mathbb{Q} -class, but different \mathbb{Z} -classes

Next, consider the space groups,

$$S_{1-1} = \langle (\vartheta_{1-1}, 0), (\mathbf{1}, \mathbf{e}_1), (\mathbf{1}, \mathbf{e}_2) \rangle \quad \text{with} \quad \vartheta_{1-1, \epsilon} = \begin{pmatrix} 1 & 0 \\ 0 & -1 \end{pmatrix}, \quad (5.24)$$

$$S_{2-1} = \langle (\vartheta_{2-1}, 0), (\mathbf{1}, \mathbf{f}_1), (\mathbf{1}, \mathbf{f}_2) \rangle \quad \text{with} \quad \vartheta_{2-1, f} = \begin{pmatrix} 0 & 1 \\ 1 & 0 \end{pmatrix}, \quad (5.25)$$

with lattices spanned by $\mathbf{e}_1 = (1, 0)$, $\mathbf{e}_2 = (0, 1)$ and $\mathbf{f}_1 = (1/2, 1/2)$, $\mathbf{f}_2 = (1/2, -1/2)$, respectively. The first space group belongs to the affine class $\mathbb{Z}_2\text{-II-1-1}$ and the second one to $\mathbb{Z}_2\text{-II-2-1}$, see Appendix 5.B. If we try to find the transformation V from Equation (5.20) that fulfills $V^{-1} \vartheta_{1-1, \epsilon} V = \vartheta_{2-1, f}$ we see that

$$V = \begin{pmatrix} x & x \\ y & -y \end{pmatrix} \quad \text{with} \quad x, y \in \mathbb{Q}. \quad (5.26)$$

But for all values of x and y for which V^{-1} exists, either V or V^{-1} has non-integer entries. Therefore, the space groups $\mathbb{Z}_2\text{-II-1-1}$ and $\mathbb{Z}_2\text{-II-2-1}$ belong to the same \mathbb{Q} -class, but to different \mathbb{Z} -classes. In other words, these space groups are defined with inequivalent lattices. Indeed, the first space group possesses a primitive rectangular lattice, while the second one has a centered rectangular lattice, as we will see in detail in the following.

The effect of including additional translations

There is an alternative way of seeing the relationship between the two space groups of the last example: one can amend one of the space groups by an additional translation. In general, this gives rise to a new lattice, and consequently to a different \mathbb{Z} -class.

In our case, let us take the $\mathbb{Z}_2\text{-II-1-1}$ affine class and add the non-lattice translation

$$\boldsymbol{\tau} = \frac{1}{2}(\mathbf{e}_1 + \mathbf{e}_2) \quad (5.27)$$

to its space group. If we incorporate this translation into the lattice, we notice that this element changes the original primitive rectangular lattice to a centered rectangular lattice, with a fundamental cell of half area. The new lattice (see Figure 5.4) can be spanned by the basis vectors $\boldsymbol{\tau}$ and $\mathbf{e}_1 - \boldsymbol{\tau}$.

We can interpret the inclusion of this additional translation as a “change of basis”, see Equation (5.4), but now generated by a matrix $M \in \text{GL}(2, \mathbb{Q})$ instead of one from $\text{GL}(2, \mathbb{Z})$. The transformation looks like

$$B_{\epsilon} M = B_{\tau} \quad \text{with} \quad M = \begin{pmatrix} 1/2 & 1/2 \\ 1/2 & -1/2 \end{pmatrix}, \quad (5.28)$$

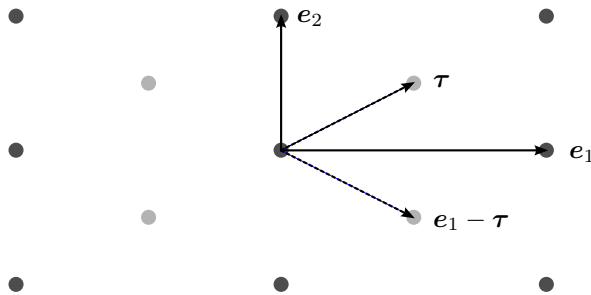


Figure 5.4: Change of a lattice by an additional translation: the basis of the original lattice is solid, the basis of the new one dashed. The additional lattice points are light gray. The action of ϑ is a reflection at the horizontal axis. Therefore, it maps e_1 to itself, e_2 to its negative and interchanges τ and $e_1 - \tau$.

where B_e and B_τ are matrices whose columns are (e_1, e_2) and $(\tau, e_1 - \tau)$, respectively. M is precisely the matrix in Equation (5.26) with values $x = y = 1/2$. Performing this basis change, the twist has to be transformed accordingly. Hence, the two \mathbb{Z} -classes are related by a $\text{GL}(2, \mathbb{Q})$ transformation M and the new space group with lattice B_τ is $\mathbb{Z}_2\text{-II-}2-1$. The geometrical action of the twist, however, is the same in both cases: it is a reflection at the horizontal axis (see Figure 5.4). That is the reason for the name geometrical crystal classes for \mathbb{Q} -classes. A general method for including additional translations can be found in Appendix 5.A.2.

The method of using additional translations has been used in [21] and [17] in order to classify six-dimensional space groups with point groups $\mathbb{Z}_N \times \mathbb{Z}_N$ for $N = 2, 3, 4, 6$ (the classification of [17] is not fully exhaustive, see Section 5.5.1). In these works, the authors start with factorized lattices, i.e. lattices which are the orthogonal sum of three two-dimensional sublattices, on which the twists act diagonally. Then, in a second step additional translations are introduced. As we have shown here, adding such translations is equivalent to switching between \mathbb{Z} -classes in the same \mathbb{Q} -class. Hence, if one considers all possible lattices (\mathbb{Z} -classes) additional translations do not give rise to new orbifolds.

Space groups in different \mathbb{Q} -classes

Finally, consider the affine classes $\mathbb{Z}_2\text{-I-}1-1$ and $\mathbb{Z}_2\text{-II-}1-1$ defined in Appendix 5.B. If we try to find a transformation between both space groups generators, see Equation (5.20),

$$V^{-1} \begin{pmatrix} -1 & 0 \\ 0 & -1 \end{pmatrix} V = \begin{pmatrix} 1 & 0 \\ 0 & -1 \end{pmatrix} \Leftrightarrow \begin{pmatrix} -1 & 0 \\ 0 & -1 \end{pmatrix} V = V \begin{pmatrix} 1 & 0 \\ 0 & -1 \end{pmatrix}, \quad (5.29)$$

we obtain

$$V = \begin{pmatrix} 0 & x \\ 0 & y \end{pmatrix} \notin \text{GL}(2, \mathbb{Q}) \quad \forall x, y. \quad (5.30)$$

Therefore, the space groups $\mathbb{Z}_2\text{-I-1-1}$ and $\mathbb{Z}_2\text{-II-1-1}$ belong to different \mathbb{Q} -classes (and also to different \mathbb{Z} -classes). That is, the point groups are inequivalent: the twist of the first point group is a reflection at the origin and the twist of the second point group is a reflection at the horizontal axis.

5.4 Classification of space groups

In this section we describe our strategy to classify all inequivalent space groups for the compactification of the heterotic string to four dimensions with $\mathcal{N} = 1$ SUSY.

5.4.1 Classification strategy

The amount of residual supersymmetry exhibited by the 4D effective theory is related to the holonomy group of the compact space [14]. In detail, for the heterotic string the number \mathcal{N} of residual SUSY in 4D is given by the number of covariantly constant spinors and, therefore, depends on the holonomy group. For example, a trivial holonomy group yields four covariantly constant spinors and hence $\mathcal{N} = 4$ in 4D. On the other hand, one gets $\mathcal{N} = 1$ SUSY in 4D for $\text{SU}(3)$ holonomy.

In the context of orbifolds, one can relate the holonomy group to the point group [19]. Orbifold compactifications preserve four-dimensional supersymmetry if the point group is a discrete subgroup of $\text{SU}(3)$. The holonomy group and hence the amount of unbroken SUSY is the same for all members of a given \mathbb{Q} -class. Therefore, we start our classification with the identification of all \mathbb{Q} -classes (i.e. point groups) that are subgroups of $\text{SU}(3)$. Then, for each \mathbb{Q} -class we identify all \mathbb{Z} -classes (i.e. lattices) and finally construct for each \mathbb{Z} -class all affine classes (i.e. roto-translations).

In more detail, our strategy reads:

1. Choose a \mathbb{Q} -class and find a representative P of it.²
2. Check that P is a subgroup of $\text{SO}(6)$ rather than $\text{O}(6)$.
3. Verify that P is a subgroup of $\text{SU}(3)$.
4. Find every possible \mathbb{Z} -class inside that \mathbb{Q} -class.
5. Find every possible affine class inside each one of those \mathbb{Z} -classes.

²A discussion about the possible orders of the elements of the point group, and therefore the possible point groups, can be found in Appendix 5.B.

There exists a catalog of every possible affine class in up to six dimensions classified into \mathbb{Z} - and \mathbb{Q} -classes [47]. Furthermore, one can access this catalog easily using the software CARAT [48]. In detail, the command `Q_catalog` lists all \mathbb{Q} -classes, the command `QtoZ` lists all \mathbb{Z} -classes of a given \mathbb{Q} -class and, finally, the command `Extensions` lists all affine classes of a given \mathbb{Z} -class. Hence, the main open question is to decide whether a given representative of a \mathbb{Q} -class is a subgroup of $SU(3)$.

5.4.2 Residual SUSY

We start by verifying that $P \subset SO(6)$. CARAT offers representatives for all \mathbb{Q} -classes, i.e. it gives the generators of the point group P in some (unspecified) lattice basis \mathfrak{e} as $GL(6, \mathbb{Z})$ matrices $\vartheta_{\mathfrak{e}}$. One can check whether or not the determinant equals $+1$ for all generators of P in the $GL(6, \mathbb{Z})$ form given by CARAT. This allows us to determine whether or not $P \subset SO(6)$.

Next, we recall that the matrices $\vartheta_{\mathfrak{e}} \in P$ originate from the six-dimensional representation $\mathbf{6}$ of $SO(6)$. One way to check that P is a subgroup of $SU(3)$ is to consider the breaking of the $\mathbf{6}$ into representations of $SU(3)$,

$$\mathbf{6} \rightarrow \mathbf{3} \oplus \bar{\mathbf{3}}. \quad (5.31)$$

On the other hand, the six-dimensional representation is, in general, a reducible representation of the point group P . Hence, it can be decomposed

$$\mathbf{6} \rightarrow \mathbf{a} \oplus \mathbf{b} \oplus \dots \quad (5.32)$$

into irreducible representations $\mathbf{a}, \mathbf{b}, \dots$ of P .

If P is a subgroup of $SU(3)$ this decomposition has to be of the kind

$$\mathbf{6} \rightarrow \mathbf{a} \oplus \bar{\mathbf{a}}, \quad (5.33)$$

where \mathbf{a} denotes some (in general reducible) representation of P originating from the $\mathbf{3}$ of $SU(3)$ and $\bar{\mathbf{a}}$ its complex conjugate (from $\bar{\mathbf{3}}$ of $SU(3)$). In addition, one needs to know the explicit matrix representation of \mathbf{a} in order to check that the determinant is $+1$. Then $P \subset SU(3)$ and at least $\mathcal{N} = 1$ SUSY survives the compactification of the heterotic string on the corresponding orbifold.

The full detailed procedure can be found in section 4.2 of the original publication [25].

5.5 Results: classification of toroidal orbifolds

We perform a systematic classification of space groups that keep (at least) $\mathcal{N} = 1$ SUSY in four dimensions unbroken. As discussed in Section 5.3, the amount of unbroken supersymmetry depends only on the \mathbb{Q} -class (i.e. point group). Using CARAT we know that there are 7103 \mathbb{Q} -classes in six dimensions. Out of those,

we find 60 \mathbb{Q} -classes with $\mathcal{N} \geq 1$ SUSY where 52 lead to precisely $\mathcal{N} = 1$, see Table 5.1 for a summary of the results. The 60 cases split into 22 Abelian and 38 non-Abelian \mathbb{Q} -classes, where the Abelian cases were already known in the literature. By contrast, most of the 38 non-Abelian \mathbb{Q} -classes have not been used in orbifold compactifications before. Starting from these 60 \mathbb{Q} -classes we construct all possible \mathbb{Z} - and affine classes (i.e. lattices and roto-translations). In the following we discuss them in detail: Sections 5.5.1 and 5.5.2 are devoted to the Abelian and non-Abelian case, respectively.

# of generators	# of SUSY	Abelian	non-Abelian
1	$\mathcal{N} = 4$	1	0
	$\mathcal{N} = 2$	4	0
	$\mathcal{N} = 1$	9	0
		14	0
2	$\mathcal{N} = 4$	0	0
	$\mathcal{N} = 2$	0	3
	$\mathcal{N} = 1$	8	32
		8	35
3	$\mathcal{N} = 4$	0	0
	$\mathcal{N} = 2$	0	0
	$\mathcal{N} = 1$	0	3
		0	3
total:	$\mathcal{N} = 4$	1	0
	$\mathcal{N} = 2$	4	3
	$\mathcal{N} = 1$	17	35
		22	38

Table 5.1: Summary of the classification of all point groups with at least $\mathcal{N} = 1$ SUSY. Out of 7103 cases obtained from CARAT there are 60 point groups with $\mathcal{N} \geq 1$ SUSY where 52 have exactly $\mathcal{N} = 1$.

5.5.1 Abelian toroidal orbifolds

Our results

Restricting ourselves to Abelian point groups, we find 17 point groups with $\mathcal{N} = 1$ SUSY, four cases with $\mathcal{N} = 2$ and one case (i.e. the trivial point group) with $\mathcal{N} = 4$ supersymmetry. Next, we classify all \mathbb{Z} - and affine classes. For the 17 point groups with $\mathcal{N} = 1$ it turns out that there are in total 138 inequivalent space groups with Abelian point group and $\mathcal{N} = 1$. Many of them were unknown before. The results are summarized in Table 5.2. More details including the generators of the orbifolding group G , the nature of gauge symmetry breaking (i.e. local or non-local) and the Hodge numbers $(h^{(1,1)}, h^{(2,1)})$ can be found in Appendix C.1 in the

original publication [25], which also includes, on the corresponding section to the present one, a comment on the distribution of the Hodge numbers and the effect of them in the amount of Standard Model generations.

label of \mathbb{Q} -class	twist vector(s)	# of \mathbb{Z} -classes	# of affine classes
\mathbb{Z}_3	$\frac{1}{3}(1, 1, -2)$	1	1
\mathbb{Z}_4	$\frac{1}{4}(1, 1, -2)$	3	3
\mathbb{Z}_6 -I	$\frac{1}{6}(1, 1, -2)$	2	2
\mathbb{Z}_6 -II	$\frac{1}{6}(1, 2, -3)$	4	4
\mathbb{Z}_7	$\frac{1}{7}(1, 2, -3)$	1	1
\mathbb{Z}_8 -I	$\frac{1}{8}(1, 2, -3)$	3	3
\mathbb{Z}_8 -II	$\frac{1}{8}(1, 3, -4)$	2	2
\mathbb{Z}_{12} -I	$\frac{1}{12}(1, 4, -5)$	2	2
\mathbb{Z}_{12} -II	$\frac{1}{12}(1, 5, -6)$	1	1
$\mathbb{Z}_2 \times \mathbb{Z}_2$	$(0, 1, -1), \frac{1}{2}(1, 0, -1)$	12	35
$\mathbb{Z}_2 \times \mathbb{Z}_4$	$(0, 1, -1), \frac{1}{4}(1, 0, -1)$	10	41
$\mathbb{Z}_2 \times \mathbb{Z}_6$ -I	$(0, 1, -1), \frac{1}{6}(1, 0, -1)$	2	4
$\mathbb{Z}_2 \times \mathbb{Z}_6$ -II	$(0, 1, -1), \frac{1}{6}(1, 1, -2)$	4	4
$\mathbb{Z}_3 \times \mathbb{Z}_3$	$(0, 1, -1), \frac{1}{3}(1, 0, -1)$	5	15
$\mathbb{Z}_3 \times \mathbb{Z}_6$	$(0, 1, -1), \frac{1}{6}(1, 0, -1)$	2	4
$\mathbb{Z}_4 \times \mathbb{Z}_4$	$(0, 1, -1), \frac{1}{4}(1, 0, -1)$	5	15
$\mathbb{Z}_6 \times \mathbb{Z}_6$	$(0, 1, -1), \frac{1}{6}(1, 0, -1)$	1	1
# of Abelian $\mathcal{N} = 1$		60	138

Table 5.2: Summary of all space groups with Abelian point group and $\mathcal{N} = 1$ SUSY. The corresponding table in the original publication [25] also contains the identification information of each of these \mathbb{Q} -classes in CARAT and the ‘‘GAPID’’ of their point groups in the algebra software GAP.

The results are also available as input for the orbifolder [46], a tool to study the low energy phenomenology of heterotic orbifolds. We have created input files for the orbifolder, which we have made available at

[http://einrichtungen.physik.tu-muenchen.de/T30e/codes/
ClassificationOrbifolds/](http://einrichtungen.physik.tu-muenchen.de/T30e/codes/ClassificationOrbifolds/) .

There is a geometry file for each of the 138 affine classes, and one model file per \mathbb{Q} -class, that contains a model with standard embedding for each of the corresponding affine classes in that \mathbb{Q} -class.

In addition, we find 23 inequivalent space groups (i.e. affine classes) with Abelian point group and $\mathcal{N} = 2$. These space groups are based on the well-known four Abelian point groups $\mathbb{Z}_2, \mathbb{Z}_3, \mathbb{Z}_4$ and \mathbb{Z}_6 . However, the inequivalent lattices and roto-translations were unknown before. They are summarized in Table 5.3.

label of \mathbb{Q} -class	# of \mathbb{Z} -classes	# of affine classes
\mathbb{Z}_2	3	5
\mathbb{Z}_3	3	5
\mathbb{Z}_4	3	9
\mathbb{Z}_6	1	4
# of Abelian $\mathcal{N} = 2$	10	23

Table 5.3: Summary of all space groups with $\mathcal{N} > 1$ SUSY for Abelian point groups P . In addition, there is the trivial \mathbb{Q} -class with $\mathcal{N} = 4$ SUSY, with one \mathbb{Z} - and one affine class. The corresponding table in the original publication [25] also contains the identification information of each of these \mathbb{Q} -classes in CARAT and the “GAPID” of their point groups in the algebra software GAP.

Previous classifications

There have been several attempts in the literature to classify six-dimensional $\mathcal{N} = 1$ SUSY preserving Abelian toroidal orbifolds. For example, Bailin and Love [3] give a classification for \mathbb{Z}_N orbifolds using root lattices of semi-simple Lie algebras of rank six as lattices Λ and the (generalized) Coxeter element as the generator of the point group P . However, as also discussed in Appendix 5.A.3, they overcount the geometries and, in addition, miss a few cases. A detailed comparison to our results can be found in Table 5.4.

For $\mathbb{Z}_2 \times \mathbb{Z}_2$ orbifolds there have been two approaches for the classification of geometries. In the first one, the classification is based on Lie lattices [26], see also [39]. Again, this classification is somewhat incomplete: it misses four lattices and, in addition, neglects the possibility of roto-translations. In a second approach by DW [21] (based on [20]), a classification for $\mathbb{Z}_2 \times \mathbb{Z}_2$ is given, which, as we find, is complete, see Table 5.5 for a comparison. In addition, we were able to resolve an ambiguity between the models 3–1 and 3–2 of DW.

Furthermore, based on the strategy of DW [21], there is an (incomplete) classification of $\mathbb{Z}_N \times \mathbb{Z}_N$ for $N = 3, 4$ and 6 [17]. For both $\mathbb{Z}_3 \times \mathbb{Z}_3$ and $\mathbb{Z}_4 \times \mathbb{Z}_4$ he identifies 8 out of 15 affine classes (compare Section 2.3 of [17] to the table in Appendix C.1 in the original publication [25]). The Hodge numbers agree with our findings except for case IV.7 (i.e. $\mathbb{Z}_4 \times \mathbb{Z}_4$ with $(38, 0)$). Finally, in the case of $\mathbb{Z}_6 \times \mathbb{Z}_6$ [17] correctly identifies that there is only one possible geometry but the Hodge numbers disagree with ours, i.e. [17] finds $(80, 0)$ and we have $(84, 0)$.

Fundamental groups

The fundamental group of a toroidal orbifold with space group S is given as [19, 11]

$$\pi_1 = S / \langle F \rangle, \quad (5.34)$$

Q-class	Z-class	corresponding root lattice(s)
\mathbb{Z}_3	1	$SU(3)^3$
\mathbb{Z}_4	1	$SO(5)^2 \times SU(2)^2$
	2	$SO(5) \times SU(4) \times SU(2)$
	3	$SU(4)^2$
\mathbb{Z}_6 -I	1	$(G_2)^2 \times SU(3)$ and $(SU(3)^{[2]})^2 \times SU(3)$
	2	—
\mathbb{Z}_6 -II	1	$G_2 \times SU(3) \times SU(2)^2$ and $SU(3)^{[2]} \times SU(3) \times SU(2)^2$
	2	—
	3	$SO(8) \times SU(3)$ and $SO(7) \times SU(3) \times SU(2)$ and $SU(4)^{[2]} \times SU(3) \times SU(2)$
	4	$SU(6) \times SU(2)$
\mathbb{Z}_7	1	$SU(7)$
\mathbb{Z}_8 -I	1	$SO(9) \times SO(5)$ and $SO(8)^{[2]} \times SO(5)$
	2	—
	3	—
\mathbb{Z}_8 -II	1	$SO(8)^{[2]} \times SU(2)^2$ and $SO(9) \times SU(2)^2$
	2	$SO(10) \times SU(2)$
\mathbb{Z}_{12} -I	1	$F_4 \times SU(3)$ and $SO(8)^{[3]} \times SU(3)$
	2	E_6
\mathbb{Z}_{12} -II	1	$SO(4) \times F_4$ and $SO(8)^{[3]} \times SU(2)^2$

Table 5.4: Matching between our classification of \mathbb{Z}_N space groups and the traditional notation of lattices as root lattices of semi-simple Lie algebras of rank six, see e.g. Table 3 of [3] and Table D.1 of [51]. Cases previously not known are indicated with a dash.

where $\langle F \rangle$ is the group generated by those space group elements that leave some points fixed.

The fundamental groups of most of the Abelian orbifolds discussed here are trivial, for in those cases $\langle F \rangle \equiv S$. The only non-trivial cases are the following (see the table in Appendix C.1 in the original publication [25]):

- 21 space groups from the $\mathbb{Z}_2 \times \mathbb{Z}_2$ Q-class as already calculated in [21]. See Table 5.5, where
 - 0 means a trivial fundamental group
 - S means the fundamental group equals the space group (no fixed points, hence $\langle F \rangle = \{1\}$)
 - A means a $\mathbb{Z}_2 \times \mathbb{Z}^2$ fundamental group

Here	Donagi et al. [21]	Förste et al. [26]	π_1
1-1	0-1	$SU(2)^6$	0
1-2	0-2	—	0
1-3	0-3	—	A
1-4	0-4	—	S
2-1	1-6	$SU(3) \times SU(2)^4$	0
2-2	1-8	—	0
2-3	1-10	—	A
2-4	1-7	—	C
2-5	1-9	—	A
2-6	1-11	—	S
3-1	2-9	—	0
3-2	2-10	—	0
3-3	2-11	—	A
3-4	2-12	—	S
4-1	2-13	$SU(3)^2 \times SU(2)^2$ -I	0
4-2	2-14	—	D
5-1	1-1	$SU(4) \times SU(2)^3$	C
5-2	1-3	—	C
5-3	1-2	—	0
5-4	1-4	—	A
5-5	1-5	—	S
6-1	2-6	$SU(3)^2 \times SU(2)^2$ -II	0
6-2	2-7	—	C
6-3	2-8	—	A
7-1	3-3	—	0
7-2	3-4	—	C
8-1	4-1	—	0
9-1	2-3	$SU(4) \times SU(3) \times SU(2)$	C
9-2	2-5	—	D
9-3	2-4	—	0
10-1	3-5	—	C
10-2	3-6	—	0
11-1	3-1 \equiv 3-2	$SU(3)^3$	0
12-1	2-1	$SU(4)^2$	D
12-2	2-2	—	C

Table 5.5: Comparison of the affine classes of $\mathbb{Z}_2 \times \mathbb{Z}_2$ between our classification and the ones in [21] and [26]. In our case, the two numbers enumerate the \mathbb{Z} - and affine classes, respectively.

- C means a \mathbb{Z}_2 fundamental group
- D means a $(\mathbb{Z}_2)^2$ fundamental group
- 6 space groups from the $\mathbb{Z}_2 \times \mathbb{Z}_4$ Q-class. In detail, the affine classes 1–6, 2–4, 3–6, 4–4, 6–5 and 8–3 possess a \mathbb{Z}_2 fundamental group.
- 4 space groups from the $\mathbb{Z}_3 \times \mathbb{Z}_3$ Q-class. In detail, the affine classes 1–4, 2–4, 3–3 and 4–3 possess a \mathbb{Z}_3 fundamental group.

Elements of the space group that leave no fixed points are called freely acting. A non-trivial fundamental group signals the presence of non-decomposable freely acting elements in the space group, i.e. freely acting elements that cannot be written as a combination of non-freely acting elements. In the cases $\mathbb{Z}_2 \times \mathbb{Z}_4$ and $\mathbb{Z}_3 \times \mathbb{Z}_3$, the non-decomposable freely acting elements belong to the orbifolding group. On the other hand, for $\mathbb{Z}_2 \times \mathbb{Z}_2$ those elements are pure lattice translations in the cases C and D , while in the cases A they are both pure lattice translations and elements of the orbifolding group.

In the context of heterotic compactifications, the phenomenologically appealing feature of non-local GUT symmetry breaking is due to the presence of non-decomposable freely acting space group elements with a non-trivial gauge embedding. In total we find 31 affine classes based on Abelian point groups with non-trivial fundamental groups. Their phenomenology will be studied elsewhere.

5.5.2 Non-Abelian toroidal orbifolds

Six-dimensional orbifolds with non-Abelian point groups have not been studied systematically up to now and the literature is limited to examples only [37, 44, 28, 23, 41].

Our classification results in 35 point groups with $\mathcal{N} = 1$ SUSY and three cases with $\mathcal{N} = 2$ SUSY. Next, we have classified all \mathbb{Z} - and affine classes. It turns out that there are in total 331 inequivalent space groups with non-Abelian point group and $\mathcal{N} = 1$ SUSY and 27 inequivalent space groups with non-Abelian point group and $\mathcal{N} = 2$. Most of them were unknown before. The results are summarized in tables 5.6 and 5.7 of the original publication [25], together with the discussion of a particular example, \mathbb{T}^6/D_6 ; and the full details can be found in Appendix C.2 there.

The results presented in this chapter were used in a follow-up study of non-Abelian orbifolds by two of the authors of the original publication in [24].

5.6 Summary and discussion

We have classified all symmetric orbifolds that give $\mathcal{N} \geq 1$ supersymmetry in four dimensions. Our main results are as follows:

1. In total we find 60 Q-classes (point groups) that lead to $\mathcal{N} \geq 1$ SUSY.

2. These \mathbb{Q} -classes decompose in

- 22 with an Abelian point group with one or two generators, i.e. \mathbb{Z}_N or $\mathbb{Z}_N \times \mathbb{Z}_M$, out of which 17 lead to exactly $\mathcal{N} = 1$ SUSY, and
- 38 with a non-Abelian point group with two or three generators, such as S_3 or $\Delta(216)$, out of which 35 lead to exactly $\mathcal{N} = 1$ SUSY.

That is, there are 52 \mathbb{Q} -classes that can lead to models yielding the supersymmetric standard model.

As we have explained in detail, \mathbb{Q} -classes (or point groups) can come with inequivalent lattices, classified by the so-called \mathbb{Z} -classes. In the traditional orbifold literature, \mathbb{Z} -classes are given by Lie lattices and a given choice fixes an orbifold geometry. However, as we have pointed out, not all lattices can be described by Lie lattices.

Our results on \mathbb{Q} -classes potentially relevant for supersymmetric model building are as follows.

3. We find that there are 186 \mathbb{Z} -classes, or, in other words, orbifold geometries that lead to $\mathcal{N} \geq 1$ SUSY.

4. These \mathbb{Z} -classes decompose in

- 71 with an Abelian point group, out of which 60 lead to exactly $\mathcal{N} = 1$ SUSY, and
- 115 with a non-Abelian point group, out of which 108 lead to exactly $\mathcal{N} = 1$ SUSY.

Furthermore, space groups can be extended by so-called roto-translations, a combination of a twist and a (non-lattice) translation. We provide a full classification of all roto-translations in terms of affine classes, which are, as we discuss, the most suitable objects to classify inequivalent space groups.

5. We find 520 affine classes that lead to $\mathcal{N} \geq 1$ SUSY.

6. These affine classes decompose in

- 162 with an Abelian point group, out of which 138 lead to exactly $\mathcal{N} = 1$ SUSY, and
- 358 with a non-Abelian point group, out of which 331 lead to exactly $\mathcal{N} = 1$ SUSY.

An important aspect of our classification is that we provide the data for all 138 space groups with Abelian point group and $\mathcal{N} = 1$ SUSY required to construct the corresponding models with the C++ orbifolder [46]. Among other things, this allows one to obtain a statistical survey of the properties of the models, which has so far only been performed for the \mathbb{Z}_6 -II orbifold [42].

Our classification also has conceivable importance for phenomenology. For instance, one of the questions is how the ten-dimensional gauge group (i.e. $E_8 \times E_8$ or $SO(32)$) of the heterotic string gets broken by orbifolding. In most of the models discussed so far, the larger symmetry gets broken locally at some fixed point. Yet it has been argued that ‘non-local’ GUT symmetry breaking, as utilized in the context of smooth compactifications of the heterotic string [6, 9, 8, 2], has certain phenomenological advantages [33, 1]. Explicit MSSM candidate models, based on the DW classification, featuring non-local GUT breaking have been constructed recently [4, 38]. As we have seen, there are 31 affine classes of space groups, based on the \mathbb{Q} -classes $\mathbb{Z}_2 \times \mathbb{Z}_2$, $\mathbb{Z}_2 \times \mathbb{Z}_4$ and $\mathbb{Z}_3 \times \mathbb{Z}_3$, that lead to an orbifold with a non-trivial fundamental group, thus allowing us to introduce a Wilson line that breaks the GUT symmetry. In other words, we have identified a large set of geometries that can give rise to non-local GUT breaking. This might also allow for a dynamical stabilization of some of the moduli in the early universe, similar as in toroidal compactifications [7].

In this study, we have focused on symmetric toroidal orbifolds, which have a rather clear geometric interpretation, such that crystallographic methods can be applied in a straightforward way. We have focused on the geometrical aspects. On the other hand, it is known that background fields, i.e. the so-called discrete Wilson lines [36] and discrete torsion [53, 54, 52, 29, 50], play a crucial role in model building. It will be interesting to work out the conditions on such background fields in the geometries of our classification. Further, it is, of course, clear that there are other orbifolds, such as T-folds [34, 16], asymmetric and/or non-toroidal orbifolds, whose classification is beyond the scope of this study. Let us also mention, we implicitly assumed that the radii are away from the self-dual point. As we are using crystallographic methods our classification strategy is independent of this assumption. Still, it might be interesting to study what happens if one sends one or more T -moduli to the self-dual values. In this case one may make contact with the free fermionic formulation, where also interesting models have been constructed [15]. In addition, our results may also be applied to compactifications of type II string theory on orientifolds (see e.g. [30, 22, 31] for some interesting models and [5] for a review).

Appendices

5.A Details on lattices

5.A.1 Bravais types and form spaces

One can classify lattices by the symmetry groups they obey. This is the concept of Bravais equivalent lattices. In more detail, denote the symmetry group of some lattice Λ as $G \subset GL(n, \mathbb{Z})$. Obviously, the point group $P \subset G$, is a subgroup of

it. Now, if two lattices give rise to the same finite unimodular group G , we call them Bravais equivalent. This equivalence generates a finite number of Bravais types of lattices for every dimension n . They have been classified for dimensions up to six [49].

The interesting task would now be to decide which Bravais type a given lattice belongs to. This can be done using the notion of form spaces [47]. The form space $\mathcal{F}(G)$ of some finite group $G \subset \mathrm{GL}(n, \mathbb{Z})$ is defined as the vector space of all symmetric matrices left invariant by G , i.e.

$$\mathcal{F}(G) = \{F \in \mathbb{R}_{\mathrm{sym}}^{n \times n} \mid g^T F g = F \text{ for all } g \in G\}. \quad (5.35)$$

On the other hand, we define the Gram matrix of the lattice basis $\mathbf{e} = \{\mathbf{e}_1, \dots, \mathbf{e}_n\}$ as

$$\mathrm{Gr}(\mathbf{e})_{ij} = (\mathbf{e}_i, \mathbf{e}_j) = (B_{\mathbf{e}}^T B_{\mathbf{e}})_{ij}, \quad (5.36)$$

where the parentheses $(\mathbf{e}_i, \mathbf{e}_j)$ denote the standard scalar product. By definition, the Gram matrix is a symmetric, positive definite matrix. Under a change of lattice basis, represented by a unimodular matrix M , the Gram matrix changes as $M^T \mathrm{Gr}(\mathbf{e}) M$, c.f. Section 5.2.2. By contrast, elements of the point group leave the Gram matrix invariant, i.e. for $\vartheta \in P$

$$\mathrm{Gr}(\mathbf{e}) \xrightarrow{\vartheta} \vartheta^T \mathrm{Gr}(\mathbf{e}) \vartheta = \mathrm{Gr}(\mathbf{e}). \quad (5.37)$$

Hence, a form space is in direct correspondence to a Bravais type of lattice, i.e. every lattice Λ has a basis $\mathbf{e} = \{\mathbf{e}_1, \dots, \mathbf{e}_n\}$ such that its Gram matrix $\mathrm{Gr}(\mathbf{e})$ is an element of the form space of a finite subgroup P of $\mathrm{GL}(n, \mathbb{Z})$, i.e. $\mathrm{Gr}(\mathbf{e}) \in \mathcal{F}(P)$ [10]. But in order to see that one lattice belongs to a given form space, it needs to be in this special basis, which is canonically chosen to be the so-called shortest possible basis for that lattice [10]. Fortunately, algorithms for precisely that task do exist, cf. e.g. [43] (though one should be careful: the shortest basis of a lattice is in general not unique).

Note that physically the Gram matrix is the metric of the torus defined by the lattice Λ and the dimension of the form space $\mathcal{F}(P)$ is exactly the number of (untwisted) moduli the orbifold offers.

Let us consider an example in two dimensions. Take the point group defined by

$$P = \{\mathbb{1} = \vartheta^2, \vartheta\} \cong \mathbb{Z}_2 \quad \text{with} \quad \vartheta = \begin{pmatrix} 1 & 0 \\ 0 & -1 \end{pmatrix}. \quad (5.38)$$

It leaves invariant the form space

$$\mathcal{F}(P) = \begin{pmatrix} a & 0 \\ 0 & b \end{pmatrix}. \quad (5.39)$$

That form space corresponds to the Bravais type called p-rectangular lattice (cf. Appendix 5.A.3), consisting of two arbitrarily long, orthogonal vectors.

5.A.2 Introducing an additional shift

DW [21] starts with an orthonormal lattice in six dimensions. Then, in a second step, additional shifts, which are linear combinations of the (orthonormal) lattice vectors with rational coefficients, are included in the space group. As we have seen in the second example in Section 5.3.4, those additional shifts can be incorporated to the lattice itself. Here we show in detail how to transform the space group accordingly.

The perhaps most elegant procedure is to perform a change of basis, but using transformations from $\text{GL}(n, \mathbb{Q})$. Hence, we are selecting a different \mathbb{Z} -class from the same \mathbb{Q} -class, cf. Section 5.3. Let us list the necessary steps and illustrate them with an example:

1. The additional shift is a linear combination with rational coefficients of some of the lattice vectors. Exchange one of the old lattice vectors (that appears in the linear combination) by the new additional shift.
2. Write the transformation matrix M : start with the identity matrix and substitute the column corresponding to the exchanged vector by the coefficients of the linear combination.
3. Transform your space group using M accordingly: see Equation (5.4) and Equation (5.5).
4. (Optional) In order to see the geometry more clearly, one can perform a basis reduction (e.g. using the LLL algorithm, cf. [43]), which is a transformation from $\text{GL}(n, \mathbb{Z})$.

As an example, take the $\mathbb{Z}_2 \times \mathbb{Z}_2$ model named (1-1) in DW [21], which consists of an orthogonal lattice (p-cubic) with orthonormal basis \mathbf{e} and an additional shift

$$\boldsymbol{\tau} = \frac{1}{2}(\mathbf{e}_2 + \mathbf{e}_4 + \mathbf{e}_6). \quad (5.40)$$

We will restrict the discussion to the three-dimensional (sub-)lattice Λ spanned by the basis $\mathbf{e} = \{\mathbf{e}_2, \mathbf{e}_4, \mathbf{e}_6\}$.

The basis matrix, Gram matrix and point group generators read

$$B_{\mathbf{e}} = \begin{pmatrix} 1 & 0 & 0 \\ 0 & 1 & 0 \\ 0 & 0 & 1 \end{pmatrix}, \quad \text{Gr}(\mathbf{e}) = \begin{pmatrix} 1 & 0 & 0 \\ 0 & 1 & 0 \\ 0 & 0 & 1 \end{pmatrix}, \quad (5.41a)$$

$$\vartheta_{\mathbf{e}} = \begin{pmatrix} 1 & 0 & 0 \\ 0 & -1 & 0 \\ 0 & 0 & -1 \end{pmatrix}, \quad \omega_{\mathbf{e}} = \begin{pmatrix} -1 & 0 & 0 \\ 0 & 1 & 0 \\ 0 & 0 & -1 \end{pmatrix}. \quad (5.41b)$$

Let us follow the steps described above:

1. We choose to exchange the 3rd (originally 6th) vector for the additional shift: the new basis \mathfrak{f} is spanned by $\mathfrak{f} = \{\mathbf{e}_2, \mathbf{e}_4, \boldsymbol{\tau}\}$. Notice that \mathfrak{f} is not a basis of the lattice Λ , but one of a new, different lattice Σ .
2. In accordance with our choice, the transformation matrix is

$$M = \begin{pmatrix} 1 & 0 & 1/2 \\ 0 & 1 & 1/2 \\ 0 & 0 & 1/2 \end{pmatrix}. \quad (5.42)$$

3. We perform the transformation using M . For the new lattice Σ in the new basis \mathfrak{f} , the quantities we are interested in look like

$$B_{\mathfrak{f}} = \begin{pmatrix} 1 & 0 & 1/2 \\ 0 & 1 & 1/2 \\ 0 & 0 & 1/2 \end{pmatrix}, \quad \text{Gr}(\mathfrak{f}) = \begin{pmatrix} 1 & 0 & 1/2 \\ 0 & 1 & 1/2 \\ 1/2 & 1/2 & 3/4 \end{pmatrix}, \quad (5.43a)$$

$$\vartheta_{\mathfrak{f}} = \begin{pmatrix} 1 & 0 & 1 \\ 0 & -1 & 0 \\ 0 & 0 & -1 \end{pmatrix}, \quad \omega_{\mathfrak{f}} = \begin{pmatrix} -1 & 0 & 0 \\ 0 & 1 & 1 \\ 0 & 0 & -1 \end{pmatrix}. \quad (5.43b)$$

4. Next, we perform a LLL reduction, which is a change of basis to a reduced one \mathfrak{r} , and transform the point group elements accordingly,

$$B_{\mathfrak{r}} = \begin{pmatrix} 1/2 & 1/2 & -1/2 \\ 1/2 & -1/2 & 1/2 \\ 1/2 & -1/2 & -1/2 \end{pmatrix}, \quad \text{Gr}(\mathfrak{r}) = \frac{1}{4} \begin{pmatrix} 3 & -1 & -1 \\ -1 & 3 & -1 \\ -1 & -1 & 3 \end{pmatrix}, \quad (5.44a)$$

$$\vartheta_{\mathfrak{r}} = \begin{pmatrix} 0 & 1 & -1 \\ 1 & 0 & -1 \\ 0 & 0 & -1 \end{pmatrix}, \quad \omega_{\mathfrak{r}} = \begin{pmatrix} 0 & -1 & 1 \\ 0 & -1 & 0 \\ 1 & -1 & 0 \end{pmatrix}. \quad (5.44b)$$

Last, we compare the Gram matrix $\text{Gr}(\mathfrak{r})$ with Table 5.6. We see that introducing the additional shift $\boldsymbol{\tau}$ into the p-cubic lattice is equivalent to work with the appropriately transformed point group in an i-cubic lattice.

A remark is in order. The form space left invariant by the $\mathbb{Z}_2 \times \mathbb{Z}_2$ point group in the (reduced) basis of Equation (5.44) is

$$\mathcal{F}(P) = \begin{pmatrix} a & b & c \\ b & a & -a-b-c \\ c & -a-b-c & a \end{pmatrix}. \quad (5.45)$$

This form space is the one of a three-parametric, i-orthogonal lattice, which contains as possible realizations the i-cubic and the f-cubic lattices (both one-parametric, see table 5.6). Therefore, model (1-1) in [21] corresponds to model A_4 of Förste et al. [26], i.e. to the Lie lattice $\text{SU}(4) \times \text{SU}(2)^3$ where the $\text{SU}(4)$ part is an f-cubic lattice, see Table 5.5.

5.A.3 Bravais types and Lie lattices

It is common in the string-orbifold literature to describe lattices as root lattices of (semi-simple) Lie algebras. On the one hand, this makes it easy to identify the point group, i.e. a discrete subgroup of $SU(3)$, using Weyl reflections and the Coxeter element. However, we find this practice to be problematic for at least three different reasons:

Redundancies

A root lattice is the lattice spanned by the simple roots of a certain (semi-simple) Lie algebra. Even if the simple roots of two non-equivalent (semi-simple) Lie algebras are different, the lattices they span might not. For example, the lattices spanned by the root systems of $SU(3)$ and G_2 are the same (see Figure 5.5). Some more examples are provided in Table 5.6.

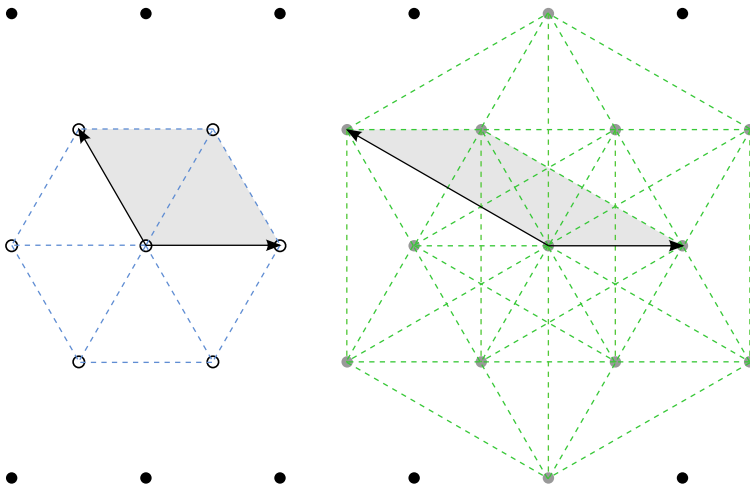


Figure 5.5: The hexagonal lattice: the lines on the left form the $SU(3)$ root system, and the lines on the right form the G_2 root system. Simple roots are also indicated with solid arrows, as well as the fundamental cells (shaded).

Missing lattices

When considering the redundancy of root lattices, one might think that there are more root lattices than types of lattices and that the situation could be resolved by introducing some clever convention to avoid this overcounting. But the problem exists in the other direction too: the set of all possible root lattices does not exhaust the whole family of Bravais types, i.e. there are Bravais types of lattices which are not generated by any root system. The lowest dimension in which this

occurs is three and the most basic example is the body centered cubic lattice, also known as bcc or i-cubic to crystallographers (see Table 5.6). The bcc lattice is a cubic lattice with an additional lattice point in the center of the fundamental cell. Its only free parameter is the size of the system (e.g. the edge length of the cube). One possible way to convince oneself that there is no root lattice that can generate this Bravais lattice is taking every rank three root lattice and calculating which Bravais lattice it generates. We find that the i-cubic lattice has no description as root lattice (see Table 5.6).

Continuous parameters

Every Bravais type allows for a set of continuous deformations which conserve its symmetries. Those deformations are encoded and made explicit in the form space that defines that particular Bravais type (cf. Appendix 5.A.1). The form space tells us how many deformation parameters one Bravais type allows for, and what is the effect of them (to change lengths of or angles between basis vectors). The realization of that freedom in the context of root lattices is very limited: lattices of Lie algebras allow for just one parameter, the size of the system; and if one includes semi-simple Lie algebras (direct products of simple ones), one can choose different sizes for different sublattices, but never the angles between vectors, which are fixed to a limited set of values. So, for example, a two-dimensional oblique lattice, in which the angle between the basis vectors is arbitrary, could never be unambiguously expressed in terms of Lie root lattices.

In conclusion, the language of root lattices is incomplete and ambiguous, and is lacking geometrical insight with respect to the language of Bravais types and form spaces, which is, therefore, the one used in this chapter.

Nevertheless, in order to justify some of the matchings between our classification of space groups and the ones already existing in the literature, we present in Table 5.6 a classification of all of the Bravais types of lattices in 1, 2 and 3 dimensions, together with their equivalent root lattices, if there are any. There, in order to overcome the discussed ambiguities in the root lattice language, some conventions have been used:

- \oplus means orthogonal product. Unspecified products should be understood orthogonal.
- \odot means free-angle product. The scalar product of the roots is indicated as a subindex. Notice that in the cases in which we have used this product there is actually no equivalent Lie lattice description: a non-orthogonal product of semi-simple Lie algebras is not a semi-simple Lie algebra. These possibilities are written in italics.
- \leftarrow means a product with the leftmost factor.
- Equal subindices mean equal length of the roots or equal scalar products.

5.A Details on lattices

- A subindex in an algebra whose simple roots are of different length stands for the squared length of the shortest simple root, e.g. $G_{2,a}$ means that the shortest simple root of G_2 has length squared a .

Gram matrix	lattice name		Lie algebra notation
1 dimension			
(a)	Ruler	r	$SU(2)$
2 dimensions			
$\begin{pmatrix} a & 0 \\ & a \end{pmatrix}$	Square	tp	$SO(5), SU(2)_a \oplus SU(2)_a$
$\begin{pmatrix} a & \pm a/2 \\ & a \end{pmatrix}$	Hexagonal	hp	$SU(3)_a, G_{2,a}$
$\begin{pmatrix} a & 0 \\ & b \end{pmatrix}$	p-Rectangular	op	$SU(2)_a \oplus SU(2)_b$
$\begin{pmatrix} a & b \\ & a \end{pmatrix}$	c-Rectangular	oc	$SU(2)_a \odot_b SU(2)_a$
$\begin{pmatrix} a & c \\ & b \end{pmatrix}$	Oblique	mp	$SU(2)_a \odot_c SU(2)_b$
3 dimensions			
$\begin{pmatrix} a & 0 & 0 \\ & a & 0 \\ & & a \end{pmatrix}$	p-Cubic	cP	$SO(7), SU(2)_a \oplus SU(2)_a \oplus SU(2)_a$
$\begin{pmatrix} a & a/2 & a/2 \\ & a & a/2 \\ & & a \end{pmatrix}$	f-Cubic	cF	$SU(4), Sp(6)$
$\begin{pmatrix} a & -a/3 & -a/3 \\ & a & -a/3 \\ & & a \end{pmatrix}$	i-Cubic	cI	(none)
$\begin{pmatrix} a & \pm a/2 & 0 \\ & a & 0 \\ & & b \end{pmatrix}$	p-Hexagonal	hP	$[SU(3)_a \text{ or } G_{2,a}] \oplus SU(2)_b$
$\begin{pmatrix} a & b & b \\ & a & b \\ & & a \end{pmatrix}$	r-Hexagonal	hR	$SU(2)_a \odot_b SU(2)_a \odot_b SU(2)_a \odot_b \leftrightarrow$
$\begin{pmatrix} a & 0 & 0 \\ & a & 0 \\ & & b \end{pmatrix}$	p-Tetragonal	tP	$[SU(2)_a \oplus SU(2)_a \text{ or } SO(5)] \oplus SU(2)_b$
$\begin{pmatrix} a+2b & -a & -b \\ & a+2b & -b \\ & & a+2b \end{pmatrix}$	i-Tetragonal	tI	(no simple expr.)
$\begin{pmatrix} a & 0 & 0 \\ & b & 0 \\ & & c \end{pmatrix}$	p-Orthorhombic	oP	$SU(2)_a \oplus SU(2)_b \oplus SU(2)_c$
$\begin{pmatrix} a & c & 0 \\ & a & 0 \\ & & b \end{pmatrix}$	c-Orthorhombic	oC	$SU(2)_a \odot_c SU(2)_a \oplus SU(2)_b$
$\begin{pmatrix} a+b & a & b \\ & a+c & c \\ & & b+c \end{pmatrix}$	f-Orthorhombic	oF	(no simple expr.)
$\begin{pmatrix} a+b+c & -a & -b \\ & a+b+c & -c \\ & & a+b+c \end{pmatrix}$	i-Orthorhombic	oI	(no simple expr.)
$\begin{pmatrix} a & c & 0 \\ & b & 0 \\ & & d \end{pmatrix}$	p-Monoclinic	mP	$SU(2)_a \odot_c SU(2)_b \oplus SU(2)_d$

continued ...

Gram matrix	lattice name	Lie algebra notation
$\begin{pmatrix} a & c & d \\ & a & d \\ & & b \end{pmatrix}$	c-Monoclinic mC	$SU(2)_a \odot_c SU(2)_a \odot_d SU(2)_b \odot_d \leftrightarrow$
$\begin{pmatrix} a & d & f \\ & b & e \\ & & c \end{pmatrix}$	Triclinic aP	$SU(2)_a \odot_d SU(2)_b \odot_e SU(2)_c \odot_f \leftrightarrow$

Table 5.6: List of Bravais types in 1, 2 and 3 dimensions, together with possible root lattice expressions. The following prefixes and suffixes are used for the lattice names: p primitive, c centered (in 2D) or base-centered (in 3D), f face-centered, i body-centered, and r rhombohedral.

In general, Bravais types with two or more parameters in the form space contain as specific cases other types with a lower number of parameters. For example, if we set the off diagonal parameter to zero in the two-dimensional oblique lattice (mp) (i.e. we take the basis vectors to be orthogonal), we get a p-rectangular (op) lattice. If we set now the diagonal elements of the form space to be equal (i.e. we take the basis vectors to have equal length), we get a square lattice (tp). These three lattices form the embedding chain $tp \leftarrow op \leftarrow mp$.

A graph containing all of the existing embeddings of that kind in two and three dimensions can be seen in Figure 5.6. For further information about this topic, the standard reference is [32].

5.B Two-dimensional orbifolds

In order to illustrate some of the concepts addressed in this chapter, we reproduce here the list of all possible two-dimensional space groups, also known as *wallpaper groups*. They are well-known, and their classification can be found for instance in [10].

The possible orders m of (irreducible) point group elements in n dimensions are given by the equation

$$\phi(m) \leq n, \quad (5.46)$$

where ϕ is the Euler ϕ -function. For dimension two, this leaves only elements with order in $\{1, 2, 3, 4, 6\}$ as possible point group elements. In six dimensions, this gets extended to $\{1, 2, 3, 4, 5, 6, 7, 8, 9, 10, 12, 14, 18\}$. Nevertheless, in dimensions $n \geq 2$, one can find point group elements with order m such that $\phi(m) > n$. This can be realized by building a point group element as the direct sum of two point group elements of dimensions that add up to n . In that case, the order of the point group element would obviously be the least common multiple of the orders of the factors. For example, in six dimensions there exist point groups with elements of order 30, which are a direct sum of a four-dimensional order 10 element and a two-dimensional order 3 element.

As discussed in Section 5.3, one can classify the 17 two-dimensional space groups by their \mathbb{Q} -classes. Those can be found in Table 5.7. There, D_n is the

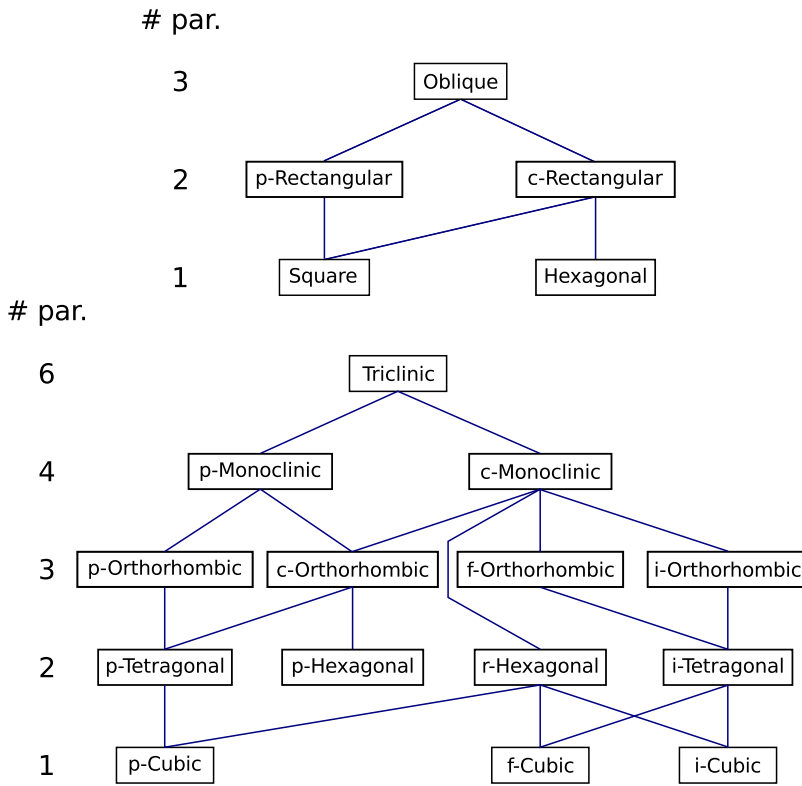


Figure 5.6: Graph of Bravais types embeddings in 2D and 3D.

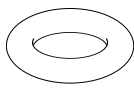
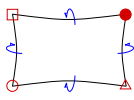


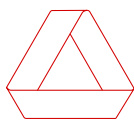
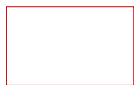
dihedral group of order $2n$ and S_n is the symmetric group of order $n!$. In Table 5.8 the specific information of every affine class is shown: the \mathbb{Q} -, \mathbb{Z} - and affine class to which they belong, its Bravais type of lattice (cf. Table 5.6), its orbifolding group generators in augmented matrix notation and a name, description and image of its topology. The augmented matrix of some element $g_{\epsilon} = (\vartheta_{\epsilon}, \lambda_i e_i) \in S$ is given by

$$g_{\epsilon} = \left(\begin{array}{c|c} \vartheta_{\epsilon} & \lambda_i \\ \hline 0 & 1 \end{array} \right), \quad (5.47)$$

using the lattice basis ϵ . This matrix acts on an augmented vector $(\mathbf{x}, 1)$ by simple matrix-vector multiplication.

label of Q-class	# of Z-classes	# of affine classes
id	1	1
\mathbb{Z}_2 -I	1	1
\mathbb{Z}_2 -II	2	3
$\mathbb{Z}_2 \times \mathbb{Z}_2 \cong D_2$	2	4
\mathbb{Z}_4	1	1
$\mathbb{Z}_2 \times \mathbb{Z}_4 \cong D_4$	2	2
\mathbb{Z}_3	1	1
$\mathbb{Z}_2 \times \mathbb{Z}_3 \cong S_3 \cong D_3$	2	2
\mathbb{Z}_6	1	1
$\mathbb{Z}_2 \times \mathbb{Z}_6 \cong D_6$	1	1

Table 5.7: Q-classes in two dimensions.

Q-Z-aff. class Lattice	Generators	Name & description	Image
id-1-1 Oblique		Torus Manifold	
\mathbb{Z}_2 -I-1-1 Oblique	$\left(\begin{array}{cc c} -1 & 0 & 0 \\ 0 & -1 & 0 \\ 0 & 0 & 1 \end{array} \right)$	Pillow Orbifold, 4 singularities with cone-angle π	
\mathbb{Z}_2 -II-1-1 p-Rectangular	$\left(\begin{array}{cc c} 1 & 0 & 0 \\ 0 & -1 & 0 \\ 0 & 0 & 1 \end{array} \right)$	Pipe Manifold, 2 boundaries	
\mathbb{Z}_2 -II-1-2 p-Rectangular	$\left(\begin{array}{cc c} 1 & 0 & 1/2 \\ 0 & -1 & 0 \\ 0 & 0 & 1 \end{array} \right)$	Klein bottle Manifold, non-orientable	
\mathbb{Z}_2 -II-2-1 c-Rectangular	$\left(\begin{array}{cc c} 0 & 1 & 0 \\ 1 & 0 & 0 \\ 0 & 0 & 1 \end{array} \right)$	Möbius strip Manifold, non-orientable, 1 boundary	
$\mathbb{Z}_2 \times \mathbb{Z}_2$ -1-1 p-Rectangular	$\left(\begin{array}{cc c} -1 & 0 & 0 \\ 0 & -1 & 0 \\ 0 & 0 & 1 \end{array} \right), \left(\begin{array}{cc c} 1 & 0 & 0 \\ 0 & -1 & 0 \\ 0 & 0 & 1 \end{array} \right)$	Rectangle Manifold, 1 boundary	
			continued ...

5.B Two-dimensional orbifolds

\mathbb{Q} - \mathbb{Z} -aff. class Lattice	Generators	Name & description	Image
$\mathbb{Z}_2 \times \mathbb{Z}_2$ -1-2 p-Rectangular	$\left(\begin{array}{c c} -1 & 0 \\ \hline 0 & -1 \\ \hline 0 & 0 \\ \hline & 1 \end{array} \right), \left(\begin{array}{c c} 1 & 0 \\ \hline 0 & -1 \\ \hline 0 & 0 \\ \hline & 1/2 \end{array} \right)$	Cut pillow Orbifold, 2 singularities with cone-angle π , 1 boundary	
$\mathbb{Z}_2 \times \mathbb{Z}_2$ -1-3 p-Rectangular	$\left(\begin{array}{c c} -1 & 0 \\ \hline 0 & -1 \\ \hline 0 & 0 \\ \hline & 1 \end{array} \right), \left(\begin{array}{c c} 1 & 0 \\ \hline 0 & -1 \\ \hline 0 & 0 \\ \hline & 1/2 \end{array} \right)$	Cross-cap pillow Orbifold, 2 singularities with cone-angle π	
$\mathbb{Z}_2 \times \mathbb{Z}_2$ -2-1 c-Rectangular	$\left(\begin{array}{c c} -1 & 0 \\ \hline 0 & -1 \\ \hline 0 & 0 \\ \hline & 1 \end{array} \right), \left(\begin{array}{c c} 0 & 1 \\ \hline 1 & 0 \\ \hline 0 & 0 \\ \hline & 1 \end{array} \right)$	Jester's hat Orbifold, 1 singularity with cone-angle π , 1 boundary	
\mathbb{Z}_4 -1-1 Square	$\left(\begin{array}{c c} 0 & -1 \\ \hline 1 & 0 \\ \hline 0 & 0 \\ \hline & 1 \end{array} \right)$	Triangle pillow Orbifold, 2 singularities with cone-angle $\pi/2$, 1 singularity with cone-angle π	
$\mathbb{Z}_2 \times \mathbb{Z}_4$ -1-1 Square	$\left(\begin{array}{c c} 1 & 0 \\ \hline 0 & -1 \\ \hline 0 & 0 \\ \hline & 1 \end{array} \right), \left(\begin{array}{c c} 0 & -1 \\ \hline 1 & 0 \\ \hline 0 & 0 \\ \hline & 1 \end{array} \right)$	Triangle Manifold, one boundary, 1 angle of $\pi/2$ and 2 of $\pi/4$	
$\mathbb{Z}_2 \times \mathbb{Z}_4$ -1-2 Square	$\left(\begin{array}{c c} 1 & 0 \\ \hline 0 & -1 \\ \hline 0 & 0 \\ \hline & 1 \end{array} \right), \left(\begin{array}{c c} 0 & -1 \\ \hline 1 & 0 \\ \hline 0 & 0 \\ \hline & 1 \end{array} \right)$	Jester's hat Orbifold, 1 singularity with cone-angle $\pi/2$, 1 boundary	
\mathbb{Z}_3 -1-1 Hexagonal	$\left(\begin{array}{c c} 0 & -1 \\ \hline 1 & -1 \\ \hline 0 & 0 \\ \hline & 1 \end{array} \right)$	Triangle pillow Orbifold, 3 singularities with cone-angle $2\pi/3$	
$\mathbb{Z}_2 \times \mathbb{Z}_3$ -1-1 Hexagonal	$\left(\begin{array}{c c} 0 & -1 \\ \hline -1 & 0 \\ \hline 0 & 0 \\ \hline & 1 \end{array} \right), \left(\begin{array}{c c} 0 & -1 \\ \hline 1 & -1 \\ \hline 0 & 0 \\ \hline & 1 \end{array} \right)$	Triangle Manifold, 3 boundary, all angles $\pi/3$	
$\mathbb{Z}_2 \times \mathbb{Z}_3$ -2-1 Hexagonal	$\left(\begin{array}{c c} 0 & 1 \\ \hline 1 & 0 \\ \hline 0 & 0 \\ \hline & 1 \end{array} \right), \left(\begin{array}{c c} 0 & -1 \\ \hline 1 & -1 \\ \hline 0 & 0 \\ \hline & 1 \end{array} \right)$	Jester's hat Orbifold, 1 singularity with cone-angle $2\pi/3$, 1 boundary	

continued ...

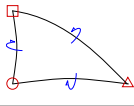
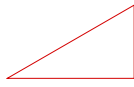
\mathbb{Q} - \mathbb{Z} -aff. class Lattice	Generators	Name & description	Image
\mathbb{Z}_6^{-1-1} Hexagonal	$\left(\begin{array}{cc c} 1 & -1 & 0 \\ 1 & 0 & 0 \\ 0 & 0 & 1 \end{array} \right)$	Triangle pillow Orbifold, 3 singularities with cone-angles $2\pi/3$, $\pi/3$ and π	
$\mathbb{Z}_2 \times \mathbb{Z}_6^{-1-1}$ Hexagonal	$\left(\begin{array}{cc c} 0 & 1 & 0 \\ 1 & 0 & 0 \\ 0 & 0 & 1 \end{array} \right), \left(\begin{array}{cc c} 1 & -1 & 0 \\ 1 & 0 & 0 \\ 0 & 0 & 1 \end{array} \right)$	Triangle Manifold, 1 boundary, with angles $\pi/2$, $\pi/3$ and $\pi/6$	

Table 5.8: List of all possible two-dimensional orbifolds. \mathbb{Q} -classes are separated by double lines.

Sometimes it is of interest to know the fundamental groups of the resulting orbifolds. Among the two-dimensional space groups, most of the fundamental groups are trivial with the following exceptions: the torus has a fundamental group of $(\mathbb{Z})^2$, the pipe and the Möbius strip \mathbb{Z} , the cross-cap pillow (a projective plane) \mathbb{Z}_2 and the Klein bottle's one is its own space group, with group structure

$$S = \{a^n b^m \mid m, n \in \mathbb{Z}, ba = a^{-1}b\} . \quad (5.48)$$

Bibliography

- [1] Archana Anandakrishnan and Stuart Raby. SU(6) GUT Breaking on a Projective Plane. *Nucl.Phys.*, B868:627–651, 2013, 1205.1228.
- [2] Lara B. Anderson, James Gray, Andre Lukas, and Eran Palti. Heterotic Line Bundle Standard Models. *JHEP*, 1206:113, 2012, 1202.1757.
- [3] D. Bailin and A. Love. Orbifold compactifications of string theory. *Phys. Rept.*, 315:285–408, 1999.
- [4] Michael Blaszczyk, Stefan Groot Nibbelink, Michael Ratz, Fabian Ruehle, Michele Trapletti, et al. A $\mathbb{Z}_2 \times \mathbb{Z}_2$ standard model. *Phys.Lett.*, B683:340–348, 2010, 0911.4905.
- [5] Ralph Blumenhagen, Boris Körs, Dieter Lüst, and Stephan Stieberger. Four-dimensional String Compactifications with D-Branes, Orientifolds and Fluxes. *Phys. Rept.*, 445:1–193, 2007, hep-th/0610327.
- [6] Vincent Bouchard and Ron Donagi. An SU(5) heterotic standard model. *Phys. Lett.*, B633:783–791, 2006, hep-th/0512149.
- [7] Robert H. Brandenberger and C. Vafa. Superstrings in the Early Universe. *Nucl.Phys.*, B316:391, 1989.

- [8] Volker Braun, Philip Candelas, Rhys Davies, and Ron Donagi. The MSSM Spectrum from (0,2)-Deformations of the Heterotic Standard Embedding. *JHEP*, 1205:127, 2012, 1112.1097.
- [9] Volker Braun, Yang-Hui He, Burt A. Ovrut, and Tony Pantev. A heterotic standard model. *Phys. Lett.*, B618:252–258, 2005, hep-th/0501070.
- [10] Brown, Buelow, Neubueser, Wondratchek, and Zassenhaus. *Crystallographic Groups of Four-Dimensional Space*. Wiley, 1978.
- [11] R. Brown and P. J. Higgins. The fundamental groupoid of the quotient of a Hausdorff space by a discontinuous action of a discrete group is the orbit groupoid of the induced action. *ArXiv Mathematics e-prints*, December 2002, arXiv:math/0212271.
- [12] Wilfried Buchmüller, Koichi Hamaguchi, Oleg Lebedev, and Michael Ratz. Supersymmetric standard model from the heterotic string. *Phys. Rev. Lett.*, 96:121602, 2006, hep-ph/0511035.
- [13] Wilfried Buchmüller, Koichi Hamaguchi, Oleg Lebedev, and Michael Ratz. Supersymmetric standard model from the heterotic string. II. *Nucl. Phys.*, B785:149–209, 2007, hep-th/0606187.
- [14] P. Candelas, Gary T. Horowitz, Andrew Strominger, and Edward Witten. Vacuum Configurations for Superstrings. *Nucl. Phys.*, B258:46–74, 1985.
- [15] G. B. Cleaver, A. E. Faraggi, and D. V. Nanopoulos. String derived MSSM and M-theory unification. *Phys. Lett.*, B455:135–146, 1999, hep-ph/9811427.
- [16] Cezar Condeescu, Ioannis Florakis, and Dieter Lüst. Asymmetric Orbifolds, Non-Geometric Fluxes and Non-Commutativity in Closed String Theory. *JHEP*, 1204:121, 2012, 1202.6366.
- [17] Jimmy Dillies. Toroidal orbifolds a la Vafa-Witten. *Adv.Theor.Math.Phys.*, 11:683–705, 2007, math/0609714.
- [18] Lance J. Dixon, Jeffrey A. Harvey, C. Vafa, and Edward Witten. Strings on orbifolds. *Nucl. Phys.*, B261:678–686, 1985.
- [19] Lance J. Dixon, Jeffrey A. Harvey, C. Vafa, and Edward Witten. Strings on orbifolds. 2. *Nucl. Phys.*, B274:285–314, 1986.
- [20] Ron Donagi and Alon E. Faraggi. On the number of chiral generations in $Z(2) \times Z(2)$ orbifolds. *Nucl. Phys.*, B694:187–205, 2004, hep-th/0403272.
- [21] Ron Donagi and Katrin Wendland. On orbifolds and free fermion constructions. *J.Geom.Phys.*, 59:942–968, 2009, 0809.0330.

- [22] Michael R. Douglas and Washington Taylor. The Landscape of intersecting brane models. *JHEP*, 0701:031, 2007, hep-th/0606109.
- [23] Sayipjamal Dulat and Katrin Wendland. Crystallographic orbifolds: Towards a classification of unitary conformal field theories with central charge $c = 2$. *JHEP*, 0006:012, 2000, hep-th/0002227.
- [24] Maximilian Fischer, Saul Ramos-Sanchez, and Patrick K. S. Vaudrevange. Heterotic non-Abelian orbifolds. *JHEP*, 1307:080, 2013, 1304.7742.
- [25] Maximilian Fischer, Michael Ratz, Jesus Torrado, and Patrick K.S. Vaudrevange. Classification of symmetric toroidal orbifolds. *JHEP*, 1301:084, 2013, 1209.3906.
- [26] Stefan Förste, Tatsuo Kobayashi, Hiroshi Ohki, and Kei-jiro Takahashi. Non-Factorisable $Z(2) \times Z(2)$ Heterotic Orbifold Models and Yukawa Couplings. *JHEP*, 0703:011, 2007, hep-th/0612044.
- [27] Stefan Förste, Hans Peter Nilles, Patrick K. S. Vaudrevange, and Akin Wingenter. Heterotic brane world. *Phys. Rev.*, D70:106008, 2004, hep-th/0406208.
- [28] Paul H. Frampton and Thomas W. Kephart. Classification of conformality models based on nonAbelian orbifolds. *Phys.Rev.*, D64:086007, 2001, hep-th/0011186.
- [29] Matthias R. Gaberdiel and Peter Kaste. Generalised discrete torsion and mirror symmetry for $G(2)$ manifolds. *JHEP*, 08:001, 2004, hep-th/0401125.
- [30] Florian Gmeiner, Ralph Blumenhagen, Gabriele Honecker, Dieter Lüst, and Timo Weigand. One in a billion: MSSM-like D-brane statistics. *JHEP*, 01:004, 2006, hep-th/0510170.
- [31] Florian Gmeiner and Gabriele Honecker. Millions of Standard Models on Z_6 -prime? *JHEP*, 07:052, 2008, 0806.3039.
- [32] Theo Hahn, editor. *International tables for crystallography*, volume A. Springer, 2005.
- [33] A. Hebecker and M. Trapletti. Gauge unification in highly anisotropic string compactifications. *Nucl. Phys.*, B713:173–203, 2005, hep-th/0411131.
- [34] C.M. Hull. A Geometry for non-geometric string backgrounds. *JHEP*, 0510:065, 2005, hep-th/0406102.
- [35] Luis E. Ibáñez, Jihn E. Kim, Hans Peter Nilles, and F. Quevedo. Orbifold compactifications with three families of $SU(3) \times SU(2) \times U(1)^{**n}$. *Phys. Lett.*, B191:282–286, 1987.

- [36] Luis E. Ibáñez, Hans Peter Nilles, and F. Quevedo. Orbifolds and Wilson lines. *Phys. Lett.*, B187:25–32, 1987.
- [37] Zurab Kakushadze, Gary Shiu, and S.H. Henry Tye. Asymmetric non-Abelian orbifolds and model building. *Phys.Rev.*, D54:7545–7560, 1996, hep-th/9607137.
- [38] Rolf Kappl, Bjoern Petersen, Stuart Raby, Michael Ratz, Roland Schieren, and Patrick K.S. Vaudrevange. String-derived MSSM vacua with residual R symmetries. *Nucl.Phys.*, B847:325–349, 2011, 1012.4574.
- [39] Tetsuji Kimura, Mitsuhsisa Ohta, and Kei-Jiro Takahashi. Type IIA orientifolds and orbifolds on non-factorizable tori. *Nucl.Phys.*, B798:89–123, 2008, 0712.2281.
- [40] Tatsuo Kobayashi and Noriyasu Ohtsubo. Geometrical aspects of Z_N orbifold phenomenology. *Int. J. Mod. Phys.*, A9:87–126, 1994.
- [41] Sebastian Konopka. Non-Abelian orbifold compactifications of the heterotic string, 2011.
<http://einrichtungen.ph.tum.de/T30e/research/theses/KonopkaDiplomarbeit.pdf>.
- [42] Oleg Lebedev, Hans Peter Nilles, Saul Ramos-Sánchez, Michael Ratz, and Patrick K. S. Vaudrevange. Heterotic mini-landscape (II): completing the search for MSSM vacua in a Z_6 orbifold. *Phys. Lett.*, B668:331–335, 2008, 0807.4384.
- [43] A. K. Lenstra, H. W. Lenstra, and L. Lovasz. Factoring polynomials with rational coefficients. *Mathematische Annalen*, 261:515–534, 1982. 10.1007/BF01457454.
- [44] Tomomi Muto. D-branes on three-dimensional nonAbelian orbifolds. *JHEP*, 9902:008, 1999, hep-th/9811258.
- [45] Hans Peter Nilles, Saúl Ramos-Sánchez, Michael Ratz, and Patrick K. S. Vaudrevange. From strings to the MSSM. *Eur. Phys. J.*, C59:249–267, 2009, 0806.3905.
- [46] Hans Peter Nilles, Saúl Ramos-Sánchez, Patrick K.S. Vaudrevange, and Akin Wingerter. The Orbifolder: A Tool to study the Low Energy Effective Theory of Heterotic Orbifolds. *Comput.Phys.Commun.*, 183:1363–1380, 2012, 1110.5229. 29 pages, web page <http://projects.hepforge.org/orbifolder/>.
- [47] J. Opgenorth, W. Plesken, and T. Schulz. Crystallographic algorithms and tables. *Acta Cryst. Sect. A*, 54, 1998.
- [48] W. Plesken. The carat computer package, 2008.
<http://wwb.math.rwth-aachen.de/carat/index.html>.

- [49] W. Plesken and W. Hanrath. The lattices of six-dimensional euclidean space. *Mathematics of computation*, 43:573–587, 1984.
- [50] Felix Plöger, Saul Ramos-Sánchez, Michael Ratz, and Patrick K. S. Vaudrevange. Mirage torsion. *JHEP*, 04:063, 2007, hep-th/0702176.
- [51] Saúl Ramos-Sánchez. Towards Low Energy Physics from the Heterotic String. *Fortsch.Phys.*, 10:907–1036, 2009, 0812.3560. Ph.D.Thesis (Advisor: H.P. Nilles).
- [52] Eric R. Sharpe. Discrete torsion. *Phys. Rev.*, D68:126003, 2003, hep-th/0008154.
- [53] Cumrun Vafa. Modular invariance and discrete torsion on orbifolds. *Nucl. Phys.*, B273:592, 1986.
- [54] Cumrun Vafa and Edward Witten. On orbifolds with discrete torsion. *J. Geom. Phys.*, 15:189–214, 1995, hep-th/9409188.

Summary

Part I

When the electro-magnetic radiation coming from the sky is observed at microwave wavelengths, one finds a mild background of radiation which is practically constant in all directions (once one removes the biggest foreground contributions, such as the radiation coming from our own galaxy). What is the origin of that radiation? When was it originated? When attempting to describe the current cosmological data with General Relativity, scientists of the early decades of the XX century found that the Universe must have been (and is) expanding for all of its life. As a gas that gets hotter when compressed, the Universe must have been much hotter in the past. So much that at some point electrons had so much energy that they preferred being detached from the atomic nuclei, streaming and scattering freely together with photons, forming what we call a *plasma*. Once the Universe's growth diluted some of this energy, the electrons fell to the nuclei to form atoms, and the photons were free to travel through space and reach us. They form the background radiation we can see today, and that we call Cosmic Microwave Background, or simply CMB.

When one carefully observes the CMB, the first feature that shows up is how strikingly constant it is across all the sky. This is certainly not what we would expect. On the one hand, two regions of the universe emitting a practically equal signal is an indication that they are in *equilibrium* – the hotter and colder regions have been exchanging energy until they were at the same temperature. On the other hand, according to the speed our Universe expands in our cosmological model, regions that are separated by more than a few degrees in the sky are so very far apart that they never had time, since the beginning of the Universe to the emission of the CMB, to exchange any energy at all. So how can they be in equilibrium?

This contradiction was resolved in the 80's with a crucial modification of the cosmological model: we assume that in the early instant of the Universe it underwent an explosively accelerated (near-exponential) expansion. Such an expansion would stretch a small patch with almost constant temperature to a region bigger than the amount of the Universe that we can see today. Therefore, what is far apart in the Universe today, was so close in the past that there was almost no

difference in temperature between these points. This explosive expansion stage was called *inflation*.

As the most stringent supporting evidence for inflation, the CMB also contains most of the information about inflation that we possess today. This information is found in some very small fluctuations in the CMB, ten thousand times smaller than the almost constant temperature of the CMB background. Those fluctuations originated when the explosive expansion turned small quantum random fluctuations on very small scales into differences of density of matter across big distances in the cosmos. If the fluctuations that we observe today were generated at very small scales, they must be well related to each other, or *correlated*. We characterise their correlation by averaging the difference in temperature over pairs of points in the sky separated by a certain angle. We call this average as a function of scale the *2-point correlation function* or *power spectrum*. If instead of having been generated very close to each other, the fluctuations were completely random and unrelated, those averages would be very close to zero. Instead, they are quite sizeable, and their precise properties can tell us much about the quantum origin of the fluctuations.

At the time of writing this thesis the Planck mission of the European Space Agency has made available its first batch of data, and we are waiting for the next and final release. Those data provide us with a very accurate measurement of the 2-point correlations of the CMB fluctuations, which is in agreement with that of previous experiments. In addition to that, the next data release is expected to contain a measurement of the 3-point correlation function or *bispectrum*, which is an average of the correlation between the fluctuations over three different points in the sky, instead of two. The 3-point correlation function, never measured before with sufficient precision, is of crucial importance for the study of inflation, since there is a specific prediction for it: if inflation occurred in the simplest way possible, we expect the 3-point correlations to be very close to zero, which corresponds to the initial fluctuations being Gaussian. Different, more complicated settings of inflation predict diverse and characteristic 3-point correlations. The moment is ripe, therefore, to test extensions of the simplest framework.

In the simplest model of inflation, the explosive expansion is caused by the presence of a single kind of *matter* in the universe, the *inflaton*, which possesses a negative pressure. In this thesis, we work under the assumption that the inflation, though dominant, was not alone – there were more species present, which appear to the inflation as a stiff background. When the inflation interacts with its background, the correlation functions of the CMB fluctuations at 2 and 3 points would possess small but distinctive features. By searching for those features in the CMB data, we can find out if the inflation evolved in such a non-trivial background, and even resolve the particular shape of it.

Since, as we stated, the 3-point correlation function of the Planck mission has not been released at the time of writing this thesis, we searched in the Planck data for features in the 2-point correlation function. After we found the best candidates, we computed the associated 3-point correlations that we expect to see

in the new data release of Planck, and left them as test for our simple extension of the simplest model of inflation. In addition, we enlarged our search to include Large Scale Structure (LSS) data, which also contains some information on inflation, since galaxies and clusters are the final outcome of primordial fluctuations. The LSS data confirmed the best candidates that we found in Planck's CMB sky.

Part II

With the recent discovery of the Higgs particle in the ATLAS and CMS experiments of the Large Hadron Collider (LHC), all of the main predictions of the Standard Model of Particle Physics have been fulfilled, and it can be considered *complete*. Nevertheless, there is a number of experimental and theoretical reasons that encourage us to attempt to extend it.

On the experimental side, one phenomenon has already been clearly observed that finds no explanation within the Standard Model: *neutrino oscillations*, i.e. how streaming neutrinos spontaneously change their *flavour* between the three possible ones. This phenomenon has been measured beyond doubt in different sources, from the stream of neutrinos coming from the Sun, to those generated at particle accelerators. This kind of behaviour is only possible for particles possessing a non-zero mass, while Standard Model neutrinos are necessarily massless particles. Any explanation for neutrino masses implies physics beyond the Standard Model.

The nature of Dark Matter also lacks an explanation within the Standard Model. The presence of Dark Matter is necessary to explain the cosmological and galactic dynamics of the Universe as we observe it (same for Dark Energy, which is not discussed here). Despite that fact, Dark Matter has never been directly observed in accelerators or astrophysical particle physics experiments. Therefore, little is known about the *Dark Matter particle* and its possible fitting in an extension of the Standard Model.

On the theoretical side, there exist several arguments. For starters, the mass of the Higgs particle, though not predicted by the Standard Model, is surprisingly low. The surprise comes from the fact that particles are made heavier through loop interactions with the particles they are coupled to. Since the Higgs field is coupled to all the fermions of the Standard Model, we would expect that they have driven its mass much higher. This suggests the existence of a symmetry that cancels such contributions. One possibility is introducing counterparts of the Standard Model particles with different spin but approximately equal mass. The difference in spin would automatically cancel the contributions to the Higgs mass, and, due to the mass of the new particles been approximately equal to those known, the new particles could possibly be observed at the LHC within the next years. We call that symmetry *Super-Symmetry* (SUSY), and we abbreviate it as MSSM, the *minimal possible SUSY extension to the Standard Model*.

SUSY has an additional consequence: it hints towards the unification of all fundamental forces operating at subatomic scale, i.e. electro-magnetic, *strong* and

weak forces. We call this speculative phenomenon *Grand Unification*, and any theory that describes it in detail is called *Grand Unification Theory* (GUT). GUT's would explain why the *hyper-charge*, one of the quantum numbers of the Standard Model particles, is in fact quantised. SUSY, combined with GUT, would also provide us with several candidate particles to constitute the Dark Matter that we observe (indirectly) in the Universe.

The MSSM possesses all the desired features mentioned above, but at the cost of introducing many new free parameters in the model. This makes it less predictive, which is never desirable for a physical model. In addition, it does not address the quantum nature of the remaining fundamental interaction: gravity. Those issues can be addressed assuming that the MSSM is embedded in String Theory. String Theory provides us with a well-defined description of quantum gravity, and, once the geometry and some properties of the theory have been chosen, all the phenomenology at all energy scales, including those that we can observe today, can be computed.

This is the case in particular of the setting considered in this thesis, Heterotic Strings compactified in Symmetric Toroidal Orbifolds, *compactification* meaning the assumption that the extra dimensions are finite and very small compared to the scales of Standard Model physics. In this theory, one only needs to specify the geometry of 6 extra dimensions, together with the effect of that geometry in the messengers of the fundamental interactions (in that case, a *rank-16* GUT): given that, the content and possible interactions of all fundamental particles are determined.

In this thesis, we perform a classification of all possible symmetric toroidal orbifolds in which heterotic strings can be compactified. In order to achieve that, we make use of their correspondence to crystallographic space groups, which are already known up to dimension 6, and whose number is fortunately finite. We establish which of those crystallographic groups possess the desired properties to describe the MSSM at low energies, and compute some of the relevant properties that allow for the description of the particle content and their interactions. We also relate our classification to previous, incomplete ones in the literature.

Samenvatting

Part I

Wanneer de elektromagnetische straling van het hemelgewelf wordt waargenomen aan de hand van microgolven, dan is een milde achtergrondstraling zichtbaar die praktisch constant is in alle richtingen (zodra de grootste bijdragen van de voorgrond verwijderd zijn, zoals de straling die uit ons eigen melkwegstelsel komt). Waar komt deze straling vandaan? Waar vindt het zijn oorsprong? Toen wetenschappers de huidige kosmologische data probeerden te beschrijven met algemene relativiteitstheorie bleek in de vroeg-twintigste eeuw dat het universum zich tijdens haar gehele levensduur heeft uitgebreid (en dat nog steeds doet). Net zoals een gas heet wordt wanneer het samengeperst wordt, moet het universum in het verleden ook veel heter zijn geweest. Zo heet, dat op een gegeven moment de elektronen zoveel energie hadden dat zij liever gescheiden waren van de atoomkernen, vrijuit stromend en verstrooiend met fotonen, om een zogenaamd *plasma* te vormen. Toen deze energie door de groei van het universum verdund was geraakt, combineerden de elektronen met de kernen om atomen te vormen en waren de fotonen vrij om te reizen door de ruimte en ons te bereiken. Het zijn deze fotonen die de achtergrondstraling vormen die wij vandaag de dag waar kunnen nemen, datgene dat wij de Kosmische Achtergrondstraling noemen (Cosmic Microwave Background, CMB).

Wanneer men de CMB zorgvuldig waarneemt, is het eerste kenmerk dat zich toont hoe opvallend constant de straling is, bekeken over het gehele hemelgewelf. Dit is zeker niet wat we zouden verwachten. Aan de ene kant, het feit dat twee regio's van het universum praktisch hetzelfde signaal uitstralen is een indicatie dat zij in *evenwicht* zijn – de hete en koude regio's hebben energie met elkaar uitgewisseld totdat zij dezelfde temperatuur hadden bereikt. Aan de andere kant, volgens de snelheid waarmee ons universum uitdijt in ons kosmologische model zouden de regio's die meer dan een paar graden op het hemelgewelf van elkaar verwijderd zijn zo ver uit elkaar staan dat zij nooit tijd hebben gehad om energie uit te wisselen, ook niet aan het begin van het ontstaan van het universum. Dus hoe kunnen zij dan in evenwicht zijn?

Deze tegenspraak was in de jaren 80 opgelost met een cruciale aanpassing van het kosmologische model: we nemen aan dat in de eerste ogenblikken van het

bestaan van het universum, deze een explosief versnellende (bijna exponentiele) expansie heeft doorgemaakt. Een dergelijke expansie zou een klein stukje met een bijna constante temperatuur opblazen tot een regio die groter is dan dat deel van het universum dat wij vandaag de dag kunnen zien. Daarom is het zo dat datgene dat nu in het universum ver van elkaar verwijderd is, zo dichtbij elkaar stond in het verleden dat er bijna geen verschil in temperatuur was tussen deze twee punten. Deze periode van explosieve expansie heet *inflatie*.

Naast het feit dat de CMB het grootste bewijs is voor het bestaan van inflatie, bevat deze ook de meeste informatie over inflatie die we op dit moment hebben. Deze informatie kan gevonden worden in de extreem kleine fluctuaties van de CMB, tien duizend keer kleiner dan de bijna constante temperatuur van de achtergrondstraling zelf. Zulke fluctuaties zijn ontstaan toen de explosieve expansie de kleine, willekeurige kwantumfluctuaties op de kleine schaallengte heeft omgevormd tot dichtheidsverschillen in de materie die verdeeld zijn over grote afstanden in de kosmos. Als de fluctuaties, die we vandaag waarnemen, hun oorsprong vinden in kleine afstanden, dan moeten ze wel aan elkaar gerelateerd of *gecorrleerd* zijn. Het gemiddelde van temperatuurverschillen over de hele hemel, tussen paren van punten die op een bepaalde hoek van elkaar staan aan de hemel, is karakteristiek voor de correlatie tussen deze fluctuaties. Dit gemiddelde als functie van de hoek tussen de punten, heet de *twee-puntsrelatie* of het *vermogenspectrum*. Als de fluctuaties volledig willekeurig en ongecorrleerd waren geweest omdat ze hun oorsprong wijd uiteen vonden, in plaats van op kleine afstanden, dan zou dit gemiddelde op nul uitkomen. In plaats van nul, zijn deze fluctuaties relatief groot, en hun precieze eigenschappen kunnen ons veel vertellen over de quantumoorsprong van de fluctuaties.

Op het moment van schrijven van dit proefschrift, heeft de Planckmissie van de European Space Agency (ESA) zijn eerste gegevens beschikbaar gesteld, en we wachten op de volgende en definitieve vrijgave van alle gegevens. Deze gegevens bevatten een zeer nauwkeurige meting van de twee-puntsrelatie van de fluctuaties in de achtergrondstraling en deze meting is in overeenstemming met de uitkomsten van voorgaande experimenten. Bovendien verwacht men dat de volgende vrijgave van gegevens ook een meting van de drie-puntsrelatie ofwel het *bispectrum* zal bevatten. Het bispectrum is een gemiddelde van de correlaties tussen drie punten op vaste afstanden van elkaar over de hele hemel, in plaats van twee. De drie-puntsrelatie is nog niet eerder met voldoende precisie gemeten en is van cruciaal belang voor het bestuderen van inflatie, omdat inflatie een specifieke voorspelling geeft voor drie-puntsrelatie: als inflatie door het eenvoudigste model beschreven wordt, dan is de drie-puntsrelatie naar verwachting nagenoeg nul. Die houdt in dat de fluctuaties Gaussisch verdeeld zijn. Andere gecompliceerdere modellen van inflatie voorspelen uiteenlopende maar specifieke drie-puntsrelaties. Nu is gezegd het uur U om uitbreidingen van het simpelste raamwerk van inflatie te testen.

In het simpelste model van inflatie wordt de explosieve uitdijning van het heelal veroorzaakt door één enkel type *materie* in het universum: het *inflaton*. Het in-

flaton heeft een negatieve druk. In dit proefschrift werken we onder de aanname dat het inflaton niet alleen was, alhoewel het wel de voornaamste component blijft – er waren meerdere soorten materie aanwezig, die ervoor zorgden dat het inflaton een stijve achtergrond ervoer. Als het inflaton interactie heeft met die stijve achtergrond, dan zullen de twee- en drie-punts correlaties van de fluctuaties van de kosmische achtergrondstraling kleine maar bijzondere eigenschappen hebben. Door naar deze specifieke eigenschappen te zoeken in de gegevens van de achtergrondstraling, kunnen we zien of het inflaton bewoog in zo'n stijve achtergrond die niet triviaal is, en kunnen we zelfs de specifieke vorm van deze achtergrond achterhalen.

Omdat zoals eerder gezegd de drie-punts correlatie nog niet is vrijgegeven door de Planckmissie, op het moment van schrijven van dit proefschrift, hebben we in de gegevens van de Planckmissie gezocht naar karakteristieke eigenschappen in de twee-punts correlatie. Nadat we de beste kandidaten voor de twee-punts correlatie hebben gevonden, hebben we de bijbehorende drie-punts correlatie uitgerekend, die we verwachten te kunnen ontdekken in de nieuwe gegevens van Planck zodra die worden vrijgegeven. Deze test voor onze simpele uitbreiding van het simpelste inflatiemodel, staat ons nog te wachten. Bovendien hebben we ons onderzoek uitgebreid naar structuren op grote schaal, die ook informatie over inflatie bevatten, omdat sterrenstelsels en clusters het eindproduct zijn van de primordiale fluctuaties. De gegevens van de structuur op grote schalen bevestigen de beste kandidaten die we vonden in de achtergrondstraling van Planck.

Part II

Met de ontdekking van het Higgs deeltje in de ATLAS en CMS experimenten van de Large Hadron Collider (LHC) zijn alle belangrijke voorspellingen van het standaardmodel van de deeltjesfysica uitgekomen, en kan het dus als *compleet* worden beschouwd. Er zijn echter een aantal experimentele en theoretische redenen om te proberen het uit te breiden.

Aan de experimentele kant is er al één fenomeen waargenomen dat niet verklaard kan worden met het standaardmodel: *neutrinooscillaties*, dat wil zeggen hoe neutrino's, die voorkomen in drie soorten of generaties, spontaan van de ene generatie in de andere veranderen. Dit is overduidelijk waargenomen, zowel in de stroom van neutrino's die van de zon komen, als in degenen die in deeltjesversnellers gegenereerd worden. Dit gedrag is alleen mogelijk voor deeltjes die massa hebben, terwijl neutrino's volgens het standaardmodel per definitie massaloos zijn. Iedere verklaring voor de massa van neutrino's impliceert dus fysica buiten het standaardmodel.

Donkere materie wordt ook niet verklaard door het standaardmodel. De aanwezigheid van donkere materie is noodzakelijk om de kosmologische en galactische dynamica die we in het heelal waarnemen te verklaren (hetzelfde geldt voor donkere energie, wat hier niet besproken wordt). Desondanks is donkere materie nog nooit direct waargenomen in deeltjesversnellers of sterrenkundige ex-

perimenten. Er is daarom weinig bekend over de *aard van donkere materie* en hoe het in een uitbreiding van het standaardmodel past.

Aan de theoretische kant bestaan verschillende argumenten. Om te beginnen is de massa van het Higgs deeltje, hoewel niet voorspeld door het standaardmodel, verrassend laag. Deeltjes worden zwaarder door de wisselwerking met de deeltjes waar ze aan gekoppeld zijn. Aangezien het Higgs-veld gekoppeld is aan alle fermionen, was de verwachting dat al deze bijdragen tot een veel hogere massa geleid zouden hebben. De verrassend lage massa suggereert het bestaan van een symmetrie die dit tegengaat. Eén mogelijkheid is de introductie van tegenhangers van de deeltjes in het standaardmodel met andere spin maar ongeveer gelijke massa. Het verschil in spin zou automatisch de bijdrage aan de massa van het Higgs deeltje te niet doen. En omdat de massa van de nieuwe deeltjes vrijwel gelijk zou zijn aan de bekende deeltjes, zouden ze mogelijk al binnen een paar jaar waargenomen kunnen worden met de LHC. We noemen deze symmetrie *Super-Symmetrie* (SUSY) en korten het af als MSSM, de *minimaal mogelijke SUSY-uitbreiding van het standaardmodel*.

SUSY heeft een bijkomend gevolg: het hint op de vereniging van alle fundamentele krachten die werken op subatomaire schaal, d.w.z. de *sterke* en *zwakke* kernkracht en de electromagnetische kracht. Dit speculatief fenomeen noemt men de *Grand Unification* en elke theorie die dit in detail beschrijft wordt een *Grand Unification Theory* (GUT) genoemd. GUT's zouden verklaren waarom de *hyperlading*, een van de kwantumgetallen van de deeltjes in het standaard model, in feite gekwantiseerd is. SUSY, gecombineerd met GUT, zou ons ook voorzien van verscheidene kandidaatdeeltjes voor de donkere materie die we (indirect) waarnemen in het universum.

Het MSSM bezit alle bovengenoemde, wenselijke eigenschappen maar tegen de prijs van de introductie van vele nieuwe vrije parameters in het model. Dit maakt het minder voorspelbaar, hetgeen nooit gewenst is voor een fysisch model. Bovendien behandelt het niet de kwantum-aard van de resterende fundamentele interactie: zwaartekracht. Zulke zaken kunnen worden behandeld onder aanname dat het MSSM ingebed is in snaartheorie. De snaartheorie verstrekt ons een goed gedefinieerde beschrijving van kwantumgravitatie. Wanneer de geometrie en enkele eigenschappen van de theorie gekozen zijn kan de gehele fenomenologie op iedere energy schaal, inclusief dat wat we tegenwoordig waarnemen, berekend worden.

Dit is in het bijzonder het geval in de context van dit proefschrift, Heterotische snaren gecompactificeerd in symmetrische toroidale orbifolds; *compactificatie* betekent de aanname dat de extra dimensies eindig en zeer klein zijn in vergelijking met de schaal van standaardmodelnatuurkunde. In deze theorie hoeft men slechts de geometrie van 6 extra dimensies te specificeren, samen met het effect van deze geometrie in de overdragers van de fundamentele interacties (in dat geval, een *rang 16* GUT): is dit gegeven, dan zijn de inhoud en mogelijke interacties van alle fundamentele deeltjes bepaald.

In dit proefschrift voeren wij een classificatie uit van alle mogelijke sym-

metrische toroïdale orbifolds, waarin heterotische snaren kunnen worden gecom-
pactificeerd. Om dit te bereiken maken we gebruik van hun gelijkenis met de
kristallografische ruimtengroepen, welke reeds bekend zijn tot op de zesde dimensie
en wiens aantal gelukkig eindig is. We stellen vast welke van die kristallografische
groepen de gewenste eigenschappen bezit om het MSSM te beschrijven bij lage
energieën en berekenen enkele van de relevante eigenschappen die de beschrijving
van de inhoud en interactie van deeltjes mogelijk maken. Ook relateren wij onze
classificatie aan vorige, incomplete classificaties uit de literatuur.

List of publications

- [1] B. Hu and **J. Torrado**,
Searching for primordial localized features with CMB and LSS spectra,
accepted in Phys. Rev. D,
arXiv:1410.4804 [astro-ph.CO].
- [2] A. Achucarro, V. Atal, B. Hu, P. Ortiz and **J. Torrado**,
*Inflation with moderately sharp features in the speed of sound: Generalized
slow roll and in-in formalism for power spectrum and bispectrum*,
Phys. Rev. D **90** (2014) 023511,
arXiv:1404.7522 [astro-ph.CO].
- [3] A. Achucarro, V. Atal, P. Ortiz and **J. Torrado**,
*Localized correlated features in the CMB power spectrum and primordial bis-
pectrum from a transient reduction in the speed of sound*,
Phys. Rev. D **89** (2014) 103006,
arXiv:1311.2552 [astro-ph.CO].
- [4] M. Fischer, M. Ratz, **J. Torrado** and P.K.S. Vaudrevange,
Classification of symmetric toroidal orbifolds,
JHEP **1301** (2013) p. 084,
arXiv:1209.3906 [hep-th].

Curriculum vitæ

I was born in Badajoz (Spain) in 1984, and raised in the nearby little village of Barcarrota. I attended primary school at Colegio Santiago Apóstol in Barcarrota, and secondary school at Colegio Hernando de Soto in Barcarrota, and Colegio Santo Ángel in Badajoz. I attended high school at Instituto Zurbarán, in Badajoz.

In 2002, I enrolled in Physics at the University of Extremadura in Badajoz. During my undergraduate studies I was awarded a SICUE/Séneca grant, which allowed me to move to Salamanca to finish my studies with a major in Fundamental Physics. During my stay in Salamanca, I was awarded three short research fellowships: at the Institute for Mathematics and Fundamental Physics of the CSIC in Madrid, at the Physics Department of the University of Salamanca, and at the Institute for Astrophysics of the Canary Islands in Tenerife. It was during those fellowships that I decided to pursue an academic research career.

After being awarded a Ph.D. fellowship at the Graduate School “Particle Physics at the Energy Frontier of New Phenomena”, I started my Ph.D. studies in 2010 at the Physics Department of the Technical University of Munich, under the supervision of prof. dr. Michael Ratz, on *Model building in Heterotic Orbifolds*. Later, I moved to the Institute Lorentz of the University of Leiden, under the supervision of prof. dr. Ana Achúcarro, where I continued and concluded my Ph.D. studies on *Searches for turns in the inflaton potential in cosmological data*. During my Ph.D. studies I performed teaching assistance in Particle Physics during several terms, visited various research institutions and attended many conferences on Theoretical Physics and Cosmology.

In 2014, I moved to the Institute for Astronomy of the University of Edinburgh as a postdoctoral researcher in the group of prof. dr. Andrew Liddle.

Acknowledgements

“ [On his way to school, Felipe reads the inscription of a statue:]
‘Tireless fighter of illustrious ideas...’ [and moans:]
‘Anybody can do that. The real feat is to be tired and keep fighting’.”
— Joaquín Salvador Lavado (Quino)

First and foremost, I must express my gratitude towards my supervisor prof. dr. Ana Achúcarro, first for her taking me back in the Ph.D. track, and later for a more than excellent supervision. Her trust and encouragement when I needed them most made this thesis possible. On top of that, she gave me the priceless opportunity to visit some of the best conferences and scientific institutions, and meet some of the best cosmologists in the world.

Thanks in second place to my collaborators during my Ph.D.: Ana Achúcarro, Vicente Atal, Maximilian Fischer, Bin Hu, Pablo Ortiz, Michael Ratz and Patrick Vaudrevange. It has been a great pleasure to learn and do research with you all. You have made me put the best of me in every paper.

Thanks as well to all the colleagues with whom I have discussed through these years and from whom I have learned so much: Benjamin Audren, Alexei Boyarski, Martin Bucher, James Ferguson, Juan García Bellido, Jinn-Ouk Gong, Rolf Kappl, Sebastian Konopka, Julien Lesgourges, Andrew Liddle, Daan Meerburg, Gonzalo Palma, Enrico Pajer, Subodh Patil, Dorothea Samtleben, Bartjan van Tent, Wessel Valkenburg and Licia Verde. All of you definitely contributed to shape my ideas as a scientist.

I am indebted to prof. dr. Otmar Biebel, Head of the Graduiertenkolleg for Particle Physics at the Energy Frontier of New Phenomena in Munich, and prof. dr. Eric Eliel, Scientific Director of the Leiden Institute of Physics, for providing me with the means to carry out the research presented here, and for their personal trust in complicated circumstances. I also thank prof. dr. Michael Ratz for the opportunity to start my Ph.D. studies at the Technical University of Munich. I am indebted also to Fernando Atrio Barandela, Ricardo Génova Santos, Juan Antonio Navarro González, Rafael Rebolo López and José Alberto Rubiño Martín, for supporting me in my search for a Ph.D. position. In addition, I owe to José Alberto and Ricardo my gratitude for a wonderful first contact with scientific research.

My deep gratitude goes also to the administrative staff both at the TU Munich, especially to Mrs. Karin Ramm, and the University of Leiden, especially to Mrs. Fran Ouwerkerk-Persaud and Mrs. Marianne Gouw-van Dun; it has been a sincere pleasure to share my workplace with such great professionals. Special thanks are due to dr. Stefan Recksiegel at the TU Munich for outstanding and unrivalled IT support. I thank also the staff at the research institutions that I have visited during my studies, as well as the organisers of the many conferences and schools that I have attended.

Special thanks also to Mark Bogers, Jelte de Jong, Thanja Lamberts and Wessel Valkenburg for the translation of my summary to the language of Lorentz, Spinoza and Vermeer.

On a more personal level, my deep gratitude to my friends in Munich from the T30e group (especially, Maxi, Christian and Sebastian) and the T30d group (especially Camilo, Cristoforo, Ana, Anna, Miguel and Alejandro), and to my good friends Juan and Esther, Javi, Gabor and Maria, who cheered me up when I needed it most; in Leiden, to my friends at the Lorentz Institute (especially Pablo, Vicente, Bin, Wessel and Mark), and at the Sterrewacht (especially Irene, Matteo, Nicola, Mattia, Marco, Thanja, Silvia and Alessandra), and to my dear friends Andrea and Ludo. Also, thanks to my colleagues and friends from Physics in Badajoz and Salamanca (especially Guadalupe, Jónatan, Víctor, Nube and Rodrigo), and to my very closest friends in Barcarrota and Badajoz, who know they are practically my family.

To conclude, thanks to my parents for teaching me what are the really important things in life, for always keeping me convinced that I could achieve anything I wanted to achieve, and for supporting me in the process in every way imaginable. My gratitude also goes to my *adoptive* family, Derlinda, Augusto and Ulises, for their love, encouragement and hospitality.

And finally thanks to the biggest and best force in my life, Berenice. Thanks for staying by my side in the best and worst of times; thanks for making me a better person, little by little, during these years; thanks for believing in me, regardless of the circumstances, and thanks for your encouragement to keep fighting and take charge of my career and my life. To you, more than anyone else, belongs a huge part of this and all my future achievements. Thank you.